

PL-TR-95-2058

## **RADIATION BELT ANALYSIS AND MODELING**

J. N. Bass  
U. DasGupta  
C. A. Hein  
J. M. Griffin  
D. S. Reynolds

Radex, Inc.  
Three Preston Court  
Bedford, MA 01730

April 22, 1995

Final Report  
April 1990 - May 1995

19960325 063

Approved for public release; distribution unlimited



**PHILLIPS LABORATORY**  
**Directorate of Geophysics**  
**AIR FORCE MATERIEL COMMAND**  
**HANSCOM AIR FORCE BASE, MA 01731-3010**

"This technical report has been reviewed and is approved for publication"



EDWARD C. ROBINSON  
Contract Manager  
Data Analysis Division



ROBERT E. MCINERNEY, Director  
Data Analysis Division

This report has been reviewed by the ESD Public Affairs Office (PA) and is releasable to the National Technical Information Service (NTIS).

Qualified requestors may obtain additional copies from the Defense Technical Information Center. All others should apply to the National Technical Information Service.

If your address has changed, or if you wish to be removed from the mailing list, or if the addressee is no longer employed by your organization, please notify PL/IM, 29 Randolph Road, Hanscom AFB, MA 01731-3010. This will assist us in maintaining a current mailing list.

Do not return copies of this report unless contractual obligations or notices on a specific document requires that it be returned.

REPORT DOCUMENTATION PAGE			Form Approved OMB No. 0704-0188	
<small>Public reporting burden for this collection of information is estimated to average 1 hour per response, including the time for reviewing instructions, searching existing data sources, gathering and maintaining the data needed, and completing and reviewing the collection of information. Send comments regarding this burden estimate or any other aspect of this collection of information, including suggestions for reducing this burden, to Washington Headquarters Services, Directorate for Information Operations and Reports, 1215 Jefferson Davis Highway, Suite 1204, Arlington, VA 22202-4302, and to the Office of Management and Budget, Paperwork Reduction Project (0704-0188), Washington, DC 20503.</small>				
1. AGENCY USE ONLY (Leave blank)		2. REPORT DATE 22 April 1995		3. REPORT TYPE AND DATES COVERED Final Report (April 1990 - May 1995)
4. TITLE AND SUBTITLE  Radiation Belt Analysis and Modeling			5. FUNDING NUMBERS  PE 62101F PR 7601 TA 22 WU RA  Contract F19628-90-C-0090	
6. AUTHOR(S)  J. N. Bass                      C. A. Hein                      D. S. Reynolds U. DasGupta                      J. M. Griffin				
7. PERFORMING ORGANIZATION NAME(S) AND ADDRESS(ES)  RADEX, Inc. Three Preston Court Bedford, MA 01730			8. PERFORMING ORGANIZATION REPORT NUMBER  RXR-95051	
9. SPONSORING / MONITORING AGENCY NAME(S) AND ADDRESS(ES)  Phillips Laboratory 29 Randolph Road Hanscom AFB, MA 01731-3010  Contract Manager: Edward C. Robinson/GPD			10. SPONSORING / MONITORING AGENCY REPORT NUMBER  PL-TR-95-2058	
11. SUPPLEMENTARY NOTES				
12a. DISTRIBUTION / AVAILABILITY STATEMENT  Approved for Public Release Distribution Unlimited			12b. DISTRIBUTION CODE	
13. ABSTRACT (Maximum 200 words)  <p>Efforts have been conducted in modeling of radiation belts, and cosmic radiation, principally in connection with the CRRES mission. Statistical studies of solar particle events have been conducted in a search for predictors of the occurrence of geomagnetic storms. Certain spectral and temporal properties of protons and electrons were found to correlate with the occurrence of storms. Comparative studies of solar proton fluxes observed at locations inside (using CRRES and GOES-7) and outside (using INP-8) the inner magnetosphere were performed in an attempt to measure penetration of solar protons to various L-shells as functions of time during a proton event and the subsequent magnetic storm. The failure to observe large increases in proton fluxes at the sudden commencement of the great magnetic storm of March, 1991, indicates a magnetospheric process was involved. An attempt was made to model the acceleration of radiation belt protons by magnetospheric compression during this event. The access of Helium into the inner magnetosphere was studied during this event. Modeling of instrument contamination and dosage were performed to enhance interpretation of measurements by the Proton Telescope and the Space Radiation Dosimeter. Support software packages developed include a science summary data base, a data processing system for the microelectronics package, and software to analyze measurements by the Low Energy Plasma Analyzer to produce a three dimensional plasma distribution function.</p>				
14. SUBJECT TERMS  Radiation belt, Space radiation dosimeter, Proton telescope, Contamination codes, Solar protons, CRRES, Magnetosphere, Low energy plasma analyzer, Geomagnetic storms			15. NUMBER OF PAGES 158	
			16. PRICE CODE	
17. SECURITY CLASSIFICATION OF REPORT  Unclassified	18. SECURITY CLASSIFICATION OF THIS PAGE  Unclassified	19. SECURITY CLASSIFICATION OF ABSTRACT  Unclassified	20. LIMITATION OF ABSTRACT  Unlimited	

## TABLE OF CONTENTS

<u>Section</u>	<u>Page</u>
<b>1. CORRELATION OF SOLAR PARTICLE EVENTS WITH GEOMAGNETIC STORMS</b>	1
1.1 INSTRUMENT DESCRIPTION AND DATA REDUCTION	1
1.1.1 DMSP/F7 SSJ*	1
1.1.2 IMP-8 CPME	3
1.2 RESULTS FROM IMP-8 CPME	5
1.3 RESULTS FROM DMSP/F7 SSJ*	5
1.4 EVENTS 6 & 7: FEBRUARY 6 AND FEBRUARY 14, 1986	8
1.4.1 Latitudinal Dependence of Particle Fluxes	8
1.4.2 Comparisons of Flare Related Quantities	11
1.4.2.1 Event 1: February 16th, 1984	13
1.4.2.2 Event 2: March 12th, 1984	16
1.4.2.3 Event 3: April 26th, 1984	16
1.5 DISCUSSION AND CONCLUSIONS	16
 <b>2. PROGRAM SSDBGEN - SCIENCE SUMMARY DATA BASE GENERATION</b>	 19
2.1 OVERVIEW	19
2.2 DETAILED SPECIFICATIONS OF SCIENCE SUMMARY DATA BASES	19
2.3 PROGRAM OPERATION	22
2.3.1 Time History Data Bases	22
2.3.2 Calibration Files	22
2.3.3 Ephemeris File	23
2.3.4 User Inputs	23
2.3.5 Orbit Number	23
2.3.6 Number of L segments	23
2.3.7 SSDB Output File Formats	24
2.4 PROGRAM STRUCTURE AND LOGIC	25
2.5 AUXILIARY PROGRAMS	28
2.5.1 Conversion to ASCII - Program SSDBASCII	29
2.5.2 Instrument-Specific Programs	29
 <b>3. THE CRRES MICROELECTRONICS PACKAGE DATA PROCESSING SYSTEM</b>	 30
3.1 MEP SERIAL TELEMETRY	30



## TABLE OF CONTENTS (Cont'd)

<u>Section</u>	<u>Page</u>
3.2 MEP DATA PROCESSING SYSTEM .....	31
3.2.1 MEP Serial Data Processing and Archiving .....	31
3.2.2 Data Retrieval and Presentation .....	36
3.2.3 Software Architecture and Development .....	44
3.3 MEP DATABASE .....	45
3.3.1 File Storage .....	45
3.3.2 Permanent Database File Formats .....	46
3.3.3 Permanent Database Packet Formats .....	48
3.3.4 SEU Chip History File Format .....	50
3.3.5 JPL File Formats .....	50
3.3.6 4007 Inverter File Format .....	50
<b>4. MARCH 1991 MAGNETIC STORM MODELING .....</b>	<b>53</b>
4.1 INTRODUCTION .....	53
4.2 METHODOLOGY .....	54
4.2.1 Relativistic Equations of Motion .....	55
4.2.2 Relativistic Guiding Center Equations of Motion .....	56
4.2.3 Magnetic Field Models: .....	59
4.2.4 Applications .....	64
4.2.4.1 Adiabatic Invariants .....	64
4.2.4.2 Application .....	66
4.3 TRAJECTORY COMPUTATION SUMMARY .....	68
4.3.1 Description of Trajectories .....	68
4.3.2 Dependence of Initial Conditions .....	68
4.3.3 Results .....	68
<b>5. ONR-604 PROCESSING FOR HEAVY ION COMPOSITION AND SPECTRA .....</b>	<b>74</b>
5.1 INTRODUCTION--GOALS .....	74
5.2 DESCRIPTION OF INSTRUMENT .....	74
5.3 EVENTS AND RATE TIMINGS .....	81
5.4 EXTRACTION OF PURE PROTON AND HELIUM COUNT RATES ..	82
5.5 MARCH, 1991, STORM .....	85
<b>6. PROTON EVENT OBSERVATIONS .....</b>	<b>94</b>

## TABLE OF CONTENTS (Cont'd)

<u>Section</u>	<u>Page</u>
<b>7. CRRES INSTRUMENT MODELING: PROTEL</b> .....	101
7.1 PROTEL CONTAMINATION CODE .....	101
7.1.1 Description of the PROTEL Contamination Code .....	103
7.1.2 Results .....	104
7.2 EFFECT OF APERTURE AND ROTATION ON OBSERVATIONS OF PROTON PITCH ANGLE DISTRIBUTIONS .....	112
7.2.1 Introduction .....	112
7.2.2 Methodology .....	113
7.2.3 Results .....	116
<b>8. CRRES INSTRUMENT MODELING: CRRES DOSIMETER</b> .....	120
<b>9. LOW ENERGY PLASMA MOMENTS FROM CRRES LEPA DATA</b> .....	124
9.1 BACKGROUND INFORMATION ON LEPA .....	124
9.2 PROCESSING OF LEPA DATAFILES .....	126
9.3 THE BASICS OF THE LEPA FILE PROCESSING .....	127
9.3.1 Theoretical Motivations .....	127
9.3.2 Basic Steps of the Software Processing .....	130
9.3.2.1 Magnetometer Database Processing .....	132
9.3.2.2 Binning of Differential Directional Flux .....	134
9.4 INTRODUCTION TO LEPAFLUX .....	135
9.4.1 Overall General Descriptions for Input .....	135
9.4.1.1 Input Files .....	136
9.4.2 Overall General Descriptions for Output .....	136
9.4.2.1 Structure and Format of the Primary Output Data File .	136
9.5 PROCESSING OF THE MAGNETOMETER DATABASE .....	137
9.5.1 Output File from PCCALMAG .....	137
9.6 INTRODUCTION TO GET3DBIN .....	138
9.6.1 Overall General Descriptions for Input .....	138
9.6.1.1 Namelist File Descriptions .....	138
9.6.1.2 Input Files .....	139
9.6.2 Overall General Descriptions for Output .....	139
9.6.2.1 Output Datafiles .....	141
<b>REFERENCES</b> .....	142

## LIST OF FIGURES

<u>Figure</u>	<u>Page</u>
1. Schematic of one of the four sensors of the DMSP/F7 space Radiation Dosimeter . . .	2
2. Construction of the IMP-8 Charged Particle Measurement Experiment . . . . .	4
3a. Proton and electron count rates in DMSP/F7 SSJ* instrument during solar particle events . . . . .	7
3b. Dst indices over the time period of February 6th and 14th, 1986 . . . . .	7
4a. Latitudinal variation of proton fluxes during a particle event between February 6-9 and a quiet time February 10-13 . . . . .	9
4b. Particle event between February 14-17 compared to the same quiet period . . . . .	9
5a. Latitudinal variation of electron fluxes during a particle event between February 6-9 and a quiet time February 10-13 . . . . .	10
5b. Particle event between February 14-17 compared to the same quiet period . . . . .	10
6. Plots of the proton and electron component, solar wind plasma, Kp and Dst indices between February 5th and 18th, 1986. The occurrence of Xray flares and sudden commencements are also indicated . . . . .	12
7. Proton and electron count rates in DMSP/F7 SSJ* instrument during solar particle event of February 16th 1984, and corresponding Dst indices over the time period . . . . .	15
8. Proton and electron count rates in DMSP/F7 SSJ* instrument during solar particle event of March 14th 1984, and corresponding Dst indices over the time period .	17
9. Proton and electron count rates in DMSP/F7 SSJ* instrument during solar particle event of April 24th 1984, and corresponding Dst indices over the time period . .	18
10. Program organization . . . . .	26
11. File production and delivery system . . . . .	35
12. Accumulated dose vs. total dose . . . . .	38
13. Scatter plot of MEP SEU distribution ICU B vs. $B_0$ . . . . .	41
14. SEU distribution, ICU B . . . . .	43
15. Comparison between guiding center trajectory and computed trajectory . . . . .	57
16. Comparison between guiding center trajectory and computed trajectory . . . . .	58
17. Comparison between guiding center trajectory and computed trajectory . . . . .	58
18. The ONR-604 design . . . . .	75
19. A matrix of energy loss in detector K1 vs total energy loss in K2-K8, for individual events, denoted by points. Note the tracks characteristic of individual nuclear species . . . . .	76
20. Count Rates for the priority groups P1, P2, and P3, for orbit 75 . . . . .	80
21. P2 proton mode event matrix for orbit 586 . . . . .	83
22. P1 proton mode event matrix for orbit 586. The polygon shows events that were counted as Hydrogen . . . . .	84

# LIST OF FIGURES (Cont'd)

<u>Figure</u>	<u>Page</u>
23. H and He count rates before and after the Sudden Storm Commencement (SSC) of 24 March, 1991 . . . . .	86
24. Helium count rate as function of L for ascending (left half) and descending (right half) legs of orbits 575-579, with error bars . . . . .	87
25. Same as Figure 24, except for orbits 580-584 . . . . .	88
26. Same as Figure 24, except for orbits 585-590 . . . . .	89
27. Same as Figure 24, except for orbits 591-595 . . . . .	90
28. Same as Figure 24, except for orbits 596-600 . . . . .	91
29. Same as Figure 24, except for orbits 601-605 . . . . .	93
30. Comparison of 4.6-15 MeV proton mean differential fluxes measured by PROTEL and IMP-8 during March 24-25, 1991 . . . . .	97
31. Same as Figure 30, except at the energy range 48-96 MeV . . . . .	98
32. Ratios of PROTEL-measured mean differential fluxes at L=4 in various energy ranges to those measured by GOES-7 in same energy ranges during March 24-25, 1991 . . . . .	99
33. Same as Figure 32, except for L=5 . . . . .	100
34. Protel HEH Cross Section (Not to Scale). (1) baffle, which defines the nominal entry cone. (2) electron magnetic deflection housing. (3) detector housing. (4) shielding for the detector array . . . . .	102
35. Response function for PROTEL HEH Channel 11 for isotropic distribution. The actual non-contamination channel response is the "spike" at the extreme left of the graph . . . . .	108
36. Response function for PROTEL HEH Channel 12 for isotropic distribution. The actual non-contamination channel response is the "spike" at the extreme left of the graph . . . . .	109
37. Response functions for PROTEL HEH Channel 11 for mirror plane distribution for two orientations of the mirror plane with respect to the deflection magnet 0° (solid line) and 90° (dashed line). The actual non-contamination channel responses are the "spikes" at the extreme left of the graph . . . . .	110
38. Response functions for PROTEL HEH Channel 12 for mirror plane distribution for two orientations of the mirror plane with respect to the deflection magnet 0° (solid line) and 90° (dashed line). The actual non-contamination channel responses are the "spikes" at the extreme left of the graph . . . . .	111
39. Computed equatorial flux at $\alpha = 90^\circ$ (incorporating the effects of the PROTEL HEH aperture and rotation), as a function of L for modified $\sin^N \alpha$ distributions for N = 4, 5, 6 and 8. Note that $\alpha_c$ ranges from 47.5° on the left to 0.25° on the right. For the original distributions, A(E,L) was taken to be 1 . . . . .	116

## LIST OF FIGURES (Cont'd)

<u>Figure</u>	<u>Page</u>
40. The computed distributions (incorporating the effects of aperture and rotation) have been fitted to a single modified $\sin^N \alpha$ distribution. $A(E,L)$ from the single fits is plotted vs $L$ for $N = 4, 5, 6$ , and $8$ . . . . .	117
41. Ratio of equatorial omnidirectional flux (from fits of the computed pitch angle distribution to a single modified $\sin^N \alpha$ distribution) to that of the original modified $\sin^N \alpha$ distribution is plotted as a function of $L$ for $N = 4, 5, 6$ , and $8$ . . . . .	118
42. Ratio of equatorial omnidirectional flux (from fits of the computed pitch angle distribution to the sum of 2 modified $\sin^N \alpha$ distributions) to that of the original modified $\sin^N \alpha$ distribution is plotted as a function of $L$ for original $N=4, 5, 6$ , and $8$ . . . . .	118
43. Sample comparison ( $N=4, \alpha_c=47.5, L=1.25$ ) of the computed pitch angle distribution with the original modified $\sin^N \alpha$ pitch angle distribution . . . . .	119
44. Path length distribution computed using the Monte Carlo method for CRRES dosimeter detector 1 . . . . .	123
45. Processing of LEPA data by steps . . . . .	131

## LIST OF TABLES

<u>Table</u>	<u>Page</u>
1. DMSP/F7 SSJ* Instrument Specification . . . . .	2
2. Solar Proton Events from IMP-8 CPME . . . . .	6
3. Comparison of Solar Particle Events of February 6th and 14th, 1986 . . . . .	14
4. Science Summary Data Base Instruments and Channels . . . . .	20
5. Accumulation Intervals . . . . .	21
6. Time History Data Base Instrument Designators . . . . .	22
7. Instrument-Specific Subroutines . . . . .	25
8. Functional Descriptions . . . . .	27
9. GL 701-1A Data File Format . . . . .	30
10. Sample of READMEP Output, Orbit 703 . . . . .	33
11. Sample of Update to the "Audit" File . . . . .	34
12. Sample DUT Power Table, Orbit 700 . . . . .	37
13. Portion of an Abbreviated Command History . . . . .	39
14. Sample Output from SEUEPH . . . . .	40
15. Table of Upsets . . . . .	42
16. Archived Data Packets . . . . .	47
17. JPL Timing File Format . . . . .	51
18. JPL Transistor File Format . . . . .	51
19. 4007 Inverter File Format . . . . .	52
20. Proton Trajectories for Compression of Standoff Distance from 10 to 5 $R_E$ in 30 Seconds . . . . .	69
21. Proton Trajectories for Compression of Standoff Distance from 10 to 5 $R_E$ in 60 Seconds . . . . .	70
22. Comparison of Adiabatic Calculations with Guiding Center Trajectory Calculations of Energy Gain and Radius at CRRES Location for Karl Pfizter Dynamical Field Model . . . . .	71
23. Proton Trajectory Data - Relativistic Equations of Motion . . . . .	72
24. Proton Trajectory Data - Guiding Center Equations of Motion . . . . .	73
25. ONR-604 Pulse Height Analysis Gate Control and Priority Logic, and Ground Command . . . . .	78
26. ONR-604 Detector Thresholds (MeV) . . . . .	79
27. PROTEL and IMP-8 (CPME) Channels . . . . .	95
28. PROTEL and GOES-7 Channels . . . . .	95
29. PROTEL Energy Channels . . . . .	95
30. FRACTION OF PROTEL HEH COUNTS DUE TO CONTAMINATION Isotropic Distribution POWER LAW SPECTRUM $E^{**q}$ . . . . .	106

# LIST OF TABLES (Cont'd)

<u>Table</u>	<u>Page</u>
31. FRACTION OF PROTEL HEH COUNTS DUE TO CONTAMINATION due to protons with $E > 100$ MeV . . . . .	106
32. FRACTION OF PROTEL HEH COUNTS DUE TO CONTAMINATION due to protons with $E > 200$ MeV . . . . .	106
33. FRACTION OF PROTEL HEH COUNTS DUE TO CONTAMINATION MIRROR PLANE LIMIT, Azimuth = 0 degrees . . . . .	107
34. FRACTION OF PROTEL HEH COUNTS DUE TO CONTAMINATION MIRROR PLANE LIMIT, Azimuth = 90 degrees . . . . .	107
35. Physical and Geometric Parameters of the CRRES Detectors . . . . .	120

## ACKNOWLEDGEMENTS

We would like to thank all those who contributed to this work, either directly or indirectly, and to acknowledge those individuals and groups with whom we worked directly.

First and foremost are M. S. Gussenhoven and E. G. Mullen (PL/PHP) who directed and motivated this research. Other PL personnel who contributed include Ed Robinson (PL/GPD, who initiated and coordinated the activities as contract monitor; Kevin Ray, who provided leadership in the MEP data processing; David Hardy, Rick Lambour, and Kevin Kerns (PL/PHP), who gave advice and assistance in using the data from the Low Energy Plasma Analyzer; and Bob Filz of PL/PHP who gave suggestions and assistance on instrument modeling.

Others we wish to thank include Bill McNeil of Radex for help in attitude and magnetometer processing; Karl Pfitzer of McDonnell Douglas Corp. for supplying his magnetic field model for the March, 1991, storm; Tom Armstrong of the University of Kansas for providing IMP-8 data; Moises Munoz, Roger Pyle, and Cliff Lopate (university of Chicago) for advice in using and analyzing data from high energy, heavy nuclei experiment (ONR-604); and Dennis Delorey and Dan Madden of Boston College for assistance in using the data bases they provided.





## 1. CORRELATION OF SOLAR PARTICLE EVENTS WITH GEOMAGNETIC STORMS

There have been many attempts at forecasting the advent of magnetic storms on Earth. This effort is important since these storms carry many hazards - chiefly the disruption of communications and heating of the ionosphere. So far, no unique set of conditions has been discovered that would predict the occurrence of a magnetic storm. It is generally believed that the arrival of a particle shock at the magnetosphere together with a southward turning of the interplanetary magnetic field are necessary conditions for the precipitation of a magnetic storm. But the problem with using the IMF or plasma shock as indications of storm commencement is that one cannot predict the storm until the conditions are right for its onset.

We have attempted a different approach to this problem. We studied solar proton events that were followed by geomagnetic storms and ones that were not followed by any apparent geomagnetic activity in an effort to examine differences in the particle components that might indicate if a magnetic storm would or would not follow. Since a magnetic storm lags its associated particle event by about 2 days, any indicators for the storm that are found in the particle component would lead to an earlier prediction of the storm than is currently possible. In our study of solar particle events, many of which were followed by magnetic activity, we observed dramatic differences between the class of events where the magnetosphere is quiet and those where it is disturbed. These differences in the particle components are noticed even when the magnitude of disturbances is modest - an overall increase of the ring currents translating to a decrease in the Dst indices of 50 nT or so over the prestorm level. We shall present the results of this study later.

### 1.1 INSTRUMENT DESCRIPTION AND DATA REDUCTION

Solar particle data were obtained from two instruments - the Space Radiation Dosimeter (SSJ\*) on board the DMSP/F7 satellite and the Charge Particle Measurement Experiment (CPME) on the IMP-8 satellite.

#### 1.1.1 DMSP/F7 SSJ\*

The DMSP/F7 was a polar orbiting satellite at an altitude of 840 km. It had a 1.7 hr period and a noon-midnight meridian orbit plane. The Space Radiation Dosimeter on board the satellite consisted of four particle detectors placed behind various thicknesses of aluminum shielding, which place the energy threshold of detection of protons at 20, 35, 51 and 75 MeV, and that for electrons at 1, 2.5, 5 and 10 MeV (Figure 1; Table 1). Details of the instrument construction and calibration can be found in *Gussenhoven, et al.* [1986].

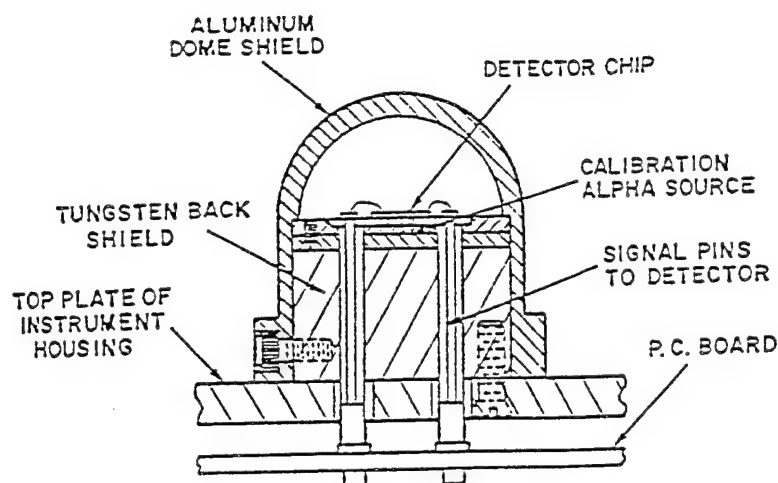


**Figure 1.** Schematic of one of the four sensors of the DMSP/F7 Space Radiation Dosimeter

TABLE 1. DMSP/F7 SSJ* Instrument Specification					
Dome	Aluminum	Range Thresholds		Detector	
	Shield (gm/cm <sup>2</sup> )	Electrons (MeV)	Protons (MeV)	Area (cm <sup>2</sup> )	Thickness (microns)
1	0.55	1.	20	0.051	398
2	1.55	2.5	35	1.000	403
3	3.05	5.	51	1.000	390
4	5.91	10.	75	1.000	384

In each detector of the SSJ\* instrument, particles were separated according to their total energy loss in the detector. The three ranges of energy deposit were the LOLET between 0.05 and 1 MeV, the HILET between 1 and 10 MeV and the VHLET where a total energy deposit of at least 40 MeV was required (75 MeV for detector 3). The flux of particles depositing the required amount of energy in each of the detectors was counted, as well as the cumulative dose resulting from the passage of the particles through the detector. The LOLET channels recorded electrons and high energy protons (energy greater than approximately 120 MeV) while the HILET channels mostly observed protons. The VHLET channels were sensitive only to large

deposits of energy from nuclear "star" events, from the passage of heavy nuclei through the detector, or from protons with a very long path length in the detector.

**Dosimeter Data Specification:** The dosimeter measured HILET, LOLET and VHLET particle count rates in 4 second time bins. Hourly averages of the data were determined after applying two sets of cuts. In order to eliminate the effect of the trapped particle populations, count rates were averaged over latitudes above  $50^\circ$  for protons, while in the case of electrons this was done at latitudes higher than  $70^\circ$ . A further condition was imposed in that each averaging interval contain at least 170, 4 second measurements of the particle fluxes. This ensures a coverage of at least half of a polar cap crossing over an hourly average. This step prevented the latitudinal variation of particle flux levels over the polar cap from obscuring the temporal variations in the particle profiles due to a solar event.

The Dosimeter was operational between December 1983 and February 1988. Solar particle events recorded during that time were isolated for a detailed study.

### 1.1.2 IMP-8 CPME

The Johns Hopkins University/Applied Physics Laboratory's Charged Particle Measurement Experiment (CPME) has been operating on board the IMP-8 satellite since 1973 (Figure 2). Details of the experimental construction and calibration can be found in *Krimigis, et al.* [1973]. The IMP-8 satellite has an almost circular orbit whose distance of closest approach to Earth was 29 Earth radii and as such it spent a large part of its time outside the magnetosphere. The instrument recorded protons in 10 energy channels between 0.3 and 138 MeV, alpha particles in 6 energy channels between 0.64 and 52 MeV/nucleon and 3 channels of electrons spanning the range 0.22 to 2.5 MeV. The data for the CPME experiment were obtained from the NSSDC data bases. They represent omnidirectional hourly averaged integral fluxes of protons above 1, 2, 4, 10, 30 and 60 MeV.

Since the SSJ\* and CPME experiments detect protons inside and outside the magnetosphere respectively, in similar energy ranges, comparisons between solar events seen by both instruments yield information regarding particle entry onto the polar caps from outside the magnetosphere.

The study of the data was divided into two parts. In the first part we studied 11 major solar proton events that were recorded by the proton telescope on board the IMP-8 satellite between December 1983 and February 1988. Of these 11 events, one had a rather soft spectrum which rendered it undetectable above 20 MeV threshold of the DMSP/F7 dosimeter while five of the other events had bad or missing data giving an overall sample of 5 good events in the dosimeter. Both the proton and electron components of these five events were studied in detail in the second part of the data analysis.

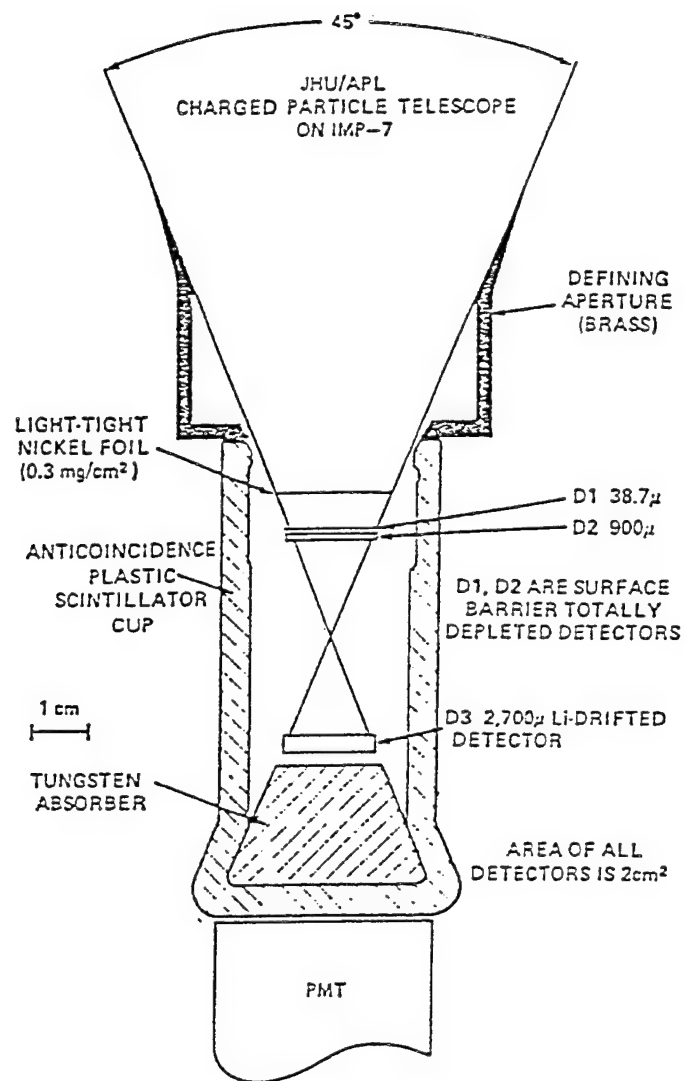


Figure 2. Construction of the IMP-8 Charged Particle Measurement Experiment

## 1.2 RESULTS FROM IMP-8 CPME

A summary of the characteristics of the 11 proton events recorded by the CPME detector was presented in Table 2. The table also includes the geomagnetic activity expressed by the Dst index, during the particle events. The magnetic data were obtained from NSSDC online Interplanetary Medium (OMNI) data bases. The second and third columns of Table 2 list the time of occurrence of the peak in the solar proton event and the flux above 1 MeV at peak, as measured by the IMP-8 proton telescope. The fourth column gives the spectral index at the maximum of the flux. This index is derived by fitting the differential flux to a power law type spectrum of the form  $dN/dE = CE^\gamma$  where  $dN/dE$  is the number of protons per unit energy interval at the energy  $E$ . The values of  $\gamma$  in the last column represent the spectral hardness of the proton event between 1 and 10 MeV.

The last two columns in the table list geomagnetic activity during the events. If evidence of the onset of a magnetic disturbance is found between 1-3 days following the start of a particle event, the minimum recorded Dst over the episode, as well as the time of occurrence of the minimum, are listed in the last two columns of Table 2.

There is one trend that we noticed outright from the data. Proton events that are followed by magnetic storms have a softer spectrum in general than the ones that have no magnetic activity associated with them. The spectral indices for the storm related proton events lie between -1.98 and -4.9, while the rest have a much flatter spectra ranging between -1.1 and -2.2.

## 1.3 RESULTS FROM DMSP/F7 SSJ\*

Five out the eleven proton events detected by the CPME experiment have been recorded by the DMSP dosimeter. We started by analyzing two of the solar events in detail. These occurred on February 6th and February 14th, 1986. The hourly averaged value of the proton count rates above 20 MeV and the electron count rates above 1 MeV measured by the DMSP dosimeter are plotted in Figure 3a. The uniqueness of these two events lies in the fact that while both were fairly large events (peak proton fluxes  $5.4 \times 10^3$  and  $1.4 \times 10^3$  above 1 MeV, respectively) they occurred close to solar minimum. This indicates that although flare occurrences on the sun and the resultant incidence of particle events is less frequent at solar minimum, the magnitude of individual events has little to do with the level of solar activity. Anomalously large solar particle events have been observed at solar minimum, such as one occurring on August 4th, 1972 in the minimum of solar cycle 20 (see for example, *King* [1974]). Another remarkable feature of the February, 1986 events was that although they occurred close together in time, the first event was followed by an extraordinarily large geomagnetic storm for which the Dst index reached a minimum value of -312 nT (Figure 3b), while the second event was not associated with any discernible magnetic activity. Therefore, we tried to investigate any differences in the two particle events which might indicate why the first event was followed by a magnetic storm while the second event was not. The sample of the three remaining particle events was used for

TABLE 2. Solar Proton Events from IMP-8 CPME						
No	Time of start of particle event	Proton Component [CPME/IMP-8]			Magnetic Activity	
		Time of peak Date : Hour	Flux at peak ( $>1$ MeV) $/(\text{cm}^2.\text{sr}.\text{sec})$	Spectral index at peak	Time of minimum Dst Date : Hour	Min. Dst (nT)
1	Feb 16, 84	Feb 16 : 11.5	309.3	-1.08	--	--
2	Mar 12, 84	Mar 14 : 9.5	290.8	-1.93	--	--
3	Apr 25, 84	Apr 26 : 17.5	12320	-1.98	Apr 26 : 3.5	-93
4	Apr 24, 85	Apr 26 : 4.5	6812	-2.62	Apr 28 : 11.5	-99
5	Jul 09, 85	Jul 09 : 7.5	410.3	-2.25	Jul 12 : 19.5	-66
6	Feb 06, 86	Feb 08 : 15.5	5448	-3.19	Feb 09 : 0.5	-312
7	Feb 14, 86	Feb 15 : 3.5	1443	-1.89	--	--
8	Nov 02, 86	Nov 04 : 0.5	8225	-4.91	Nov 04 : 10.5	-109
9	May 29, 87	May 30 : 4.5	28.2	-2.44	May 31 : 22.05	-62
10	Nov 07, 87	Nov 08 : 10.5	1420	-2.17	--	--
11	Dec 29, 87	Dec 29 : 13.5	226.8	-1.48	--	--

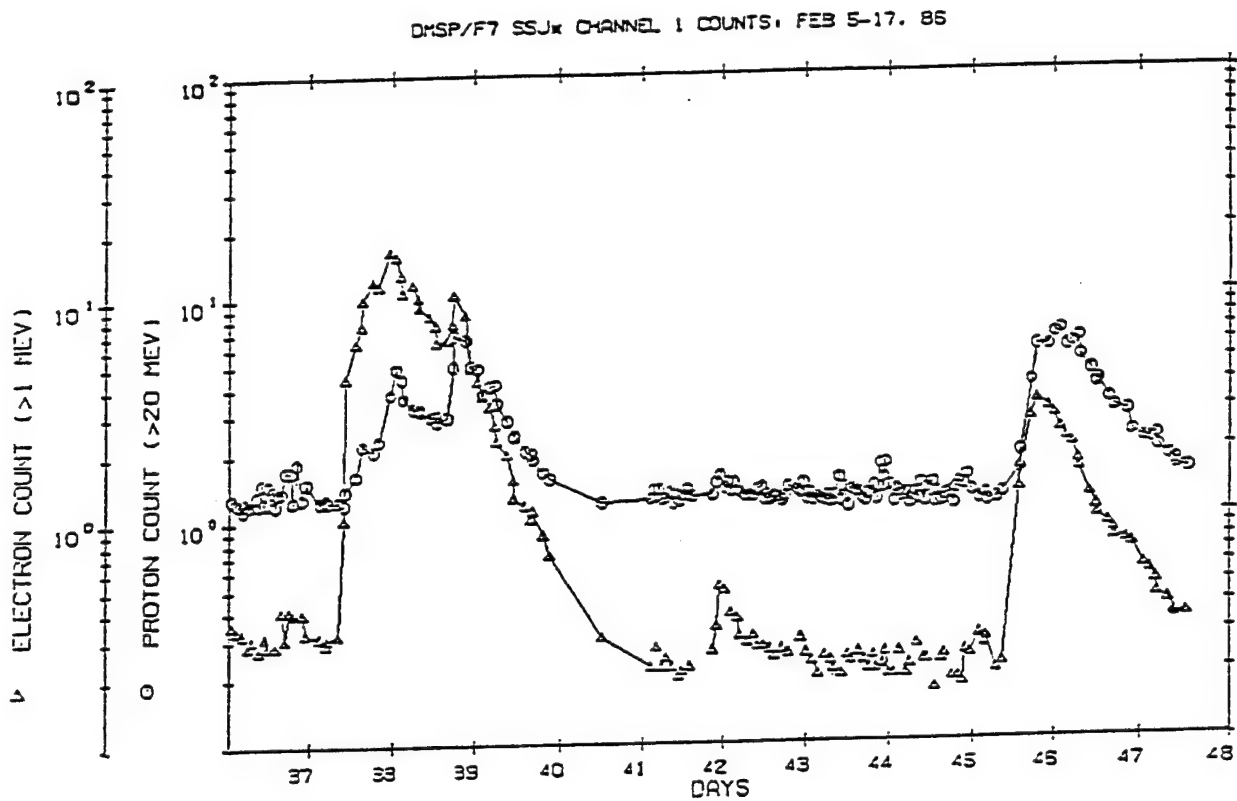


Figure 3a. Proton and electron count rates in DMSP/F7 SSJ\* instrument during solar particle events  
SOLAR GEOPHYSICAL DATA, FEB 05-17, 86

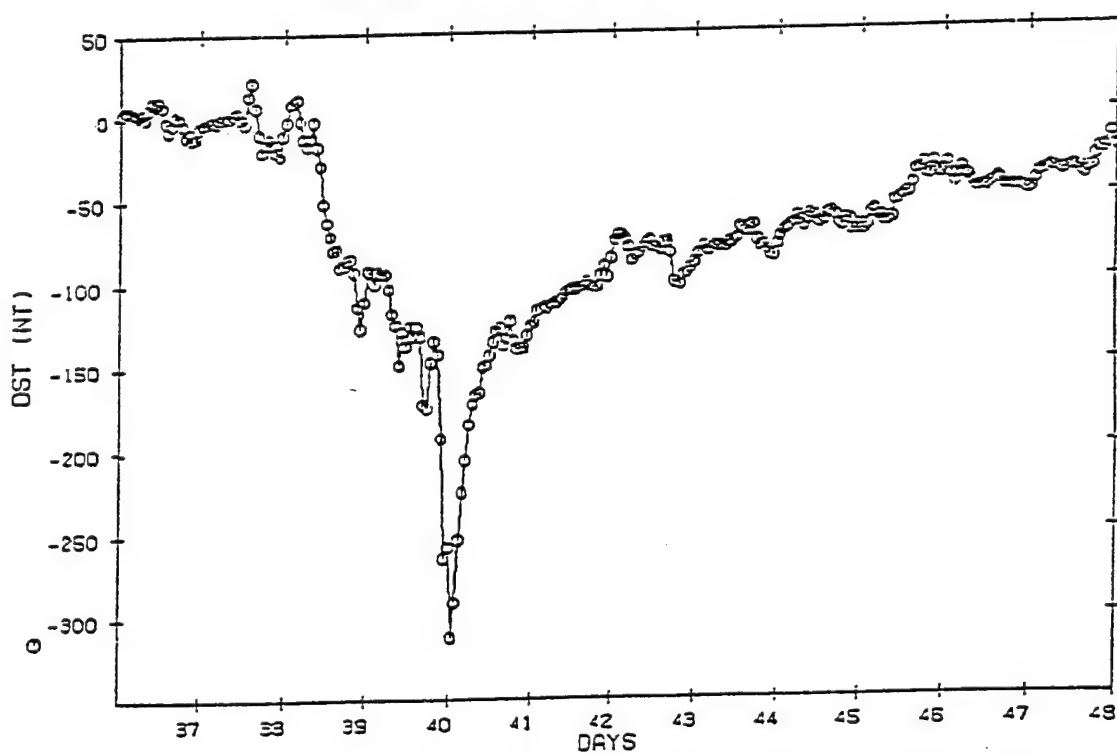


Figure 3b. Dst indices over the time period of February 6th and 14th, 1986.



a verification of the storm predictors found from the comparison of the two February 1986 solar particle events.

#### 1.4 EVENTS 6 & 7: FEBRUARY 6 AND FEBRUARY 14, 1986

We began a detailed comparison of the February 6th and February 14th events by looking first at the latitudinal variations of the particle components during both events. This was followed by a comparison of the DMSP/F7 particle flux measurements made over the polar caps with the interplanetary values obtained from the IMP-8 instruments. Finally, different aspects of the flares that led up to and occurred during the two particle events were compared, as well as the geomagnetic activity occurring during the two events.

##### 1.4.1 Latitudinal Dependence of Particle Fluxes

Being in a  $99^\circ$  inclination orbit, the DMSP/F7 spent a fair fraction of its time over the Earth's polar caps. At these higher latitudes, particles from external sources can gain direct entry into the Earth's magnetosphere. Figure 4a gives the proton count rate above 20 MeV averaged over  $5^\circ$  bins in the latitude over the time of the first solar event between February 6th and 9th (circles) and the quiet time in between the two particle events, i.e. February 10th - 14th (triangles). Over the first time period, both the particle components and the accompanying magnetic storm had reached their peak values.

We noticed that in quiet times, the particle flux profiles are fairly flat over both polar caps. During the solar event, protons start to gain access at around  $50^\circ$  north and south latitudes. There is a peak in the proton fluxes at  $65^\circ$  followed by a flattening off of the flux. In Figure 4b, the quiet time profile is compared to that over the second proton event between February 14th and 17th. We noticed that the variation of the proton flux with latitude is the same as for the previous case, except, possibly, for a sharper fall off in the flux over the north pole.

Next we compared the flux profile of high energy electrons over the DMSP orbit for the first event (5a) and the second event (5b), in both cases using the quiet period in between the two events as the common baseline. In Figure 5a, we noticed that the electron count rate is fairly unperturbed over the inner belts, but that the outer belts, extending between a latitude of  $40^\circ$  and  $70^\circ$ , are perturbed by electron entry during the solar event. Both the equatorial and polar boundaries of the outer electron belt were at higher latitudes. In both hemispheres, the polar edges of the belt shift by about  $2^\circ$ - $3^\circ$  degrees while the equatorial edge sees a more dramatic shift of  $7^\circ$  in the northern hemisphere and  $10^\circ$  in the southern hemisphere. The profile over the polar caps is flat in both cases. Figure 5b represents the flux profiles during the second particle event. Here, we noticed the same poleward shift in the outer zone electrons, though the migration in this case is modest for both edges of the belt in both hemispheres, about  $1^\circ$ - $4^\circ$ .

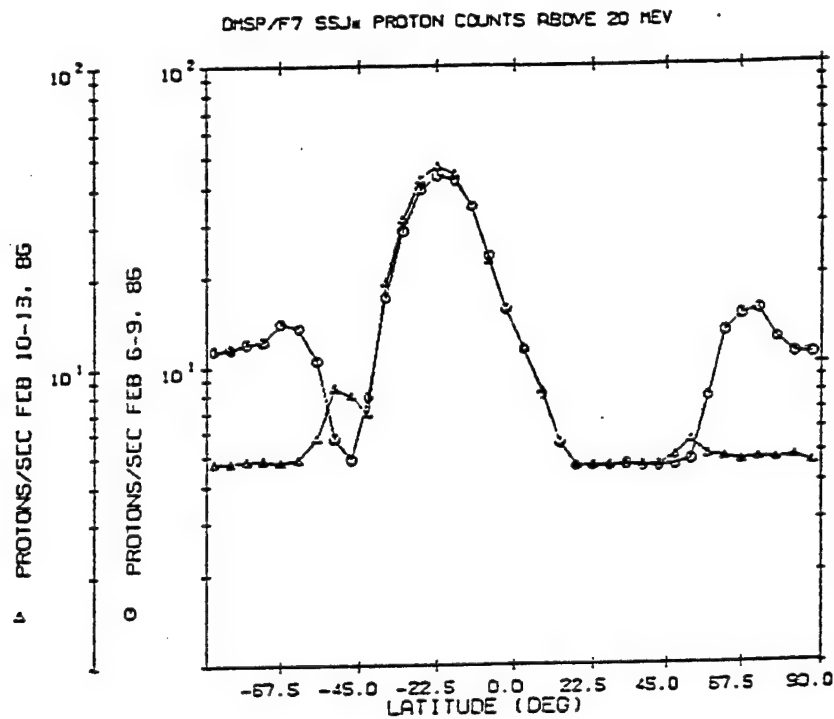


Figure 4a. Latitudinal variation of proton fluxes during a particle event between February 6-9 and a quiet time February 10-13.

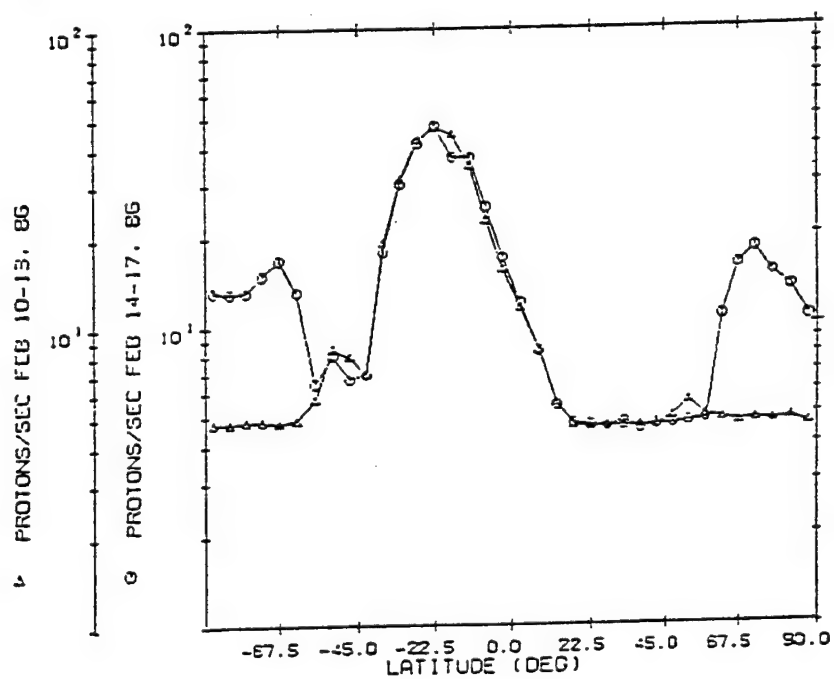


Figure 4b. Particle event between February 14-17 compared to the same quiet period.

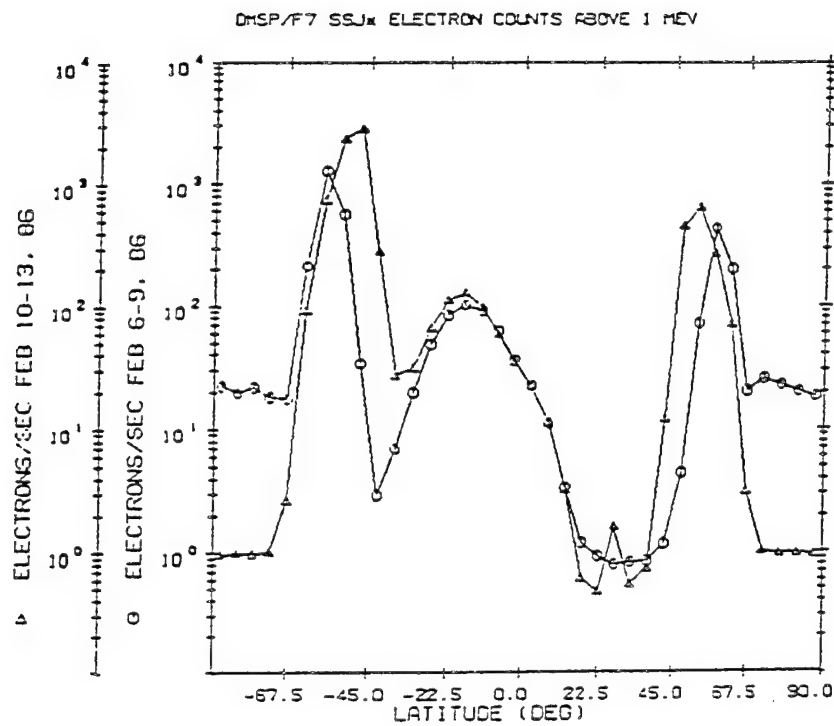


Figure 5a. Latitudinal variation of electron fluxes during a particle event between February 6-9 and a quiet time February 10-13.

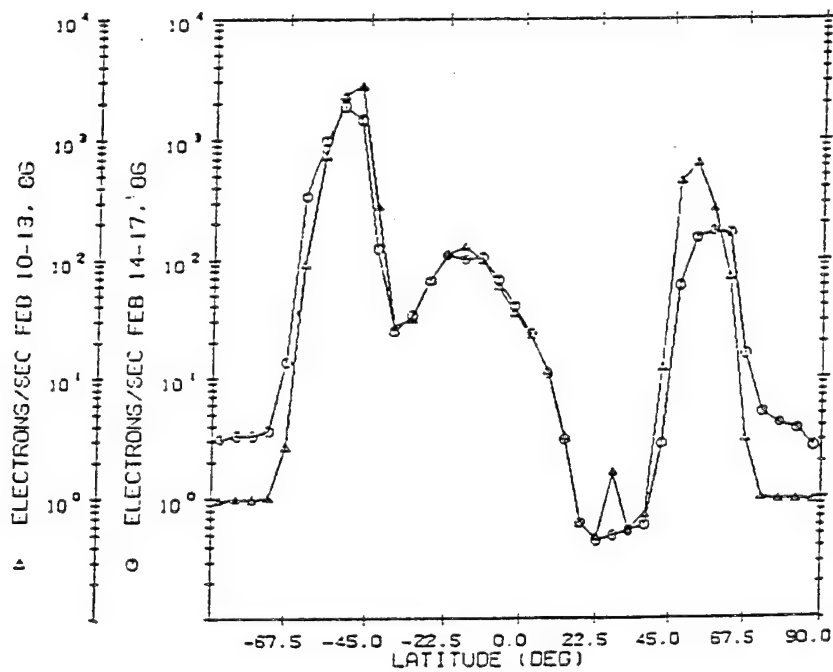


Figure 5b. Particle event between February 14-17 compared to the same quiet period.

To summarize, the latitudinal dependence of the proton component of a particle event seems to show little change with the level of geomagnetic activity. On the other hand, electron entry into the magnetosphere appears to be sensitive to the presence of the magnetic storm.

#### 1.4.2 Comparisons of Flare Related Quantities

Next, we studied the temporal variations in a number of flare related phenomena that occurred at or around of the time of observation of the particle events. The profiles of the different components were plotted in Figure 6 between February 5th and 18th, 1986. The phenomena were presented in the chronological order of their observation at the Earth. The top graph gives the electron count rate above 1 MeV obtained from the SSJ\* experiment, while the second one gives the proton count rate above 20 MeV. Both are measured in the first detector of the dosimeter. The two proton events are similar in total intensity and duration. Both events show a quicker leading edge compared to the fall off, although the first event has a much slower rise time than the second, and it also exhibits a curious two peak structure. The arrows at the top of the graph indicate the occurrences of Xray flares of type M or stronger. All of the flares are clustered around one of the two particle events. In each case, we noticed that there are 2-3 precursor flares with the onset of the particle event following the strongest of the Xray flares in the series.

Magnetic sudden commencements, indicated by arrows at the bottom of the second plot, followed the start of both particle events by 3-4 hours.

The third graph depicts the solar wind speed as a function of time. There is distinct evidence of a shock arrival following the first particle event. There are no data available over the time period of the second event.

In the last two graphs, the Kp and Dst indices reveal the geomagnetic activity during the time period of the two events. We noticed a huge magnetic storm during the Feb 6th event, but no activity during the time of the second event.

The chart on the right side gives the time sequencing of the various events. The X-ray flare is followed in about an hour by the arrival of the electron component at the Earth. The protons trail the electrons by another hour or so. The magnetic sudden commencements occur a few hours following particle onset, while the solar wind plasma shock arrives a day or so later. The magnetic storm develops shortly after the arrival of the shock plasma and reaches a peak a day later.

An important observation can be made from the preceding investigation. The magnetic storm develops 1-2 days following the arrival of the particle components at the Earth. If one were to find signatures in the particle events that might indicate that a magnetic storm would follow, one would have a lead time of a day or two in avoiding the hazards that might occur with the storm. It is generally believed that the arrival of a plasma shock, together with a southward IMF, will

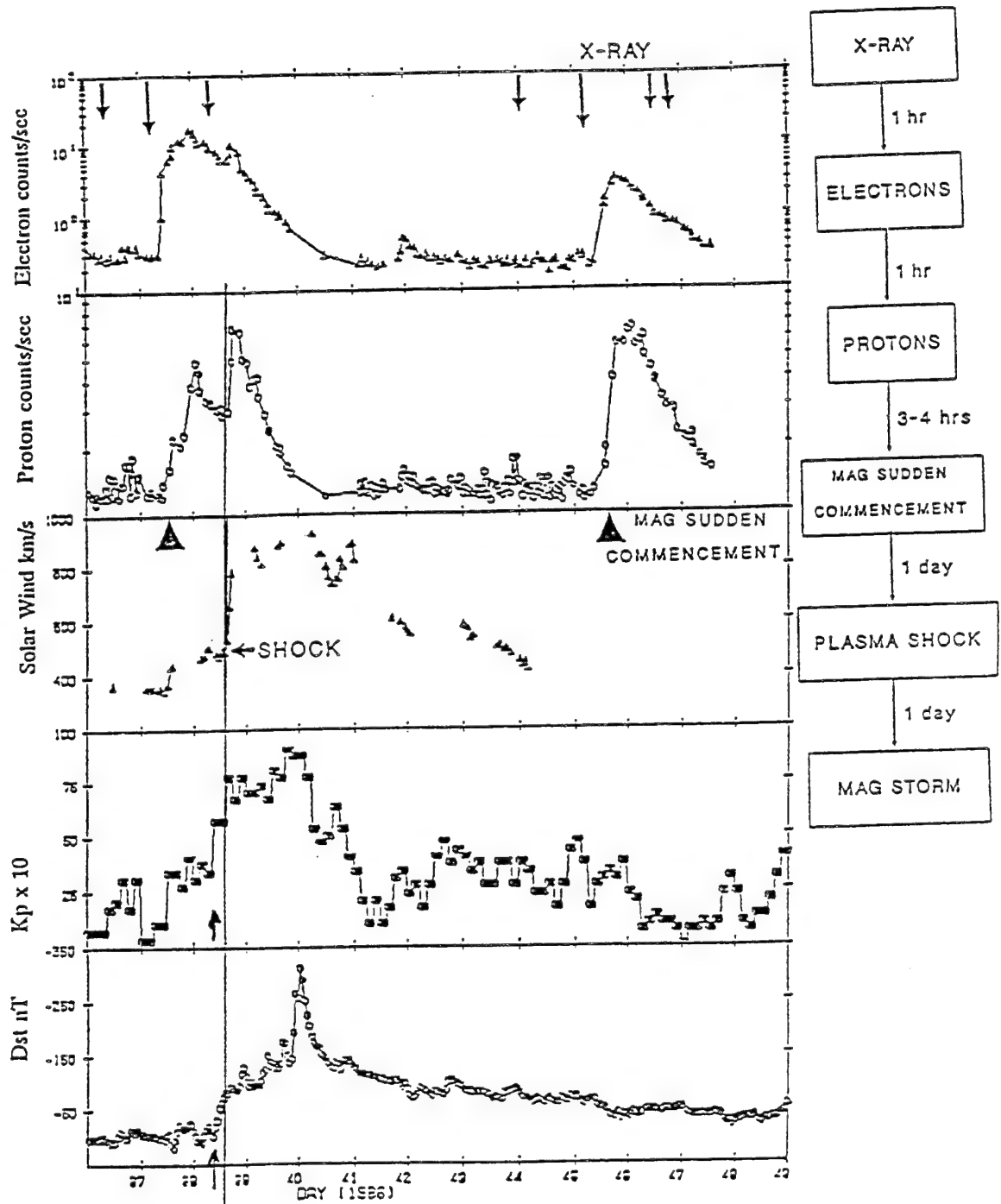


**Figure 6.** Plots of the proton and electron component, solar wind plasma, Kp and Dst indices between February 5th and 18th, 1986. The occurrence of X-ray flares and sudden commencements are also indicated.

lead to a geomagnetic storm. These are not the best indicators for most practical purposes because the storm sometimes occurs concurrently with the southward turning of the IMF, so that no advance warning is obtained.

We investigated major differences in two events to find features that might be significant enough to be used as pointers to the fact that the first event led to or caused a geomagnetic storm, while the second one did not. A comparison of the two particle events is summarized in Table 3. We noticed that the first event was preceded by a stronger X-ray flare than the second, but this is not very significant since there have been larger recorded flares that have not led to magnetic storms, with the converse also being true in that there are major magnetic storms that are not flare related [Smith and Smith, 1963]. Both particle events are followed within an hour of their arrival at the Earth by magnetic sudden commencements (SCs) indicating that the appearance of SCs does not necessarily herald the onset of a magnetic storm. However, if we look at the particle components of the two solar events, some significant differences emerge. The first is that the spectrum of protons is softer in the first event. The second difference is the rise time of the proton component from the background to peak value, which is about twice as long for the first event as it is for the second. Also, the profile of the rising edge is considerably more bumpy in the first case, while it is fairly smooth in the second case. However, the profiles and rise time of the electron component is similar in both cases. Next, we compared the actual fluxes of protons and electrons above 20 MeV and 1 MeV, respectively. Since both sets of counts are recorded by the same detector, the geometrical factors are the same. We note that the first event contains considerably more electrons than protons with energies greater than the thresholds specified above, while the reverse is true for the second event. Finally, we noticed that the fraction of protons gaining access to the polar caps is somewhat smaller during the first event.

In conclusion, we found that there are three important differences in the particle components of the event that was followed by a magnetic storm and the one that was not. The first is that the spectrum of particles at peak is softer in the event that preceded the magnetic storm. The second is that the time taken for the proton component to rise to maximum is considerably slower for this event. Also, there are proportionately more high energy electrons than protons. In the following section, we investigated three other events (numbers 1, 2, 3 in Table 2). The first two were not followed by any geomagnetic activity, while the third one was.

#### 1.4.2.1 Event 1: February 16th, 1984

The particle event of February 16th, 1984 (Figure 7) shows a quick rise to the peak (less than an hour) for both protons and electrons. The peak fluxes for both components are the same, although the electrons, in this case, die out much quicker than the protons - over a period of about 2.5 days. In the period following the event, the Dst index remains predominantly positive, indicating the absence of magnetic storm activity.

TABLE 3. Comparison of Solar Particle Events of February 6th and 14th, 1986			
	Event 1: Feb 6-9, 1986	Event 2: Feb 14-16, 1986	Reference
Particle Events	1. Softer proton spectrum: Differential index of 1 MeV protons at peak = -3.19	= -1.89	IMP-8 CPME data
	2. Slower rise time of protons from start of event to peak. Rise time = 33 hrs 5 mins	= 14 hrs 15 mins	DMSP/F7 SSJ* data
	3. Larger electron flux compared to protons: Peak electron/Proton counts = 3.0	Smaller electron flux: = 0.4	DMSP/F7 SSJ* Electron >1 MeV Proton >20 MeV
	4. Total heavy ion fluence about the same: 54 CNO (21-43 MeV), no Fe (47-80 MeV)	32 CNO, 4 Fe	IMP-8 U. of Chicago Heavy Ion Experiment
	5. Same total dose in flare Total dose = 8.5 rads	= 8.9 rads	DMSP/F7 SSJ*, Detector 1 dose
	6. Fewer protons gain access to polar caps. 37% above 30 MeV 17% above 60 MeV	42% above 30 MeV 23% above 60 MeV	IMP-8 and DMSP/F7 solar proton data
X-ray Flares	7. Particle event followed X1.7 class X-ray flare	Event followed M6.4 flare	GOES 6 X-ray data
	8. 3 precursor flares between February 3-5 ( 1 during proton event)	3 precursors (2 during proton flare)	GOES 6 X-ray data
Solar Wind Plasma and Magnetic Activity	9. Substantial increase in solar wind speed (shock arrival)	No data	NSSDC OMNI data
	10. Magnetic sudden commencements following particle events February 6th, 13:12	February 14th, 14:34	Solar Geophysical Data Prompt Reports
	11. Accompanied by strong geomagnetic storm (largest in 30 yrs)	No storm observed	NSSDC OMNI data

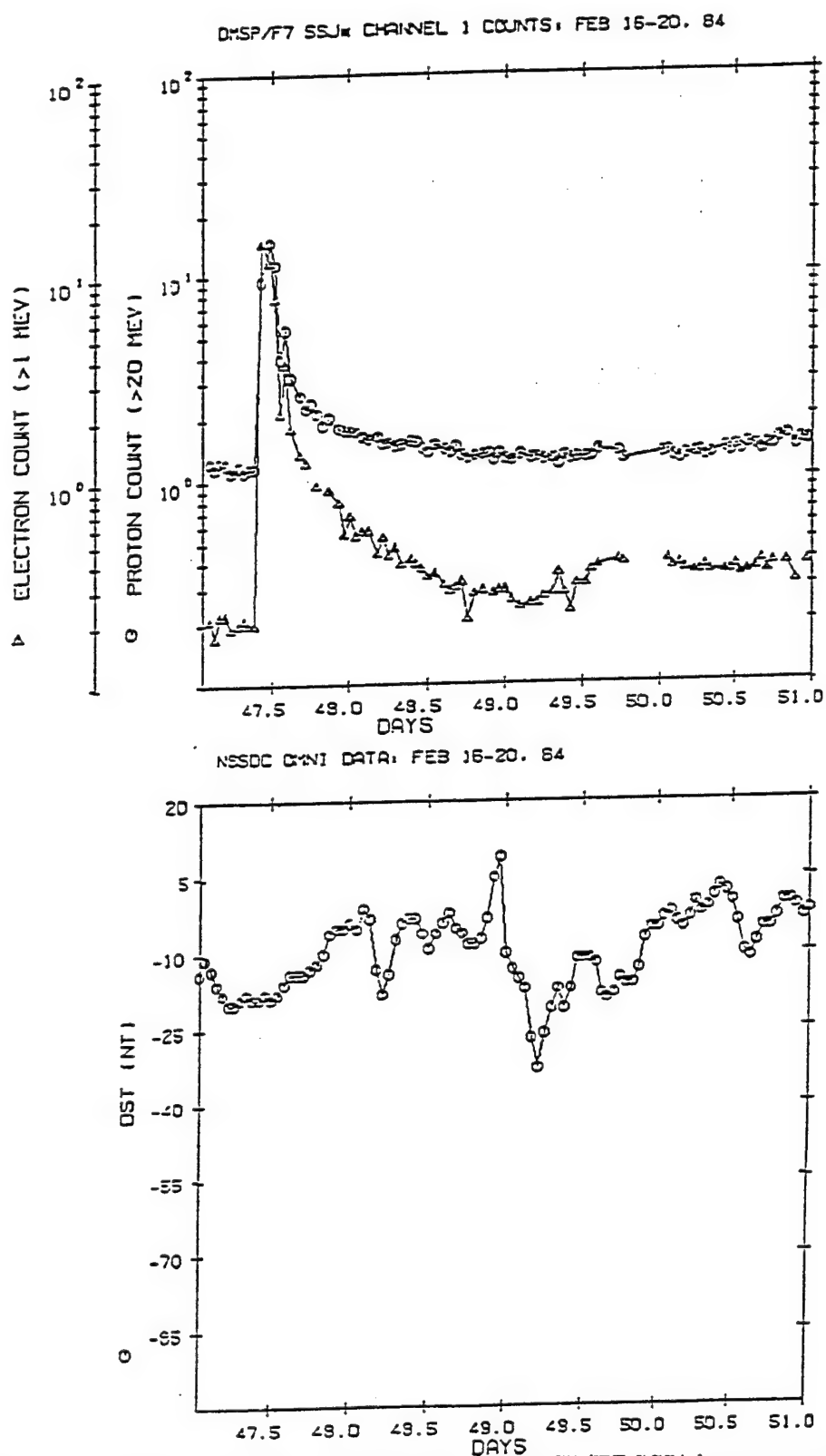


**Figure 7.** Proton and electron count rates in DMSP/F7 SSJ\* instrument during solar particle event of February 16th 1984, and corresponding Dst indices over the time period.



#### 1.4.2.2 Event 2: March 12th, 1984

This event (Figure 8) is similar to the previous one in its particle profiles. We noticed the same sharp rise from the quiet time count rate to the peak. The flux of protons above 20 MeV is comparable to that of electrons above 1 MeV. Again, the magnetosphere is quiet following this event.

#### 1.4.2.3 Event 3: April 26th, 1984

This solar particle event (Figure 9) is distinctly different from the two previous ones. The protons and electrons rise to their peak value over a period of about 2 days. In addition, there are about 5 times as many electrons above 1 MeV as there are protons above 20 MeV. Following the particle event is a geomagnetic storm that reaches a minimum Dst of almost -100 nT.

We observed that the differences seen in the particle events of February 6th and 14th, 1986 are borne out in the three events in 1984.

### 1.5 DISCUSSION AND CONCLUSIONS

In this study, we have not attempted to uncover underlying causes that lead to the precipitation of a geomagnetic storm following a solar particle event, but rather we have pursued an empirical approach to the problem where we studied solar particle events that were followed by geomagnetic storms and ones that were not. We identified consistent differences in the particle components of these two classes of events. Over the polar caps, we noticed that the ratio of high energy electrons to high energy protons was higher in the particle events that were followed by geomagnetic storms. These events also exhibited a longer rise time for the protons, though not for the electrons, suggesting that it is the proton entry onto the polar caps that is inhibited during events that are associated with magnetic activity. Less protons are seen to gain access to the polar caps when there is a magnetic storm. Also, the spectrum of the protons is considerably softer for the storm related events, indicating a preferential access of the lower energy protons in these events. We have verified the above features in a data sample of events spanning half a solar cycle with corresponding particle events of different sizes and energy thresholds.

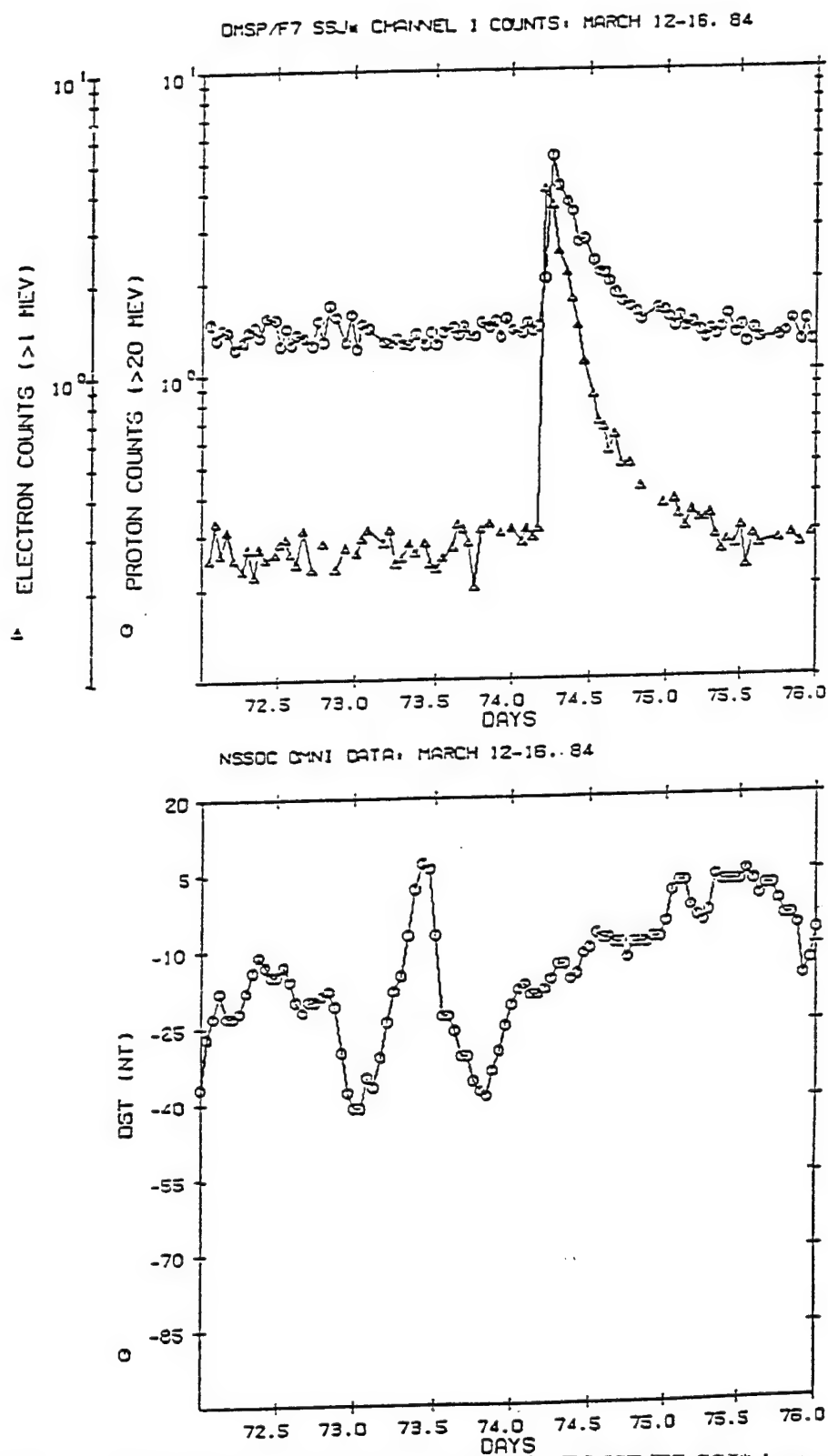


**Figure 8.** Proton and electron count rates in DMSP/F7 SSJ\* instrument during solar particle event of March 14th 1984, and corresponding Dst indices over the time period.

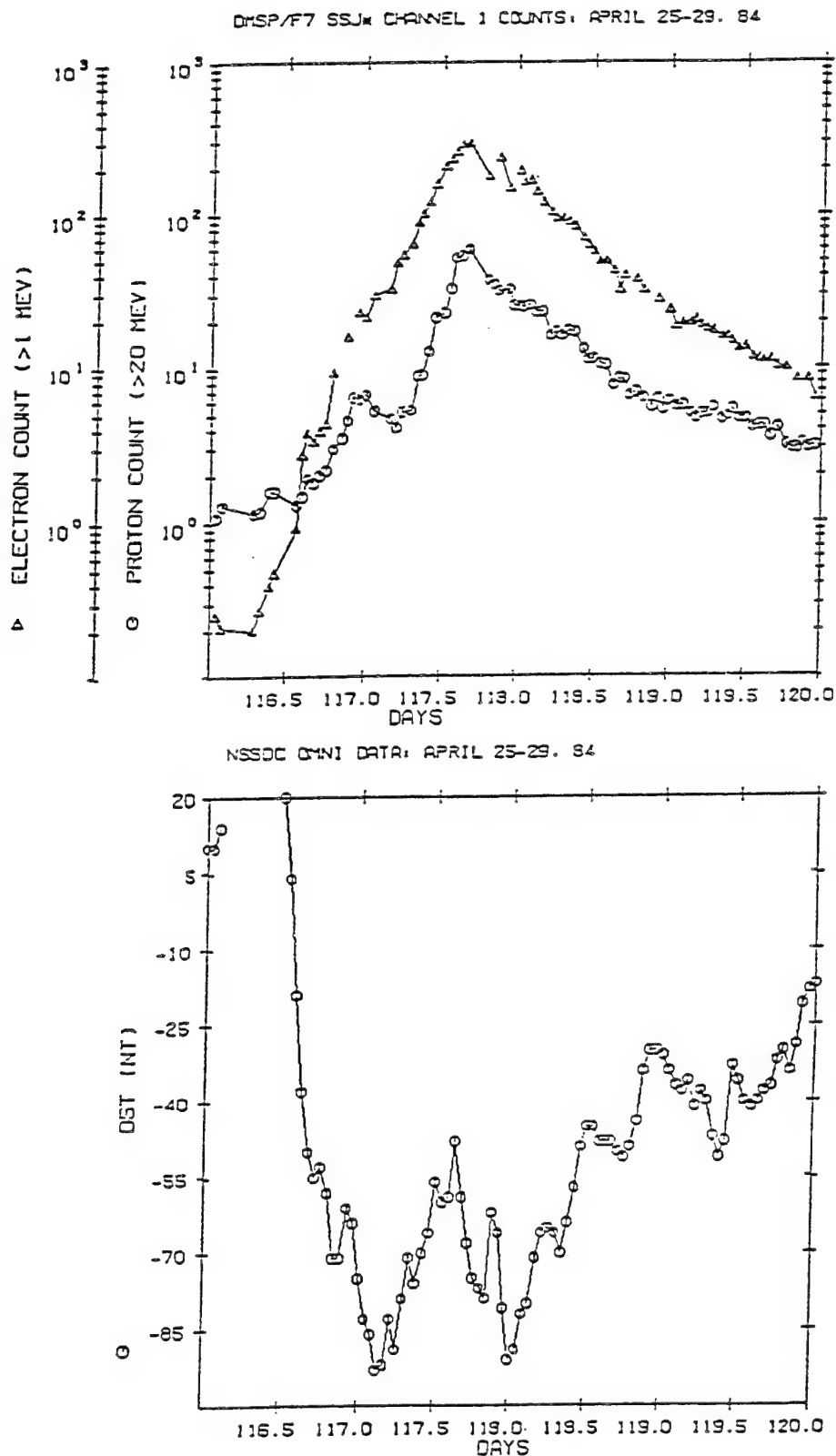


**Figure 9.** Proton and electron count rates in DMSP/F7 SSJ\* instrument during solar particle event of April 24th 1984, and corresponding Dst indices over the time period.

## 2. PROGRAM SSDBGEN - SCIENCE SUMMARY DATA BASE GENERATION

### 2.1 OVERVIEW

The science summary data base (SSDB) will be created in order to give an overview of the dynamical state of the magnetosphere. It will be used as a tool to select events for more extensive study and to help characterize the regions through which the satellite is passing. The software described here was developed from a private communication [Gussenhoven, *et al.*, 1990].

Program SSDBGEN, creates this data base for a CRRES orbit by averaging quantities selected from the time history data bases over time intervals of user-specified size, for example 1 minute. The results are given in geophysical units when possible, otherwise as count rates. Pitch angle information is not used; the particle quantities in the data base are approximately proportional to omnidirectional flux. Selected ephemeris values at the midpoints of the averaging intervals are included. Although the program was operated initially on the CYBER 860 (NOS/VE operating system), a VAX-compatible version was developed for use after the CYBER was removed from operation in September, 1992.

### 2.2 DETAILED SPECIFICATIONS OF SCIENCE SUMMARY DATA BASES

The SSDB consists of time-sequenced records, each containing the selected particle and magnetic field measurement averages for a time interval, plus selected ephemeris values at the midpoint of the interval. Each record contains 24 such "items", including the time at the midpoint of the interval. Some of the items are currently undefined. The data records are preceded by header records describing the contents of the data base. One data base is constructed per orbit, from perigee to perigee.

The SSDB is provided in two forms: packed and unpacked. The packed form represents the data as scaled two-byte integers (except for time, four bytes), while the unpacked form employs the internal 8 byte floating point representation of the host platform (single precision on the CYBER, double precision on the VAX). The packed integers (I) are converted to real numbers (R) by the formula

$$R = \text{OFFSET} + I \cdot \text{SCALE} \quad (2.1)$$

where OFFSET and SCALE are defined in a header for each data item. The unpacked form appears to be the most reliable for the foreseeable future, until a set of dependable scales and offsets can be formulated. For portability to other computer systems, auxiliary programs exist for converting the unpacked files to ASCII.

The ephemeris values are the L value, the solar magnetic latitude (deg), the solar magnetic local time (hr) and the model magnetic field magnitude (nT). The particle/field instruments and channels are given in Table 4. The magnetic field is given in nT. The fluxes are in particles/(cm<sup>2</sup>-sec-MeV-sr), except for those items indicated as "count rate", which are given as counts/sec. Whenever possible a backup channel and instrument is given, to be used in case of in-flight problems with the preferred instrument and channel.

**TABLE 4.** Science Summary Data Base Instruments and Channels

Quantity	Preferred	Backup
Measured Magnetic Field Magnitude	Fluxgate Magnetometer	
Electron Flux: 4-5 MeV	HEEF AFGL-701-4 L6-L7	Dosimeter AFGL-701-2 3rd LOLET Flux Channel
Electron Count Rate: > 2.5 MeV	Dosimeter AFGL-701-2 2nd LOLET Flux Channel	MEES AFGL-701-5A Channel 17
Electron Flux: 1-1.5 MeV	HEEF AFGL-701-4 LL-L1	MEES AFGL-701-5A Channel 10
Electron Flux: .2-.3 MeV	MEES AFGL-701-5A Channel 2	EPAS AFGL-701-5B Look Direction 90°
Electron Count Rate: 20-285 keV	EPAS AFGL-701-5B Look Direction 90°	MEES AFGL-701-5A Channel 0
Helium Count Rate: > 45 MeV/Nucleon	ONR-604 P2	
Star Count Rate: Threshold > 75 MeV	Dosimeter AFGL-701-2 4th VHILET Channel	
Proton Count Rate: > 35 MeV	Dosimeter AFGL-701-2 2nd HILET Flux Channel	Proton Switch AFGL-701-7B > 50 MeV
Proton Flux: 50 MeV	PROTEL AFGL-701-9 HEH # 13	
Proton Flux: 3 MeV	PROTEL AFGL-701-8 LEH # 5	
Electron Flux: .55-.65 MeV	MEES AFGL-701-5A Channel 6	

The count rates are obtained by dividing the counts by the accumulation interval (Table 5).

TABLE 5. Accumulation Intervals	
Instrument	Accumulation Interval, sec
HEEF	0.512
MEES	0.512
EPAS	0.512
PROTEL	1.024
Dosimeter	4.096
ONR-604	4.096
Proton Switch	4.096

For MEES, the counts are first corrected by subtracting the background counts, given in Channel 16. For HEEF, the counts in the 10 differential channels are corrected for the front solid state detector dead time by multiplication by the factor:

$$M_F = \frac{1}{[1 - \tau_0(WF/\delta T)] [1 - \tau_0(SF/\delta T)]} \quad (2.2)$$

where  $\tau_0$  is the electronics dead time,  $1.1 \times 10^{-6}$  sec. and  $\delta T$  is the accumulation time, 0.512 sec. WF and SF depend on which differential channel is being corrected. For the lowest three energy channels, the W2F and S2F counts are used, while for the remaining seven, the W1F and S1F counts are used.

The flux (differential in energy and direction) is computed by :

$$\text{Flux} = \text{Count rate}/(\text{efficiency} \times \text{geometric factor})$$

The efficiencies and geometric factors have been supplied by the principal investigators (PI's) for HEEF, MEES, and PROTEL. Except for PROTEL, the efficiencies are unity.

Normally the instrument/channel used for a specific particle quantity is selected on the basis of THDB availability. The preferred instrument is selected if its THDB is available; otherwise the backup instrument is used, or if neither is available, then the quantity is omitted from the SSDB. The user can optionally mandate that only the preferred instrument may be used, or that only the backup instrument may be used. In this case, the quantity will be omitted if the mandated THDB is not available.

The magnetic field magnitude is given in nT. For the fluxgate magnetometer, the calibration constants are updated frequently by the principal investigator. Therefore, this instrument may

be used only if the calibration file is available for the desired orbit. The conversion from counts to nT is performed using this file and the code provided by the principal investigator in the VAX README.DOC directory. When the measured magnetic field is supplied, an additional quantity is included in the SSDB: the fractional difference between the measured and model magnetic field magnitude.

## 2.3 PROGRAM OPERATION

### 2.3.1 Time History Data Bases

SSDBGEN looks for the time history data bases in the current working catalog. It uses the standard naming format: Ammmnnnn (the VAX version adds the extension .DAT), where A is the letter P for the dosimeter, or T for the other instruments; mmm is the instrument designator (Table 6): and nnnn is the four-digit orbit number, right-adjusted with zero fill.

<b>TABLE 6. Time History Data Base Instrument Designators</b>	
<b>Instrument</b>	<b>Designator</b>
Dosimeter	002
HEEF	004
MEES	05A
EPAS	05B
PROTEL	008
Proton Switch	07B
ONR-604	604
Fluxgate Magnetometer	131

If the file with the appropriate name does not exist on the current working catalog, SSDBGEN assumes that the data for that instrument is not available.

### 2.3.2 Calibration Files

At present a calibration file is used only for the fluxgate magnetometer. This must be copied to the working catalog under the name MAGCAL, if magnetometer data are to be included. Cal constants for the other instruments are built into instrument-specific code which determines the conversion factors from counts to geophysical quantities.

### 2.3.3 Ephemeris File

The CYBER version used the binary ephemeris file stored on the RMS family disk under the name

:RMS.CRESEPH.CERnnnn0

where nnnn is the orbit number. The VAX version uses the standard THDB file, under the name E000nnnn.DAT.

### 2.3.4 User Inputs

SSDBGEN interactively prompts the user for values of various parameters controlling the run. These are described in the following.

### 2.3.5 Orbit Number

*Definition of L-dependent averaging intervals:* the length of the averaging interval is allowed to depend on L. It is constant within each of the set of user-defined L segments. The default is a 1 minute averaging interval for  $L < 4$ , 10 minutes for  $L > 4$ . The user is asked if he wants to override this default. If the response is Y, then the following inputs are required:

### 2.3.6 Number of L segments

*Length of averaging interval and maximum L value for each L segment:* the maximum L value of each segment is assumed to be the minimum value for the next. The minimum value of the first segment is zero; the maximum of the last is infinite (user input ignored).

*Backup Source Flags:* These have the value +1, 0, or -1. The default is 0, meaning that if the preferred source (instrument/channel) for a data item is not available, and the backup is, then the backup is used. If the backup source flag for an item is +1, then the backup is to be used even if the preferred source is available. If the backup flag for an item is -1, then the backup will not be used under any circumstances. The user is first asked if any of the defaults (set to 0 for all flags) are to be overridden. If the response is Y, then SSDBGEN prompts the user for a value for each of the backup flags.

*Confirmation of choices:* The user is asked if he wishes to confirm the choices of sources selected by SSDBGEN for the various data items, in accordance with the THDB file availabilities and backup flags. If the response is Y, the source selected for each item is displayed. If the user responds N to any selection the program is terminated.

*Packed and unpacked output file names:* character strings, maximum length 50 characters.



### 2.3.7 SSDB Output File Formats

The packed and unpacked science summary data bases created by SSDBGGEN are in internal binary (FORTRAN unformatted). Each file begins with several header records, in character mode. These headers are followed by the data records, one per averaging interval. Each data record contains 24 items, including the universal time, some of which are currently undefined. The packed file size is ~42 kbytes, and the unpacked file size is ~125 kbytes.

#### *Header Records:*

There are 4 types of header records:

- Type 1. Orbit/date identifier
- Type 2. L-dependent averaging interval definitions
- Type 3. Item and source descriptions
- Type 4. (Packed file only) Offsets and scales

Each record should be read, as a binary record, into a character string. The character string may then be subdivided into its contents by a formatted internal read. The following describes the contents of the header records, by type, and the format for subdividing the record into its contents.

- Type 1. Year, day number in year, orbit number, number of type 2 header records (L segments) to follow (I4,1X,I3,1X,I5,1X,I5)
- Type 2. One record per L segment: Maximum L value of segment, and averaging interval in seconds(6X,F4.1,3X,F7.1)
- Type 3. One record for each of 24 items: descriptions of the item and its source, blank for the undefined items (A50,10X,A50)
- Type 4. (Packed files only) One record per item: offset and scale for that item (2E15.8)

#### *Data Records:*

Each data record consists of 24 items. In the unpacked data base these are 8-byte real numbers (single precision on the CYBER, double precision on the VAX), the first of which is the universal time, in sec. Undefined items, those for which there were insufficient data in the interval, or those for which no source was available, are assigned the value  $-9.9 \times 10^{99}$  in the CYBER version,  $-1 \times 10^{30}$  on the VAX version. MEES items for which averaged background counts exceed average measured counts are assigned the value  $-9.0 \times 10^{99}$  in the CYBER version,  $-0.5 \times 10^{30}$  on the VAX version. In the packed data base, the first item in each record is the universal time, in msec, as a 4-byte integer. The remaining 23 items are 2-byte integers. Items for which there is no valid value (undefined items, insufficient data, or lack of available

source) are assigned the value -1; MEES items for which background counts exceed measured counts are assigned the value -5. If any of the scaled values of a data record would overflow the allocated 2 bytes, each of them, and the time, are replaced in the record by negative values, and the data are rewritten in the following record in the same format as in the unpacked data base, 8 byte reels.

## 2.4 PROGRAM STRUCTURE AND LOGIC

Figure 10 depicts the organizational structure of the program. A subroutine is called by the module directly linked to it from above. Thus the main program, SSDBGEN, calls CHKTHDB, SETITEMS, and DELTAVE; CHKTHDB, in turn, calls NAME and READCAL. READCAL calls instrument-specific routines (Table 7) to collect the required calibration information for each instrument. Instrument-specific routines called by subroutine GETOFFSC set the offsets and scales for the packed data bases; those called by subroutines GETITINST and GETSAMP acquire data from the time-history data bases. It is anticipated that such instrument-specific processing will be modified from time to time in the future. Implementation of such changes would be restricted to these instrument-specific routines. Brief descriptions of each of the functions of the other modules are given in Table 8. Also listed are the principal common blocks and the significant parameters they contain.

TABLE 7. Instrument-Specific Subroutines			
Instrument	Called by READCAL	Called by GETOFFSC	Called by GETITINST and GETSAMP
Magnetometer	MAGNETCAL	MAGNETOS	GETMAG
Dosimeter	DOSECAL	DOSIMOS	GETDOS
HEEF	HEEFCAL	HEEFOS	GETHEEF
MEES	MEESCAL	MEESES	GETMEES
EPAS	EPASCAL	EPASOS	GETEPAS
ONR-604	ONR604CAL	ONR604OS	GETONR604
PROTEL	PROTCAL	PROTELOS	GETPROT
Proton Switch	PRSWCAL	PROTSWOS	GETPRSW

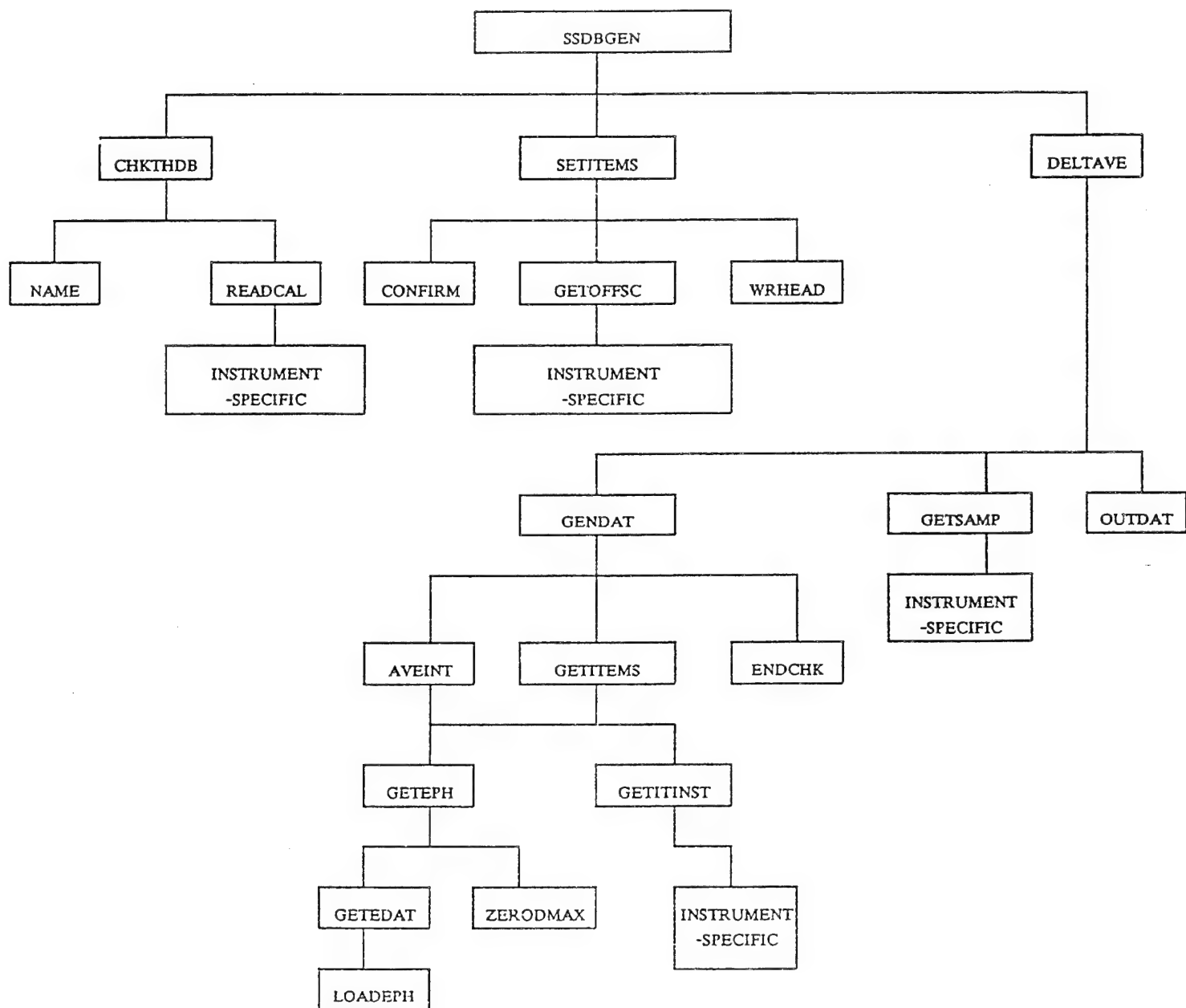


Figure 10. Program organization.

TABLE 8. Functional Descriptions	
Module	Description
AVEINT	Determine the size of the averaging interval
CHKTHDB	Determine the availability of THDB files
CONFIRM	User confirmation of source selection
DELTAVE	Generate and output the SSDB data records
ENDCHK	Check for end of all instrument data
GENDAT	Generate the values for one data record
GETEDAT	Get the next ephemeris record
GETEPH	Obtain the ephemeris values for a given time
GETITEMS	Get the items required from a THDB or ephemeris for a given time interval
GETITINST	Get the required values from a THDB
GETOFFSC	Set the offsets and scales for the packed SSDB file
GETSAMP	Get a THDB data record
LOADEPH	Read the RMS ephemeris file into a common block (CYBER version only)
NAME	Construct THDB file names
OUTDAT	Output the data records to the SSDB packed and unpacked files
READCAL	Read or set calibration constants
SETITEMS	Select source for each item in the SSDB
SSDBGEN	Main Program
WRHEAD	Open packed and unpacked output SSDB files; write headers to them
ZERODMAX	Place a value into the interval 0-DMAX
COMMON Blocks	
SSDB	Item descriptions and source identifications; Orbit number and date; Offsets and scales
DTSEG	Parameters defining averaging interval sizes vs. L
AVE	Accumulators and sample counts for current interval; Start and end times; THDB end-of-file flags
HEDCOM	RMS file header information (CYBER version only)
POSCOM	RMS Ephemeris Records (CYBER version only)

After reading in the user input described above, the main program calls subroutine CHKTHDB to determine the availability of the various THDB files, i. e., it inquires, for each THDB, whether or not a file of the appropriate name, according to the above-described naming convention, exists. Flags are set indicating the existence, or non-existence, of each file. For each THDB that exists, the calibration information is read in, or set from internally stored constants, by instrument-specific routines called by READCAL.

Once the availability of the various files is known, SSDBGEN invokes subroutine SETITEMS, to select the source (THDB and channel) to be used for each item in the SSDB. The results are saved in a common block, along with a cross- reference table indicating, for each THDB, channel numbers that will be required. SETITEMS next invokes subroutine CONFIRM, if the user request direct confirmation of the sources selected, GETOFFSC to set the offsets and scales for the packed data base, and WRHEAD to open the packed and unpacked SSDB files, and write the headers to them.

SSDBGEN then invokes subroutine DELTAVE to perform the rest of the processing: generating and outputting the SSDB data records. First, DELTAVE determines the starting time of the first time interval for output. This is done by reading each instrument THDB (subroutine GETSAMP) and determining the time (truncated to minutes UT) of the earliest data. DELTAVE, then, alternately calls subroutines GENDAT and OUTDAT to generate and output, respectively, the values for the successive time intervals, one record per interval, terminating the loop when end-of-file has been reached on all instrument THDB's, as signaled by subroutine ENDCHK. GENDAT first determines the start and end times of the interval. The start time is equal to the end time of the previous interval, except for the first interval, as just described. AVEINT is called to determine the size of the interval from the L value at the starting time, in accordance with the specifications in the user input. The ephemeris routines are invoked by AVEINT to obtain the required L value. Once the start time and size (therefore, also the end time) of the interval have been determined, GETITEMS is invoked to construct the data for the SSDB record for that interval. GETITEMS, in turn, invokes GETEPH to obtain the ephemeris values at the midpoint of the interval, and GETITINST to obtain the THDB instrument values, averaged over the interval.

## 2.5 AUXILIARY PROGRAMS

In addition to SSDBGEN, several useful related programs have been developed. The first of these converts the unpacked SSDB file to ASCII for convenient transmittal of the data to other computer systems. The other programs discussed here create specialized, instrument-specific data bases, in formats identical to the general SSDB.

### 2.5.1 Conversion to ASCII - Program SSDBASCII

Program SSDBASCII converts an unpacked SSDB file to an ASCII file. The user is prompted for the names of these files. It begins with copies of the header records, except for the last six, which describe the last 6 presently undefined data items. Each header record is preceded by a blank. The first 18 items of each data record are converted to 9E13.5, as shown. This occupies two lines of output. The remaining six, presently undefined, items are omitted. Note that other undefined items, those for which there were insufficient data in the interval, or those for which no source was available, are assigned the value  $-1.0 \times 10^{30}$ . MEES items, for which the background counts exceeded the measured counts, are assigned the value  $-0.5 \times 10^{30}$ . A blank line separates consecutive data records.

### 2.5.2 Instrument-Specific Programs

These programs differ from SSDBGGEN only in the main module, where the preferred and backup sources for the various data items are defined. They may be operated exactly as the general program SSDBGGEN. The programs available and the instruments (channels) to which they apply are given below.

SSDBDOSGEN - SPACERAD Dosimeter Flux Channels

SSDBHEEFGEN - HEEF differential channels

SSDBMEES1GEN - MEES E0-E8

SSDBMEES2GEN - MEES E9-E16

SSDBLEGEN - PROTEL LEH 1-8

SSDBHE18GEN - PROTEL HEH 1-8

SSDBHE916GEN - PROTEL HEH 9-16

SSDBPSGEN - Proton Switch

### 3. THE CRRES MICROELECTRONICS PACKAGE DATA PROCESSING SYSTEM

The CRRES Microelectronics Package (MEP) data processing software must recognize 141 different data packet headers and unpack the parameter bytes accordingly. The time of the measurements is determined by monitoring the time pulses embedded in the data stream. Missing data and time jumps must be accounted for, if this is to be done accurately. Software has been developed for the NOS/VE environment in parallel with the RTDS (Real Time Data Acquisition System) package. The complete processing system, input and output data formats, and samples of the various print-outs and plots are described in this report.

#### 3.1 MEP SERIAL TELEMETRY

The GL 701-1A data files (format shown below in Table 9) are composed of a series of 7080 byte records, each containing 8 master (major) frames [Griffin, 1989]. The first eight bytes of a master frame give the current universal time and vehicle time code word (VTCW). A master frame occurs every 4.096 seconds and yields 32 minor frames of five bytes for a total of 160 bytes of serial telemetry data (science words) [*CRRES Microelectronics Package Serial Telemetry Manual*, 1989]. These are bytes 10-14 of each minor frame, as shown in Table 9. The remaining 22 bytes of each minor frame are not used in this processing.

TABLE 9. GL 701-1A Data File Format	
Byte Number	Contents
1-4	Universal Time (ms) for minor frame 0
5-8	Vehicle Time Code Word for minor frame 0
9	Frame counter
10-14	Science words for minor frame 0
15	B35 for minor frame 0
16-35	Subcom words 0-19 for minor frame 0
36-62	Repeat order of bytes 9-35 for minor frame 1
.	.
.	.
846-872	Repeat order of bytes 9-35 for minor frame 31
873-1744	Repeat order of bytes 1-872 for second master frame
.	.
.	.
6105-6976	Repeat order of bytes 1-872 for eighth master frame
6977-7080	Vacant (0 filled)

The first minor frame of each master frame contains a fixed set of status indicators, including a 24 bit segment (512 millisecond resolution) of the 32 bit MEP internal software clock. The remaining 155 bytes of serial data are interpreted as a packetized stream, where each packet is identified by a one byte header [*CRRES Microelectronics Package User's Guide*, 1989]. The header implies both the length and contents of the packet; the complete packet formats are defined in the *CRRES Microelectronics Package Serial Telemetry Manual* [NRL, 1989]. Two of the 141 packet types are variable length, and include a packet length specifier immediately following the header byte. Note that the minor frame divisions within a master frame are arbitrary, as the entire 155 bytes are treated as a single stream. However, the packets are not permitted to overlap master frame boundaries. If the next packet will not fit in the current master frame, or if there is no packet waiting to be transmitted, a null packet is sent. A null packet is simply a header byte of \$0F (hexadecimal 0F) and serves only as a place holder. Empty (unused) master frames at the end of an orbit are "1's filled."

Data may be missing due to telemetry dropout for a portion of a master frame. In this case, the serial data is "1's filled", containing header bytes of \$FF. When this occurs, the remainder of the master frame must be discarded. Otherwise, it is impossible to re-synchronize on a packet header. If there is telemetry dropout anywhere within a master frame, the most significant bit of the VTCW is set to 1 [Griffin, 1989]. No filling is necessary if there is dropout for a complete master frame.

The serial data includes "time tick" packets, which report the status of the internal software clock once every eight minor frames (1.024 seconds). Therefore, the time of occurrence of an event may be accurately determined even if the telemetry buffer is being filled at a rate greater than the data transmission rate. This buffer overflow may occur during periods of extremely high activity, which typically result from the detection of a large number of Single Event Upsets (SEU's). The correlation between the internal software clock (time tick values) and universal time is given by the time values at the start of the record. If two successive time ticks are separated only by the proper number of null packets (i.e, the telemetry buffer is not full), the second time tick packet may serve as a reference for the correlation between MEP time and the VTCW. The vehicle time code word is known at a resolution of 128 ms because its least significant bit is equivalent to one minor frame.

## 3.2 MEP DATA PROCESSING SYSTEM

### 3.2.1 MEP Serial Data Processing and Archiving

The MEP serial data processing begins with the creation of a sequential listing of the MEP data packets, which is performed by the program READMEP. This program reads the GL 701-1A file along with the associated header file, and creates a time sequential event history, presenting all serial data, except JPL Timing and Transistor packets, in a text format. The volume of JPL data is quite high (approximately four megabytes per orbit), and since this data is not of particular interest to PL researchers, it is stored separately in a compact binary format. Null



packets are discarded, and time tick packets are processed internally so that all other data packets may be time tagged. Table 10 shows a sample of READMEP output for orbit 703 (the right column shows universal time in seconds).

These files are transferred to PC's using the high speed Ethernet link, and compressed using the popular PKZIP utility. Typical compression achieved is approximately 85%; the .ZIP files are then archived on two Bernoulli disks. The binary version of the time history is also saved on NOS/VE, and serves as the input for the second program, READSEQ.

Each run of the READMEP program generates an update to the "Audit" file, which serves as a quick reference for the entire MEP data processing system. A separate program is run periodically to sort this file, since orbits are not necessarily processed in order; a sample is shown in Table 11 below.

Each entry includes the time of the run, the date of creation of the GL 701-1A file, and data time ranges (including separate ranges for JPL and 4007 Inverter data). Time range entries of -1.000, such as for JPL data during orbit 3, indicate that no data of the particular type was received during the orbit. Statistics on anomalies such as time jumps, data fills, and data dropouts are also maintained. Note in the sample that data for orbit 4 was released nearly three months later than data from other early CRRES orbits.

READMEP also creates a number of auxiliary data files for delivery to other research facilities. The complete file production and delivery system is illustrated in Figure 11. JPL Transistor, JPL Timing, Temperature, and Dosimeter files are sent to Jet Propulsion Labs over the SPAN network each time a batch of orbits is processed. NASA Goddard receives 4007 Inverters, Temperature, Dosimeters, and other selected Total Dose data on 1.2 Mb floppy disk. Rate Meter and Pulse Height Analyzer (PHA) files are delivered to Clemson University on 1.44 Mb floppies. Both NASA Goddard and Clemson receive data as sufficient volume accumulates, generally every several hundred orbits.

READSEQ reads the READMEP output file and sorts the data packets into five categories: Commands, SEU Commands, SEU Events (separate files for each ICU and block), Housekeeping, and Total Dose. The files created in this stage utilize table structures where possible to facilitate data retrieval. For example, a series of DUT Power measurements, such as the one shown above, is collected and saved as one unit even though other packets may interrupt the power dump (see sample in Table 12 below). These interruptions occur because SEU information (including Rate Meter data) has the highest priority in the telemetry system. Only the initial and final times of the power dump are saved, since the exact times of the individual measurements are not critical for analysis. The output files are merged into databases that are sorted by orbit number and maintained as permanent files on NOS/VE.

**TABLE 10. Sample of READMEP Output, Orbit 703**

Soft SEU - ICU B Address 025B Mask: 01 Pat: 1	57233.516
Block: C4-2 (Am92L44CDB)	
DUT Block Power Measurement, ICU B: Block E4 = .013 Amps	57235.564
Rate Meter Data Update ICU B Counter A = 00 Counter B = 01	57237.612
DUT Block Power Measurement, ICU B: Block E5 = .007 Amps	57239.660
Rate Meter Data Update ICU B Counter A = 00 Counter B = 00	57239.660
DUT Block Power Measurement, ICU B: Block E6 = 0.000 Amps	57243.756
DUT Block Power Measurement, ICU B: Block E7 = .005 Amps	57247.852
DUT Block Power Measurement, ICU B: Block E8 = .002 Amps	57251.948
DUT Block Power Measurement, ICU B: Block E9 = .002 Amps	57256.044
DUT Block Power Measurement, ICU B: Block EA = .003 Amps	57260.140
DUT Block Power Measurement, ICU B: Block EB = 0.000 Amps	57264.236
DUT Block Power Measurement, ICU B: Block EC = .013 Amps	57268.332
DUT Block Power Measurement, ICU B: Block ED = .007 Amps	57272.427
Rate Meter Data Update ICU B Counter A = 01 Counter B = 00	57274.475
DUT Block Power Measurement, ICU B: Block EE = 0.000 Amps	57276.523
Rate Meter Data Update ICU B Counter A = 00 Counter B = 00	57276.523
Soft SEU - ICU B Address 00DC Mask: 20 Pat: 1	57278.571
Block: C11-2 (Am93422DM)	
Soft SEU - ICU B Address 012F Mask: 20 Pat: 1	57278.571
Block: C11-3 (N82S212F/883B)	
DUT Block Power Measurement, ICU B: Block EF = .005 Amps	57280.619
Rate Meter Data Update ICU B Counter A = 00 Counter B = 01	57281.643
Rate Meter Data Update ICU B Counter A = 00 Counter B = 00	57283.691
DUT Block Power Measurement, ICU B: Block F0 = 0.000 Amps	57284.715
DUT Block Power Measurement, ICU B: Block F1 = 0.000 Amps	57288.811
DUT Block Power Measurement, ICU B: Block F2 = 0.000 Amps	57292.907
DUT Block Power Measurement, ICU B: Block F3 = 0.000 Amps	57297.003
DUT Block Power Measurement, ICU B: Block F4 = 0.000 Amps	57301.099
DUT Block Power Measurement, ICU B: Block F5 = 0.000 Amps	57305.195
DUT Block Power Measurement, ICU B: Block F6 = 0.000 Amps	57309.291
DUT Block Power Measurement, ICU B: Block F7 = 0.000 Amps	57313.387
DUT Block Power Measurement, ICU B: Block F8 = 0.000 Amps	57317.483
DUT Block Power Measurement, ICU B: Block F9 = 0.000 Amps	57321.579
DUT Block Power Measurement, ICU B: Block FA = 0.000 Amps	57325.675
DUT Block Power Measurement, ICU B: Block FB = 0.000 Amps	57329.771
DUT Block Power Measurement, ICU B: Block FC = 0.000 Amps	57333.867
DUT Block Power Measurement, ICU B: Block FD = 0.000 Amps	57337.963
DUT Block Power Measurement, ICU B: Block FE = 0.000 Amps	57342.059
Soft SEU - ICU B Address 0D12 Mask: 02 Pat: 1	57346.155
Block: C6-5 (WH VHSIC)	
DUT Block Power Measurement, ICU B: Block FF = 0.000 Amps	57346.155
ICU B TD Reference +0 Volt Ref. measured 0.000 Volts	57358.443
ICU B TD Reference +10.000 Volt Ref. measured 9.997 Volts	57362.539
ICU B TD Reference ICU Temperature measured 17.952 C	57366.634
ICU B TD Reference ICU +5 V. Supply measured 5.302 Volts	57370.730
ICU B TD Reference ICU +10 V. Supply measured 9.997 Volts	57374.826
ICU B TD Reference ICU +15 V. Supply measured 14.994 Volts	57378.922
ICU B TD Reference ICU -15 V. Supply measured -15.080 Volts	57383.018
ICU B TD Reference Ext +5.000 V. Ref. measured 4.988 Volts	57387.114

TABLE 11. Sample of Update to the "Audit" File

```

ORBIT      3 DAY 90208 CREATED 1990249 PROCESSED 1990-09-06 12:00:02
FILL MIN FR: 36 MISS MAST FR: 3 TIME RANGE: 18239.948 TO 40679.744
JPL RANGE: -1.000 TO -1.000 4007 RANGE: -1.000 TO -1.000
FILLS: 0 DROPOUTS: 12 NEW CODES: 8 RECORDS: 685
READSEQ PROCESSING COMPLETED FOR ORBIT 3: 1990-09-06 12:00:56
ORBIT      4 DAY 90208 CREATED 1990303 PROCESSED 1990-12-13 17:35:44
FILL MIN FR: 1462 MISS MAST FR: 215 TIME RANGE: 40501.535 TO 76138.592
JPL RANGE: 75091.045 TO 76135.520 4007 RANGE: 71904.374 TO 72690.802
FILLS: 3 DROPOUTS: 43 NEW CODES: 142 RECORDS: 1061
READSEQ PROCESSING COMPLETED FOR ORBIT 4: 1990-12-13 17:50:10
ORBIT      5 DAY 90208 CREATED 1990276 PROCESSED 1990-10-04 14:31:21
FILL MIN FR: 285 MISS MAST FR: 65 TIME RANGE: 75960.511 TO 111658.976
JPL RANGE: 75960.511 TO 111655.904 4007 RANGE: 108157.941 TO 108944.369
FILLS: 0 DROPOUTS: 7 NEW CODES: 11 RECORDS: 1082
READSEQ PROCESSING COMPLETED FOR ORBIT 5: 1990-10-04 14:35:35
ORBIT      6 DAY 90209 CREATED 1990257 PROCESSED 1990-09-14 11:20:15
FILL MIN FR: 29 MISS MAST FR: 15 TIME RANGE: 25080.767 TO 60779.360
JPL RANGE: 25080.767 TO 43853.837 4007 RANGE: 58017.639 TO 58806.117
FILLS: 0 DROPOUTS: 1 NEW CODES: 1 RECORDS: 1088
READSEQ PROCESSING COMPLETED FOR ORBIT 6: 1990-09-14 11:30:17
ORBIT      7 DAY 90209 CREATED 1990257 PROCESSED 1990-09-14 12:52:53
FILL MIN FR: 45 MISS MAST FR: 11 TIME RANGE: 60601.151 TO 96299.616
JPL RANGE: 61218.620 TO 80135.877 4007 RANGE: 94283.372 TO 95071.847
FILLS: 0 DROPOUTS: 2 NEW CODES: 0 RECORDS: 1089
READSEQ PROCESSING COMPLETED FOR ORBIT 7: 1990-09-14 13:00:47
ORBIT      8 DAY 90210 CREATED 1990260 PROCESSED 1990-09-18 09:25:11
FILL MIN FR: 36 MISS MAST FR: 4 TIME RANGE: 9721.535 TO 45359.616
JPL RANGE: 11080.376 TO 29997.778 4007 RANGE: 44120.582 TO 44911.106
FILLS: 0 DROPOUTS: 1 NEW CODES: 2 RECORDS: 1088
READSEQ PROCESSING COMPLETED FOR ORBIT 8: 1990-09-18 09:30:14

```

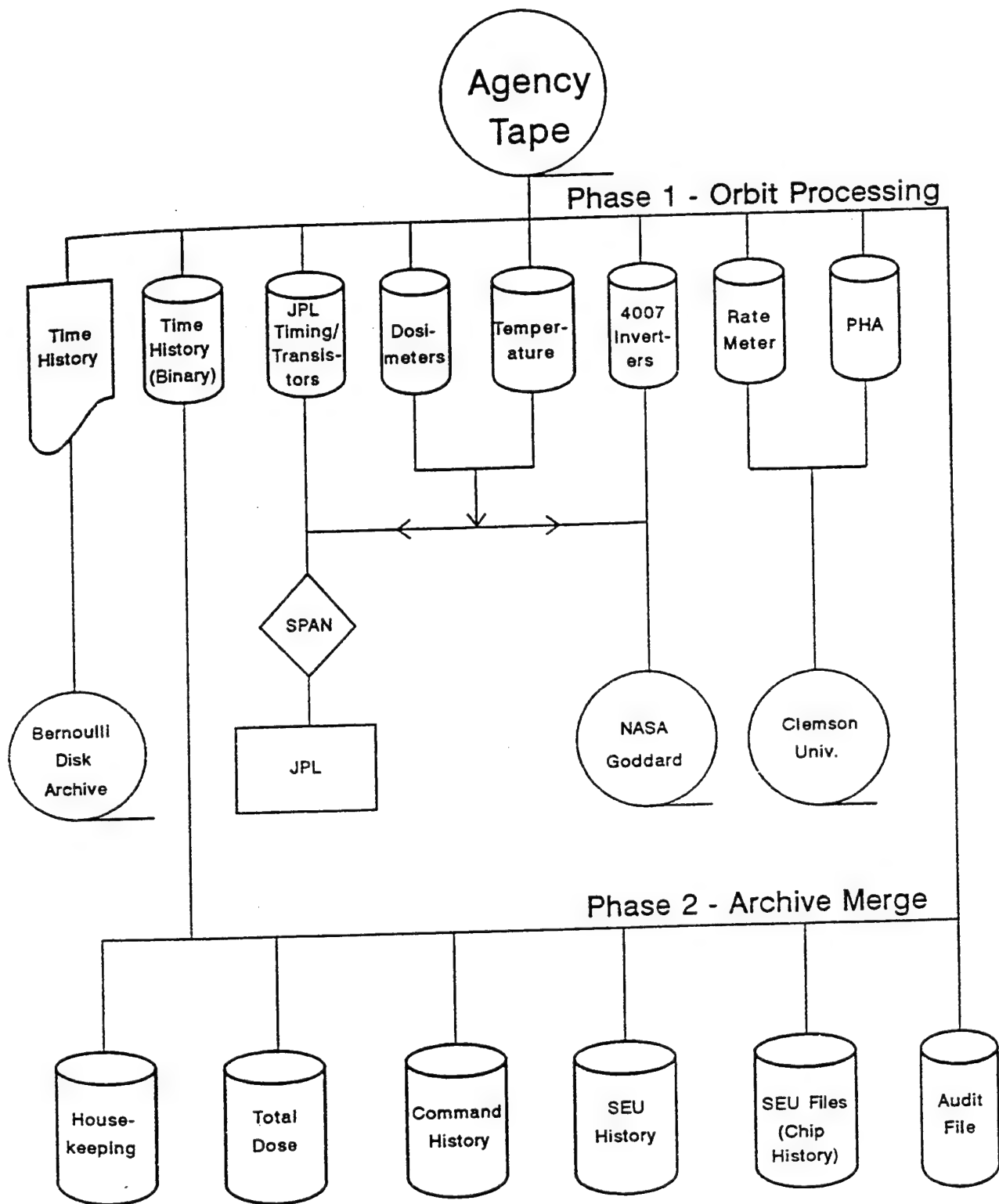


Figure 11. File production and delivery system.

### 3.2.2 Data Retrieval and Presentation

The program LOOKUP is used to unpack the binary archive files created by READSEQ. Individual packets or an entire category of data (for example, all Housekeeping data) may be extracted over any time or orbit range. Data may be presented in tables or in files suitable for plotting. Table 12 is a sample DUT Power table for orbit 700:

The asterisks indicate that a particular entry was not present in the telemetry. The time range for the power readings is shown at the top of the table (in general, specific event times are critical only for SEU's). The corresponding plot data file for DUT Power would have four columns: orbit number, ICU (0 or 1), block, and power reading.

A plotting program based on *GraphiC* (a product of Scientific Endeavors Corporation) has been written in C for use on PC's. This program allows selection of a particular ICU and device over a desired range of orbits. A typical plot of Dosimeter data is shown in Figure 12. In this case, the reading for orbit 4 is used as a "baseline", and is subtracted from subsequent readings to give accumulated dose.

LOOKUP can create spreadsheet-compatible files for selected packets, such as temperature and total dose; these files have been processed on PC's with Borland's QUATTRO. Special processing is required to print lines containing blank data fields where data is missing for an orbit. Certain capsulated event histories may also be generated - for example, Table 13 is a portion of an abbreviated command history (command parameters are not listed). Universal time in seconds is given in the right column.

Single Event Upsets and Rate Meter Upsets are more meaningful when studied in conjunction with various ephemeris parameters such as  $B/B_0$ , L-shell, and altitude, in order to determine the conditions under which upsets are most likely to occur. The programs SEUEPH and RMTEPH read the CRRES ephemeris files and generate listings of the upsets along with the corresponding ephemeris parameters. Table 14 is a sample of output from SEUEPH:

These listings have proven to be extremely useful in eliminating SEU's that are a result of ground commands and telemetry errors. SEU's of this type have been removed from the SEU database in order to maintain the validity of the statistics. The RMTEPH output has the same general format, and does not include Rate Meter packets where both counters are zero.

Similar files containing some different ephemeris parameters are also created for plotting purposes. Scatter plots have been generated from this data showing  $B/B_0$  versus L-shell at the time of SEU occurrence. Typically, these plots are produced for individual chips, though scatter plots for an entire ICU and the entire device have also been generated. The sample shown in Figure 13 shows a fairly typical concentration of SEU's at low values of L and  $B/B_0$ . At higher L values, we see three "tracks", a result of extremely high solar flare activity during three orbits.

**TABLE 12.** Sample DUT Power Table, Orbit 700

DUT Block Power Measurement, ICU B UT: 7346.369 - 8390.842

DUT Block Power Measurement, ICU B UT: 7346.369 - 8390.842

[illegible]

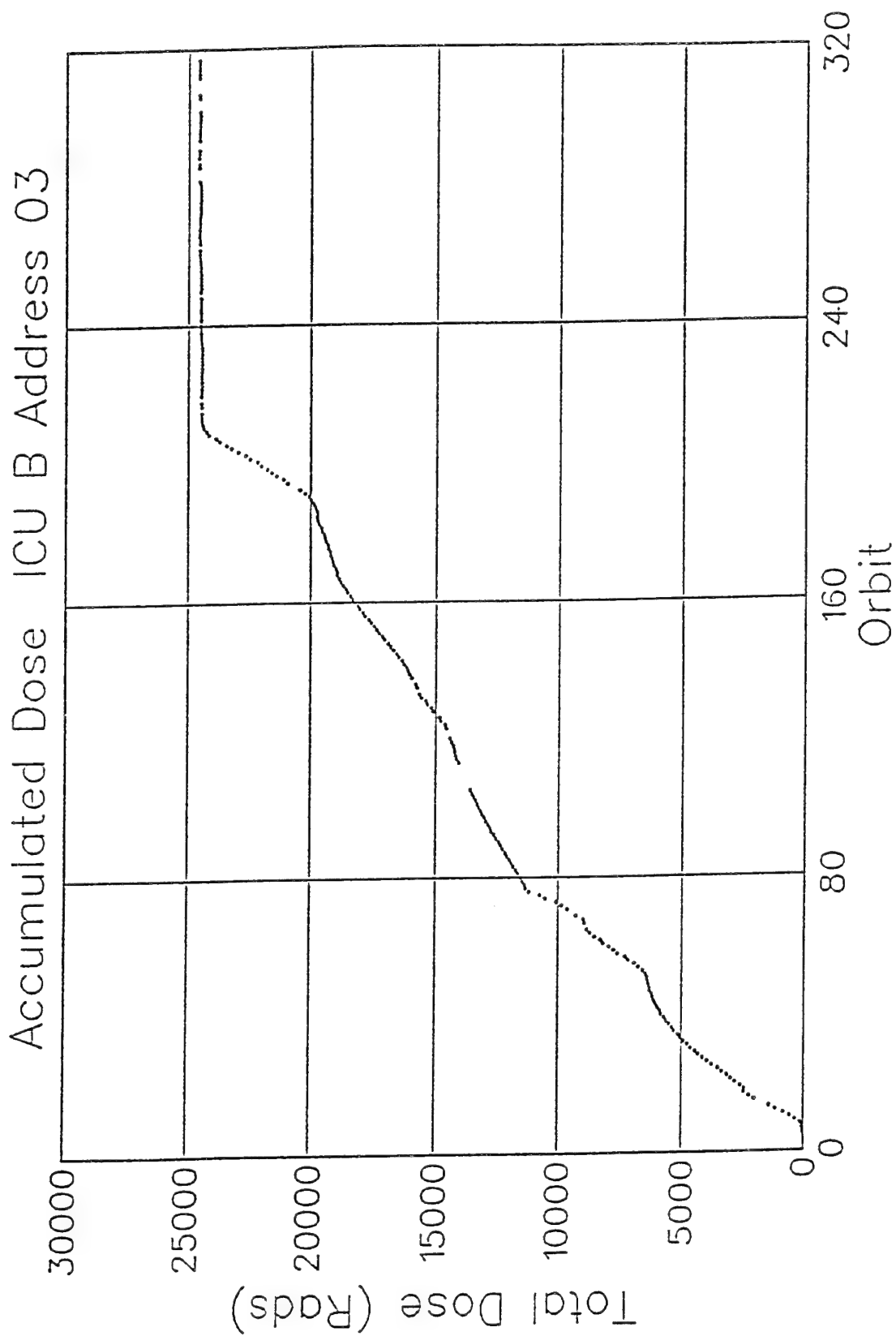


Figure 12. Accumulated dose vs. total dose.

**TABLE 13. Portion of an Abbreviated Command History**

Orbit 3 Day 208 Year 90	
ICU A Block Power Array	21417.400
ICU B Block Power Array	21417.400
Physical To Logical RAM Bank Mapping	24894.883
RAM Shadow Assignment	24894.883
Device "Map Around" Update	24894.883
ICU A Block Power Array	28626.443
ICU B Block Power Array	28626.443
ICU A Block Power Array	35835.230
ICU B Block Power Array	35835.230
Orbit 4 Day 208 Year 90	
Physical To Logical RAM Bank Mapping	42894.611
RAM Shadow Assignment	42894.611
Device "Map Around" Update	42894.611
ICU A Block Power Array	43044.242
ICU B Block Power Array	43044.242
Command Accepted - Command (624E) Orbit Segment	44180.748
Fatal Experiment Power Fault	45958.402
Fatal Experiment Power Fault	46786.814
Fatal Experiment Power Fault	47081.724
Fatal Experiment Power Fault	47409.402
Fatal Experiment Power Fault	49205.489
ICU A Block Power Array	50253.035
ICU B Block Power Array	50253.035
Fatal Experiment Power Fault	50722.024
Fatal Experiment Power Fault	50861.288
Fatal Experiment Power Fault	51594.468
Fatal Experiment Power Fault	51812.579
Fatal Experiment Power Fault	51906.786
Fatal Experiment Power Fault	51982.690
ICU A Block Power Array	57461.956
ICU B Block Power Array	57461.956
Physical To Logical RAM Bank Mapping	60894.386
RAM Shadow Assignment	60894.386
Device "Map Around" Update	60894.386
ICU A Block Power Array	64670.877
ICU B Block Power Array	64670.877
ICU A Block Power Array	71879.798
ICU B Block Power Array	71879.798



TABLE 14. Sample Output from SEUEPH

SEU	ICU	BLOCK	PAT	ADR	MSK	YR	DAY	ORBIT	UT	L-SHELL	ALT
Soft	A	14	0	0209	02	90	208	5	110617.574	1.3421	2616.3566
Soft	A	14	0	0DC0	10	90	209	6	59768.674	1.4367	2430.0860
Soft	A	14	0	099C	10	90	209	7	72066.808	5.7682	29899.4435
Soft	A	14	0	0F5B	10	90	209	7	95112.807	1.5079	3044.7825
Soft	A	14	0	0889	10	90	210	8	10638.011	1.4813	2239.7298
Soft	A	14	0	09F8	04	90	210	8	10767.034	1.5827	2729.2076
Soft	A	15	0	0D9A	02	90	208	3	39181.641	1.7002	4359.8479
Soft	A	15	0	05D1	01	90	208	5	110681.062	1.3046	2374.9149
Soft	A	15	0	0CDB	04	90	210	8	10621.627	1.4687	2179.5262
Soft	A	15	0	01A4	04	90	210	9	79784.198	1.7050	2785.3600
Soft	A	16	0	0034	10	90	208	5	110617.574	1.3421	2616.3566
Soft	A	16	0	0035	10	90	208	5	110617.574	1.3421	2616.3566
Soft	A	16	0	002C	01	90	209	6	26505.148	1.6981	4115.0668
Soft	A	16	0	003C	02	90	209	7	95061.607	1.5404	3249.7413
Soft	A	19	0	0891	80	90	209	6	59705.186	1.4936	2672.9131
Soft	A	1B	0	00CE	02	90	208	3	23010.734	6.3705	33581.5760
Soft	A	1B	0	00CF	02	90	208	3	39314.760	1.5945	3808.2303
Soft	A	1B	0	00C8	40	90	208	3	39431.495	1.5023	3331.7258
Soft	A	1B	0	00C6	80	90	208	3	39449.927	1.4878	3257.3614
Soft	A	1B	0	0042	01	90	208	3	39619.910	1.3574	2587.4841
Soft	A	1B	0	00CC	20	90	208	4	41626.905	1.6169	3003.4881
Soft	A	1B	0	00FB	04	90	208	4	75570.275	1.3047	1082.0291
Soft	A	1B	0	00F6	40	90	208	5	110361.576	1.5067	3637.3913
Soft	A	1B	0	00CE	08	90	209	6	26034.109	1.3952	2242.7131
Soft	A	1B	0	00B0	01	90	209	6	26296.252	1.5591	3259.6792
Soft	A	1B	0	0086	20	90	209	6	59660.131	1.5360	2848.5385
Soft	A	1B	0	00A6	20	90	209	6	59660.131	1.5360	2848.5385
Soft	A	1B	0	0016	80	90	209	7	95157.863	1.4795	2866.5681
Soft	A	1B	0	0056	80	90	209	7	95157.863	1.4795	2866.5681
Soft	A	1B	0	001D	08	90	209	7	95458.917	1.2958	1753.1643
Soft	A	1B	0	0046	01	90	210	8	10363.580	1.2884	1312.8113
Soft	A	1B	0	0082	10	90	210	8	10441.404	1.3380	1555.5200
Soft	A	1B	0	004E	01	90	210	8	43524.617	2.0347	5905.5401
Soft	A	1B	0	0049	08	90	210	8	44519.940	1.2536	1897.2323
Soft	A	1C	0	00D4	40	90	208	3	38788.427	2.0099	6003.6122
Soft	A	1C	0	00CC	40	90	208	3	39466.311	1.4750	3191.4982
Soft	A	1C	0	0037	20	90	208	3	39581.126	1.3866	2737.3805
Soft	A	1C	0	000F	40	90	208	3	39777.605	1.2446	2002.4706
Soft	A	1C	0	0031	40	90	208	3	39804.229	1.2268	1908.3973
Soft	A	1C	0	0071	40	90	208	3	39804.229	1.2268	1908.3973
Soft	A	1C	0	0026	01	90	208	5	110453.735	1.4455	3262.9412
Soft	A	1C	0	002D	40	90	208	5	110668.774	1.3117	2421.1626
Soft	A	1C	0	0042	20	90	209	7	95350.373	1.3603	2135.5702
Soft	A	1C	0	00DB	80	90	209	7	95399.525	1.3307	1959.1852
Soft	A	1C	0	00FD	80	90	210	8	10306.236	1.2551	1146.7876
Soft	A	1C	0	0028	08	90	210	8	10459.836	1.3504	1615.6472
Soft	A	1C	0	003E	80	90	210	8	10773.178	1.5876	2753.1099
Soft	A	1C	0	00CC	10	90	210	8	10807.994	1.6151	2889.4218
Soft	A	1C	0	0056	08	90	210	8	10900.153	1.6878	3256.4670
Soft	A	1D	0	00CB	80	90	208	4	75496.547	1.3809	1291.4170
Soft	A	1D	0	01F7	04	90	208	5	110457.831	1.4428	3246.4475
Soft	A	1D	0	00B8	10	90	209	6	26062.781	1.4122	2349.2562
Soft	A	1D	0	0190	01	90	209	6	26159.037	1.4712	2716.4163
Soft	A	1D	0	00F2	02	90	209	6	59916.130	1.3191	1892.6634
Soft	A	23	0	110F	08	90	210	8	10603.195	1.4546	2112.4018

MEP SEU Distribution ICU B  
Block 03 / A1-4 (Rkwl 1Kx1)

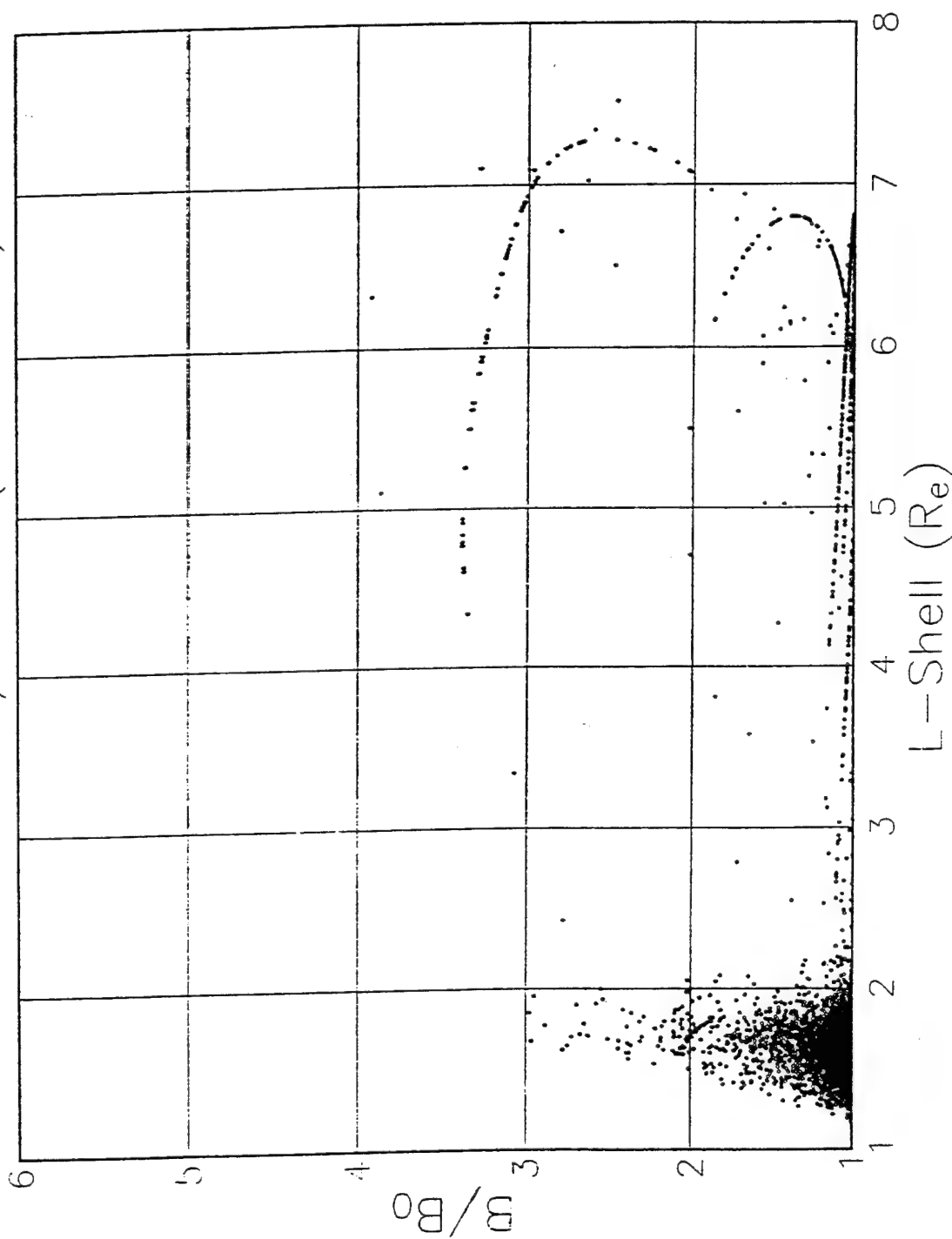


Figure 13. Scatter plot of MEP SEU distribution ICU B vs.  $B_0$ .

The satellite does not spend an equal amount of time at the various L-shell levels. Therefore, the scatter plots do not reflect the true frequency of occurrence of upsets in the various L bins. The amount of time that the satellite has spent at each L-shell level is determined from the ephemeris files. Periods of missing data are listed in the CRRES Agency Tape Anomaly bulletins released for each set of orbits; these intervals are not included in the statistics, since the receipt of upsets is not possible under such circumstances. The upsets are then binned by L-shell to produce a file of the type shown in Table 15:

TABLE 15. Table of Upsets							
Average L-shell	Combined Frequency	SEU Frequency	Rt Mtr Frequency	Total Upsets	SEU's	Rt Mtr Upsets	Time (Sec)
1.025	.94125E-04	.94125E-04	0.0000	12	12	0	127490
1.075	.56984E-04	.56984E-04	0.0000	9	9	0	157940
1.125	.60709E-03	.59680E-03	.10290E-04	118	116	2	194370
1.175	.71875E-03	.60817E-03	.11058E-03	130	110	20	180870
1.225	.27341E-02	.19422E-02	.79191E-03	473	336	137	173000
1.275	.73944E-02	.48205E-02	.25740E-02	1287	839	448	174050
1.325	.13244E-01	.83288E-02	.49156E-02	2204	1386	818	166410
1.375	.18249E-01	.11550E-01	.66987E-02	2776	1757	1019	152120
1.425	.22349E-01	.14419E-01	.79306E-02	3052	1969	1083	136560
1.475	.24353E-01	.16561E-01	.77916E-02	3113	2117	996	127830
1.525	.23165E-01	.16612E-01	.65528E-02	2821	2023	798	121780
			.				
			.				
			.				
8.275	.20896E-03	.14925E-03	.59701E-04	7	5	2	33500
8.325	.54001E-03	.54001E-03	0.0000	11	11	0	20370
8.375	.15936E-03	.15936E-03	0.0000	4	4	0	25100
8.425	0.0000	0.0000	0.0000	0	0	0	21140
8.475	0.0000	0.0000	0.0000	0	0	0	18520
8.525	.50302E-04	.50302E-04	0.0000	1	1	0	19880
8.575	.71582E-04	.71582E-04	0.0000	1	1	0	13970
8.625	0.0000	0.0000	0.0000	0	0	0	11790
8.675	0.0000	0.0000	0.0000	0	0	0	5830
8.725	0.0000	0.0000	0.0000	0	0	0	6010
8.775	0.0000	0.0000	0.0000	0	0	0	3160

L-Shell is in  $R_c$ , with the number given being the center of a bin (for example, 1.025 is the center of bin from 1.0 to 1.05); frequency is the number of upset events per second. Upsets have also been binned based on the satellite's position in  $R_c$ ; an SEU distribution plot of this type is shown in Figure 14. Similar studies have been made for individual blocks and for particular orbit ranges.

# SEU Distribution

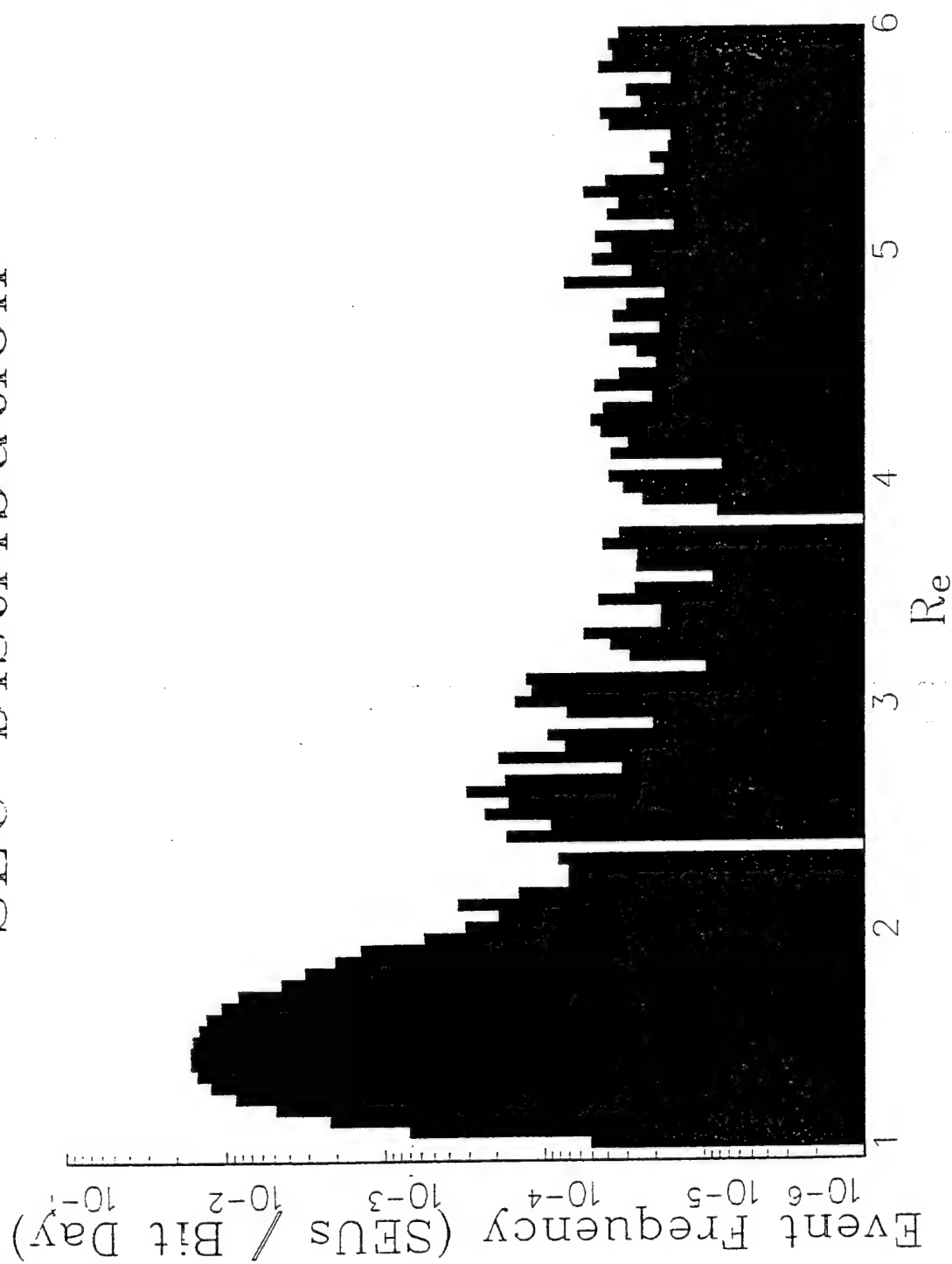


Figure 14. SEU distribution, ICU B.

### 3.2.3 Software Architecture and Development

The CRRES Microelectronics Package Serial Telemetry Manual [NRL, 1989] defines six categories of data packets:

- System Configuration
- System Data
- System Information
- Experiment Configuration
- Experiment Data
- Experiment Housekeeping / Error

The READMEP and READSEQ programs were designed around these six categories, which allows for functional association of related packets. For example, the fifteen System Data packets were broken down as follows:

- Memory Dump
- Task functions (Cancelled, Scheduled, Definition Update)
- ICU SEU testing (A Offline, A Online, B Offline, B Online)
- ICU Total Dose testing (A Offline, A Online, B Offline, B Online)
- ICU Swapping (Disabled; Enabled, ICU A Active; Enabled, ICU B Active)

This type of grouping resulted in much less code than would have been required if each individual packet was handled separately.

The objective of the initial software development was to simulate the output of the Real Time Data Acquisition System (RTDS) package, which was developed in C [Assurance Technology Corporation, 1989]. NOS/VE was chosen as the development environment, since this was the site of most related CRRES work. A number of discrepancies were discovered between the CRRES Microelectronics Package Serial Telemetry Manual [NRL, 1989] and the RTDS code. These were a combination of typographical errors in the manual and undocumented changes in the telemetry format; appropriate corrections were determined through communications with ATC.

Several GL 701-1A files were available for testing prior to the actual CRRES flight. These files were a product of ground "test chamber" operation of the MEP. READMEP was run using these files as input, and program output was verified against output from the RTDS. A number of modifications to READMEP were required during this phase, in order to handle the various time anomalies present in the sample files.

Upon completion, READMEP runs the READSEQ program, which maintains all permanent MEP databases on NOS/VE. Output data organization was determined in conjunction with PL personnel, and was designed to facilitate the data retrieval tasks performed by LOOKUP. Streams of a given packet type are collected and stored in one large data structure, the size of

which is known by LOOKUP. All disk I/O operations are performed using 9600 byte buffers, in order to minimize the amount of disk access. Since most retrieval requests are for one specific packet type, LOOKUP can advance quickly through the input buffer and skip data that is not of interest simply by incrementing a pointer.

Software for data presentation was developed primarily in the PC environment, using Microsoft C and *GraphiC 6.0*, a library of high-level graphics subroutines. This approach allowed for the production of high quality output with a minimal amount of effort. *GraphiC* can generate high resolution images on many different hardware devices, including full support of the HP Laserjet III printers used to produce the figures in this section [*Scientific Endeavors Corporation*, 1991]. Data transfer from NOS/VE to the PC can be accomplished quickly using the high speed Ethernet link available at PL.

### 3.3 MEP DATABASE

#### 3.3.1 File Storage

In order to minimize the volume of data stored on-line on the Cyber, the MEP data processing software was revised to maintain separate databases for every 1000 orbits. Older databases were to be backed up on tape and remain accessible through the Central File Storage System (CFS). Unfortunately, CRRES data transmission ceased shortly after completion of these code modifications (during orbit 1067).

Due to the plan to phase out the Cyber, the MEP databases were migrated to PC's and stored on Bernoulli disk (approximately 25 Mb of storage space is required). The LOOKUP program was adapted to run under MS-DOS (using the Microsoft FORTRAN compiler), and output was verified against NOS/VE results. There are several major differences between the two environments of significance to LOOKUP:

- Microsoft FORTRAN requires NOS/VE "UNFORMATTED" files to be opened as "BINARY" files (no modifications to the data files are necessary, unless floating point variables are used).
- The Microsoft FORTRAN default storage size for floating point variables is four bytes (compared to eight on NOS/VE).
- MS-DOS limits the number of open files to a maximum of 255 (compared to 1000 on NOS/VE).

A number of minor differences between the NOS/VE and Microsoft FORTRAN compilers also exist (for example, the method of appending files) [*Control Data Corporation*, 1988; *Microsoft Corporation*, 1991].

### 3.3.2 Permanent Database File Formats

The MEP permanent database files are standard FORTRAN unformatted files, consisting of a series of 3200 byte records. The first seven bytes of each record are reserved:

Bytes 1-4    Orbit number (low order byte first)  
Byte 5       Year (2 digit)  
Bytes 6-7    Day number (low order byte first)

The remainder of each record consists of a packetized stream, with a format similar to the telemetry; packets may cross record boundaries if necessary. The unused portion of the last record for an orbit is "1's filled". Table 16 summarizes the data packets stored in the four permanent MEP data files:

The "packet ID" numbers are the hexadecimal codes used to identify the type of each packet in the telemetry stream. Length is the packet size in bytes (-1 indicates variable length). The NRL group numbers refer to the six categories of data packets defined in the CRRES Microelectronics Package Serial Telemetry Manual [NRL, 1989] (refer to section 3.3). "LOOKUP file" indicates the file in which each packet may be found: 1 - Housekeeping, 2 - Total Dose, 3 - Command History, and 4 - SEU History. Packet names preceded by an asterisk are those for which the database format differs from the telemetry format.

TABLE 16. Archived Data Packets

Packet ID	Length	NRL Group	LOOKUP File	Name
32-33	13	1	3	EXPERIMENT BLOCK POWER ARRAY
34	6	1	3	RAM POWER
35	7	1	3	RELAY STROBED
36	8	1	3	RAM BANK MAPPING
38	8	1	3	RAM SHADOW ASSIGNMENT
40-41	6	1	3	REGISTER UPDATE
42-43	5	1	3	MMU INTERRUPT
46-47	7	1	3	COMMAND REJECTED / ACCEPTED
48,50,52,53	8	1	3	RESTART
64	-1	2	1	MEMORY DUMP
66-67	6	2	3	TASK CANCELLED / SCHEDULED
68	9	2	3	TASK DEFINITION UPDATE
72-75	5	2	4	ICU SEU OFFLINE / ONLINE
76-79	5	2	2	TOTAL DOSE OFFLINE / ONLINE
80-82	5	2	3	ICU SWAPPING
96,98,100	5	3	3	PROM CHECKSUM, NO ERROR
97,99,101	6	3	3	PROM CHECKSUM, ERROR BANK
102	7	3	3	COMMAND COULD NOT BE EXECUTED
103	6	3	3	WRITE PROTECT VIOLATION
104	5	3	3	RAM DIAGNOSTIC SUCCESS
105	9	3	3	RAM DIAGNOSTIC ERROR
106	5	3	3	WRITE PROTECT DIAGNOSTIC SUCCESS
107	7	3	3	WRITE PROTECT DIAGNOSTIC ERROR
108-111	5	3	3	WATCHDOG TIMER
112,113,116,118,119	9	3	3	PARITY ERROR
120-121	7	3	3	PARITY ERROR
124-127	9	3	3	PARITY ERROR
158	83	4	3	MAP AROUND UPDATE
159	7	4	3	MAP AROUND INITIATED
160-161	6	4	3	BLOCK POWER
162	5	4	3	EXPERIMENT ABORTED
164-165	6	4	4	SEU BLOCK DISABLED / ENABLED
166-167	6	4	2	TD BLOCK DISABLED / ENABLED
168-169	7	4	4	SEU DEVICE DECOMPRESSED / COMPRESSED
176	37	4	1	EXPERIMENT CONFIGURATION
177	-1	4	3	PERMANENT FAULT LIST UPDATE
184	7	4	3	*MEP MAXIMUM POWER UPDATE
186	5	4	3	PERMANENT FAULT LIST CLEARED
188	7	4	4	SEU TEST PATTERN UPDATE
195	6	5	4	PHA THRESHOLD UPDATE
196-197	777	5	4	*PHA SPECTRAL DATA
198-199	7	5	4	RATE METER DATA
200-203	9	5	2	ROCKWELL DATA
204-205	7	5	2	LOCKHEED DATA
206-207	49	5	2	*TOTAL DOSE REFERENCE
208-209	145	5	2	*TOTAL DOSE DOSIMETERS
210-211	41	5	2	*TOTAL DOSE HEXFETS
212-213	273	5	2	*TOTAL DOSE SEU VTR
214-215	777	5	2	*TOTAL DOSE OP-AMPS
216	65	5	2	*TOTAL DOSE CMOS OCTAL LATCH
217	89	5	2	*TOTAL DOSE ALS OCTAL LATCH
219	3281	5	2	*TOTAL DOSE 4007 INVERTERS
220	1037	5	2	*TOTAL DOSE ADC
221	97	5	2	*TOTAL DOSE ACCESS TIME
224-225	7	6	3	EXPERIMENT COMMAND UNKNOWN / REJECTED
226-227	29	6	1	*MEP PRIMARY CURRENT
228-229	8	6	3	EXPERIMENT POWER MONITOR FAULT
230-231	521	6	1	*DUT BLOCK POWER
232-233	57	6	1	*TEMPERATURE
234-235	6	6	3	INTERRUPT ERROR
236-239	153	6	1	*ANALOG TESTER CALIBRATION SYSDAC
240	7	6	4	SEU TIMEOUT
241-242	6	6	2	TOTAL DOSE TIMEOUT
243	7	6	4	RATE METER TIMEOUT
244	7	6	2	ROCKWELL TIMEOUT
245	7	6	2	LOCKHEED TIMEOUT
246	7	6	4	PHA TIMEOUT
247	6	6	3	ICU SWAP ERROR
251	5	6	3	FATAL EXPERIMENT POWER FAULT



All packets headers are followed by a time tag, which is stored to milliseconds accuracy, and requires four bytes. Otherwise, most of the packet storage formats are identical to that of the telemetry; refer to the CRRES Microelectronics Package Serial Telemetry Manual [NRL, 1989] for descriptions. Exceptions are marked in the table with an asterisk, and described below in section 3.3.3. Values stored in multi-byte integer or floating point format may be read with the functions INTREAD and READFLT:

```

INTEGER FUNCTION INTREAD (NBYTE)
COMMON /TAPEIN/ BINDAT, NBIN
CHARACTER*3200 BINDAT
IVAL = 0
DO 10 I=1,NBYTE
    IVAL = IVAL + ICHAR(BINDAT(NBIN+1:NBIN+1)) * 256**(I-1)
    NBIN = NBIN + 1
    IF (NBIN.GE.3200) CALL BINREAD
10 CONTINUE
INTREAD = IVAL
RETURN
END

FUNCTION READFLT (NDEC, NBYTE)
READFLT = INTREAD(NBYTE) / 10.**NDEC
RETURN
END

```

NBYTE indicates the number of bytes used to store the value, and NDEC indicates the number of places to the right of the decimal point for floating point values. NBIN is the location at which the BINDAT array should be read, and is incremented automatically by these routines. The call to BINREAD in INTREAD will read in the next 3200 byte record into BINDAT, if necessary.

### 3.3.3 Permanent Database Packet Formats

The first five bytes of all packets contain the header byte and the universal time of the data transmission. The descriptions in this section indicate the content of all subsequent bytes. Note that some packets contain additional universal time values. In this case, each successive pair of time values constitutes the time range for a series of measurements, such as shown in Table 12 in section 3.2.2.

The storage format for an individual variable is indicated in square brackets as follows:

[N] - integer requiring N bytes (call INTREAD (N))

[N, D] - floating point requiring N bytes, stored with D decimal places (call READFLT (D, N))

MEP Maximum Power Update: Power [3,2].

PHA Spectral Data: Time 2 [3,4], 32 packets x 8 channel counts [3]. Orbit segment and channel zero number are determined from the packet number (0-31), as in the telemetry.

Total Dose - Reference: ICU A - time 2 [3,4], 8 reference measurements [3,2]; ICU B - time 1 [3,4], time 2 [3,4], 8 reference measurements [3,2].

Total Dose - Dosimeters: ICU A - time 2 [3,4], 32 dosimeters [3,2]; ICU B - time 1 [3,4], time 2 [3,4], 32 dosimeters [3,2].

Total Dose - Hexfets: ICU A - time 2 [3,4], 6 hexfets [3,2]; ICU B - time 1 [3,4], time 2 [3,4], 6 hexfets [3,2].

Total Dose - SEU Vtr: ICU A - time 2 [3,4], 16 devices x 4 measurements [3,2]; ICU B - time 1 [3,4], time 2 [3,4], 16 devices x 4 measurements [3,2]. Measurements 1 through 3 are VTR data readings 0, 1, and 2; measurement 4 is the 1.2 volt reference measurement.

Total Dose - Op-Amps: ICU A - time 2 [3,4], 19 devices x 10 tests [3,2]; ICU B - time 1 [3,4], time 2 [3,4], 19 devices x 10 tests [3,2].

Total Dose - CMOS Octal Latch: ICU A - time 2 [3,4], 2 blocks x 6 measurements [3,2]; ICU B time 1 [3,4], time 2 [3,4], 2 blocks x 6 measurements [3,2]. Measurements 1-3 are VTR data readings; measurements 4-6 are IOZH data readings.

Total Dose - ALS Octal Latch: ICU A - time 2 [3,4], 2 blocks x 9 measurements [3,2]; ICU B - time 1 [3,4], time 2 [3,4], 2 blocks x 9 measurements [3,2]. Measurements 1-3 are IIH data readings; measurements 4-6 are Function +5V readings; measurements 7-9 are Function +0V readings.

Total Dose - 4007 Inverters: ICU A - time 2 [3,4], 6 blocks x 16 devices x {device address [1], 8 currents [3,2]}; ICU B - time 1 [3,4], time 2 [3,4], 6 blocks x 16 devices x {device address [1], 8 currents [3,2]}.

Total Dose - ADC: ICU A - time 2 [3,4], 17 codes x 6 devices x {block number [1], current [3,4]}; ICU B - time 1 [3,4], time 2 [3,4], 17 codes x 6 devices x {block number [1], current [3,4]}.

Total Dose - Access Time: ICU A - time 2 [3,4], 5 blocks x 2 devices x {reference measurement [3,2], access time [1,2]}; ICU B - time 1 [3,4], time 2 [3,4], 5 blocks x 2 devices x {reference measurement [3,2], access time [1,2]}.

MEP Primary Current: Time 2 [3,4], 2 ICU's x 5 currents [3,2].

DUT Block Power: Time 2 [3,4], 256 power readings [3,2]. ICU is determined by the header byte (230 for A, 231 for B).

Temperature: Time 2 [3,4], 24 temperature readings [2,2]. ICU is determined by the header byte (232 for A, 233 for B).

Analog Tester Calibration SYSDAC: Time 2 [3,4], 9 inputs x 2 SYSDAC's x 2 ICU's x {reading [3,2], convert time [1,2]}.

### 3.3.4 SEU Chip History File Format

The SEU chip history files are standard FORTRAN unformatted files, consisting of a series of 80 byte records. Each record contains data for one Single Event Upset, and may be read with the following statement:

```
READ(1) ICU, NUMBL, IYR, IDAY, IUT, IORB, ICODE, INT1, INT2, IPAT
```

The parameters are:

ICU	0 for ICU A, or 1 for ICU B
NUMBL	The block number
IYR	The last two digits of the year
IDAY	The day of the year
IUT	Universal time (floating point) milliseconds
IORB	The orbit number
ICODE	192 for Soft SEU, 193 for Hard SEU, or 194 for SEU Compressed Data
INT1	Address for a Soft or Hard SEU, or device for SEU Compressed Data
INT2	Mask for a Soft or Hard SEU, or error count for SEU Compressed Data
IPAT	The pattern stored in the DUT block

### 3.3.5 JPL File Formats

JPL Timing and JPL Transistor data files are standard FORTRAN unformatted files, consisting of a series of 10000 byte records. The last record in a file may not be completely filled with data; the vacant bytes are "1's filled". All integer variables requiring more than one byte are written low byte to high byte. Tables 17 and 18 summarize the two file structures.

### 3.3.6 4007 Inverter File Format

4007 Inverter data files are standard FORTRAN unformatted files, consisting of a series of 9200 byte records. The last record in a file may not be completely filled with data; the vacant bytes are "1's filled". All variables requiring more than one byte are written low byte to high byte. Table 19 summarizes the file structure.

**TABLE 17. JPL Timing File Format**

Bytes 1-2	Packet identifier, DA <sub>16</sub> (218 <sub>10</sub> )
Bytes 3-4	The number of 9-byte packets that follow in this record
Bytes 5-8	Universal time in milliseconds
Byte 9	ICU and Block Number Bit 7 (highest order bit) gives the ICU (0 for ICU A, 1 for ICU B) Bits 0-5 give the Block Number
Byte 10	Device 0, rising edge
Byte 11	Device 0, falling edge
Byte 12	Device 1, rising edge
Byte 13	Device 1, falling edge
Bytes 14-22	Repeat order of bytes 5-13
Bytes 9986-9994	Repeat order of bytes 5-13
Bytes 9995-10000	Vacant (1's filled)

**TABLE 18. JPL Transistor File Format**

Bytes 1-2	Packet identifier, DE <sub>16</sub> (222 <sub>10</sub> )
Bytes 3-4	The number of 68-byte packets that follow in this record
Bytes 5-8	Universal time in milliseconds
Byte 9	ICU and Block Number Bit 7 (highest order bit) gives the ICU (0 for ICU A, 1 for ICU B). Bits 0-5 give the Block Number.
Byte 10	Device Number and Transistor Number Bits 5-7 give the device number; bits 0-4 give the transistor number.
Bytes 11-12	Vdd measurement results (mV)
Bytes 13-14	Vg 0 measurement results (mV)
Bytes 15-16	Vd 0 measurement results (mV)
Bytes 17-18	Id 0 measurement results (see below)
Bytes 67-68	Vg 9 measurement results (mV)
Bytes 69-70	Vd 9 measurement results (mV)
Bytes 71-72	Id 9 measurement results (see below)
Bytes 73-140	Repeat order of bytes 5-72
Bytes 9933-10000	Repeat order of bytes 5-72
To obtain the Id measurement value in mA: I.     Itemp = Idval (2 byte integer read above) II.    If <High Byte> > 127 Then Itemp = Itemp .AND. '3FFF'X (discard the 2 highest order bits) Id = Itemp * .0002 Else Id = Itemp * .000002	

**TABLE 19. 4007 Inverter File Format**

Bytes 1-2	Packet identifier, DB <sub>16</sub> (219 <sub>10</sub> )
Bytes 3-4	The number of 22-byte packets that follow in this record
Bytes 5-8	Universal time in milliseconds
Byte 9	ICU and Block Number Bit 7 (highest order bit) gives the ICU (0 for ICU A, 1 for ICU B). Bits 0-5 give the Block Number.
Byte 10	Device Address
Bytes 11-12	Current 0 (10 mA)
Bytes 13-14	Current 1 (3 mA)
Bytes 15-16	Current 2 (1 mA)
Bytes 17-18	Current 3 (300 uA)
Bytes 19-20	Current 4 (100 uA)
Bytes 21-22	Current 5 (30 uA)
Bytes 23-24	Current 6 (10 uA)
Bytes 25-26	Current 7 (1 uA)
Bytes 27-48	Repeat order of bytes 5-26
Bytes 9179-9200	Repeat order of bytes 5-26
Divide all current values by 1000 to obtain the actual measurement values.	

## 4. MARCH 1991 MAGNETIC STORM MODELING

### 4.1 INTRODUCTION

The appearance of a second proton radiation belt has been observed in some major magnetic storms [McIlwain, 1963; Gussenhoven, *et al.*, 1989]. It is not known whether the second belt is formed by introduction of new particles into the magnetosphere, or by a redistribution of existing magnetospheric populations. New particles could be introduced, for example, by some enhancement or variant of the classical neutron albedo [Lingenfelter, 1963] which is generally considered to be responsible for formation and maintenance of the inner proton belt. Possible mechanisms involving existing magnetospheric populations include splitting the belt (outward transport of some of the particles in the outer portion of the preexisting belt), inward transport of penetrating solar particles, or acceleration in place of existing trapped particles.

The CRRES satellite, launched 25 July 1990, provided a unique opportunity to study the dynamics of the radiation belts. The CRRES orbit ranges from  $L \sim 1.05$  to  $\sim 6.6$ , at an orbital inclination of  $18^\circ$ . Its particle instrumentation measures 10 eV - 10 GeV particles with excellent energy and pitch angle resolution. The magnetometer measures the magnetic field in the range  $\pm 45000$  NT. For a detailed description of the CRRES instruments, see Gussenhoven, *et al.* [1985].

At the Sudden Storm Commencement (SSC) of 03:43 UT 24 March, 1991, CRRES observed spikes in the proton populations above 20 MeV, at  $L=2.55$  [Mullen and Gussenhoven, 1991]. In subsequent passes, a second proton belt was seen in these populations in this  $L$  region, which persisted at least until 11 October 1991, when contact with the satellite was lost. For  $\sim 24$  hours prior to the SSC, substantial solar proton populations were seen, associated with the solar flare recorded at 22:42 UT 22 March. These protons penetrated to  $L \sim 4$ . At SSC, the Cerenkov counter, designed originally to detect protons, saw substantial increases in the 25 MeV electron population [Blake, 1991].

In this report, we model the acceleration and transport of magnetospheric particles in a rapidly changing magnetic field, in an attempt to determine if these processes, as opposed to the introduction of new particles into the magnetosphere, could account for the formation of the new proton belt and the 25 MeV electron population. For the protons, we numerically integrated the relativistic equations of motion in the presence of a time-varying magnetic field (and its induced electric field), optionally supplemented with an additional non-induced electric field.

In addition to examining the effects of simple time-dependent magnetic field models (mirror dipole field, with time-varying standoff distance, mirror dipole field, fixed standoff distance, and time dependent strength of the mirror dipole), we also examined the effects of a modified Mead field, and Karl Pfister's dynamic magnetospheric field model.

Variations on the Mead model [Mead, 1964] were used in which a pair of quiet Tsyganenko-type ring current fields [Tsyganenko and Usmanov, 1982; Hilmer, 1989] were added to test the effect

of the addition of ring currents. A similar study was performed using Karl Pfizter's dynamical magnetospheric magnetic field [Pfizter, 1992].

For each field, multiple proton trajectories were computed for a variety of initial conditions (both forward in time and backward in time). None of the computed trajectories for these models brought in protons initially beyond  $L = 4$  to the  $L = 2.5$  region observed by CRRES, or accelerated lower energy particles already there to energies above 20 MeV corresponding to protons found in the new belt.

As a result of the simulations, we conclude that, although a rapidly compressing magnetosphere can significantly accelerate and transport particles that are initially beyond  $L = 4$ , reasonable models of the changing magnetic field and the corresponding induced electric field, are not sufficient to bring the particles in to the  $L = 2.5$  observed by CRRES, or to accelerate lower energy particles already there to energies above 20 MeV for which the new belt was observed. We find that either an additional non-inductive transient electric field of 1 V/m is necessary to produce the new belt, or that there may be a possible resonance effect in which only particles with a narrow range of initial conditions were accelerated to form the new belt.

A study of the energy changes resulting from the compression of the model fields and predictions obtained assuming adiabatic behavior of the charged particles has also been made. The results of this study are also provided in this report, together with a series of tables describing the results.

## 4.2 METHODOLOGY

An important approach for the study of the motion of charged particles (protons or electrons) in the magnetosphere is to compute individual particle trajectories in external time-dependent electric and magnetic fields. The presence of multiple charged particles and their subsequent collective motion, will, even in the case of a neutral plasma, result in the modification of these fields. It will be necessary to include these effects in the field models in order to accurately model the fields during the magnetic storm.

For the trajectory computations reported here, a fast automatic step size Runge-Kutta-Fehlberg (RKF) integration routine was used to integrate the appropriate relativistic equations of motion. The source code was written in FORTRAN 77, and implemented using the Microsoft Fortran 5.1 compiler on an Intel 80486 based personal computer. For protons in the outer magnetosphere and in the outer radiation belts, these calculations are reasonably fast. However, for protons in the inner belt, and for protons mirroring at high latitudes, the computation time required becomes excessive. Thus, for some calculations, the FORTRAN code has been ported to other computer systems. For electrons, the time required to integrate the relativistic equations of motion is prohibitive - about 1,800 times longer than that required for protons - because, for a given required accuracy, the required integration step size is inversely proportional to the instantaneous radius of curvature of the orbit.

The motion of a charged particle in a combined external electric and magnetic field is generally complex, but there are circumstances under which the motion exhibits periodic or near periodic behavior. The simplest example is that of a proton or an electron in a uniform magnetic field, with no electric field. Depending on the pitch angle (the angle between the particle's velocity vector and the magnetic field vector) the particle moves in a circular spiral motion (for a pitch angle of 90 degrees, circular motion). The addition of a uniform electric field introduces additional effects, a drift velocity for the component perpendicular to the magnetic field, and an acceleration along the magnetic field for the parallel component, in addition to the spiral motion.

The relativistic guiding center equations of motion are a set of differential equations which approximate the "orbit" or "motion" of the guiding center, a fictitious point which lies approximately at the center of the proton's "spiral motion" about the magnetic field line. Thus, for the computation of electron (and where necessary, for proton) trajectories, it was desirable to develop similar software to integrate the relativistic guiding center equations of motion. The same RKF integration routine was used.

For numerical integration of equations of motion using RKF and similar schemes, the primary error of concern is truncation error. In the RKF scheme, an estimate of the truncation error is made at each integration step, and the step size is adjusted to keep the estimated truncation error within user set bounds. The standard way of testing the step size control is to verify that conservation laws are not violated. In this case, using static magnetic fields and a null electric field, the step size control parameters were chosen so that energy was constant to within a few electron volts for the worst cases.

#### 4.2.1 Relativistic Equations of Motion

The relativistic equations of motion for a charged particle in an external electric and magnetic field may be derived by differentiating the relativistic momentum equation  $\mathbf{p} = m \mathbf{v} \gamma$  with respect to time, and solving for  $d\mathbf{v}/dt$  in terms of the force  $d\mathbf{p}/dt$ . The relativistic equations of motion are given by Eq. 4-1. To integrate these equations of motion, it is necessary to compute the electric field  $\mathbf{E}$  and the magnetic field  $\mathbf{B}$  as a function of position and time.

$$\frac{d\mathbf{v}}{dt} = \frac{1}{m\gamma} \left( \frac{d\mathbf{p}}{dt} - \left( \frac{d\mathbf{p}}{dt} \cdot \frac{\mathbf{v}}{c} \right) \frac{\mathbf{v}}{c} \right)$$

where

(4-1)

$$\frac{d\mathbf{p}}{dt} = q (\mathbf{E} + \mathbf{v} \times \mathbf{B}), \quad \gamma = \left( 1 - \frac{v^2}{c^2} \right)^{-\frac{1}{2}}$$



#### 4.2.2 Relativistic Guiding Center Equations of Motion

The relativistic guiding center equations of motion were adapted from *Northrop* [1963]. In order to state the equations of motion, it is first necessary to define the following quantities:

$$\begin{aligned} \mathbf{v}_{drift} &= \frac{\mathbf{E} \times \mathbf{B}}{B^2}, \quad \mathbf{u}_B = \frac{\mathbf{B}}{B}, \quad \gamma_{drift} = \left[ 1 - \frac{v_{drift}^2}{c^2} \right]^{-\frac{1}{2}} \\ M_r &= \frac{p_{\perp}^{*2} \gamma_{drift}}{2mB} = \text{constant}, \quad E_{\parallel} = \mathbf{E} \cdot \mathbf{u}_B, \quad v_{\parallel} = \mathbf{v} \cdot \mathbf{u}_B, \end{aligned} \quad (4-2)$$

where  $p_{\perp}^*$  is the momentum component orthogonal to  $\mathbf{B}$  as viewed in the  $\mathbf{v}_{drift}$  reference frame.

The relativistic guiding center equations of motion are given by Eq. (4-3).

$$\begin{aligned} \frac{d\mathbf{R}_{gc}}{dt} &= \frac{d\mathbf{R}_{\perp}}{dt} + v_{\parallel} \mathbf{u}_B \\ \frac{d\mathbf{R}_{\perp}}{dt} &= \frac{\mathbf{u}_B}{B} \times \left[ -\mathbf{E} + \frac{M_r \gamma_{drift}^2}{\gamma q} \nabla \left( \frac{B}{\gamma_{drift}} \right) + \frac{m\gamma}{q} \gamma_{drift}^2 \left( v_{\parallel} \frac{d\mathbf{u}_B}{dt} + \frac{d\mathbf{v}_{drift}}{dt} \right) \right. \\ &\quad \left. + \frac{v_{\parallel} E_{\parallel} v_{drift}^2 \gamma_{drift}^2}{c^2} + \frac{M_r v_{drift}^2 \gamma_{drift}^2}{\gamma q c^2} \frac{\partial}{\partial t} \left( \frac{B}{\gamma_{drift}} \right) \right] \\ \frac{d\gamma}{dt} &= \frac{q}{mc^2} \left[ \frac{d\mathbf{R}_{\perp}}{dt} + v_{\parallel} \mathbf{u}_B \right] \cdot \mathbf{E} + \frac{M_r}{mc^2 \gamma} \frac{\partial}{\partial t} \left( \frac{B}{\gamma_{drift}} \right) \\ \frac{dp_{\parallel}}{dt} &= m \frac{d(\gamma v_{\parallel})}{dt} = m \gamma v_{drift} \cdot \frac{d\mathbf{u}_B}{dt} + q E_{\parallel} - \frac{M_r}{\gamma} (\mathbf{u}_B \cdot \nabla) \left( \frac{B}{\gamma_{drift}} \right) \end{aligned} \quad (4-3)$$

where

$$\begin{aligned} \frac{d\mathbf{u}_B}{dt} &= \frac{\partial \mathbf{u}_B}{\partial t} + v_{\parallel} (\mathbf{u}_B \cdot \nabla) \mathbf{u}_B + (v_{drift} \cdot \nabla) \mathbf{u}_B \\ \frac{d\mathbf{v}_{drift}}{dt} &= \frac{\partial \mathbf{v}_{drift}}{\partial t} + v_{\parallel} (\mathbf{u}_B \cdot \nabla) \mathbf{v}_{drift} + (v_{drift} \cdot \nabla) \mathbf{v}_{drift} \end{aligned}$$

The requirements for the validity of the guiding center equations is that the drift velocity ( $v_{\text{drift}}$ ) is small compared to the speed of light, and that the first adiabatic invariant ( $M_r$ ) is conserved.

For the guiding center equations of motion, in addition to computing the  $\mathbf{E}$  and  $\mathbf{B}$  fields, it is also necessary to compute their partial derivatives with respect to spatial coordinates and the time. Despite the added complexity, the computation time for proton trajectories is comparable to that required for direct integration; for electron trajectories the computation time is comparable to that of protons.

To verify the performance of the guiding center trajectory computations, parallel computations of the actual and guiding center equations of motion were made. To facilitate the evaluation of the trajectory data, graphics files of the trajectories (projection of the motion on the XY, XZ, and YZ planes) were produced, in addition to the output listing of the trajectory. Figures 15-17 are the graphs for a single proton trajectory, and its corresponding guiding center trajectory.

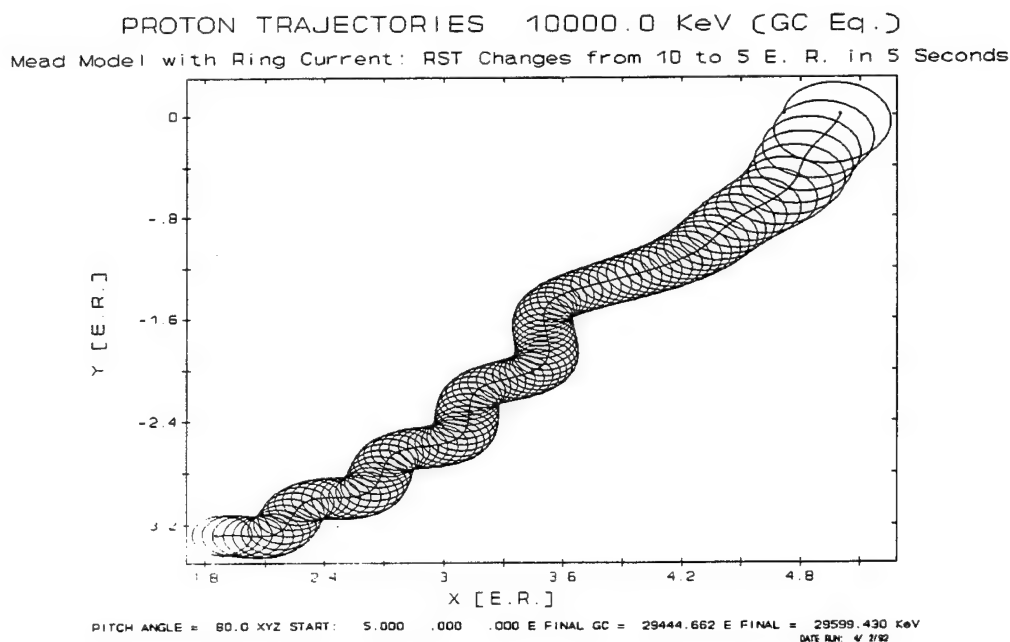


**Figure 15.** Comparison between guiding center trajectory and computed trajectory.

PROTON TRAJECTORIES 10000.0 KeV (GC Eq.)  
Mead Model with Ring Current: RST Changes from 10 to 5 E. R. in 5 Seconds

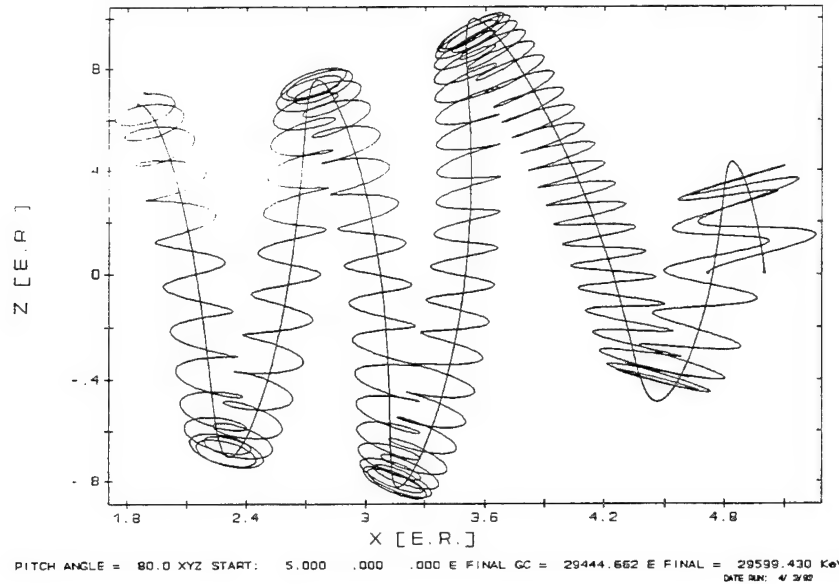


**Figure 16.** Comparison between guiding center trajectory and computed trajectory.

PROTON TRAJECTORIES 10000.0 KeV (GC Eq.)  
Mead Model with Ring Current: RST Changes from 10 to 5 E. R. in 5 Seconds

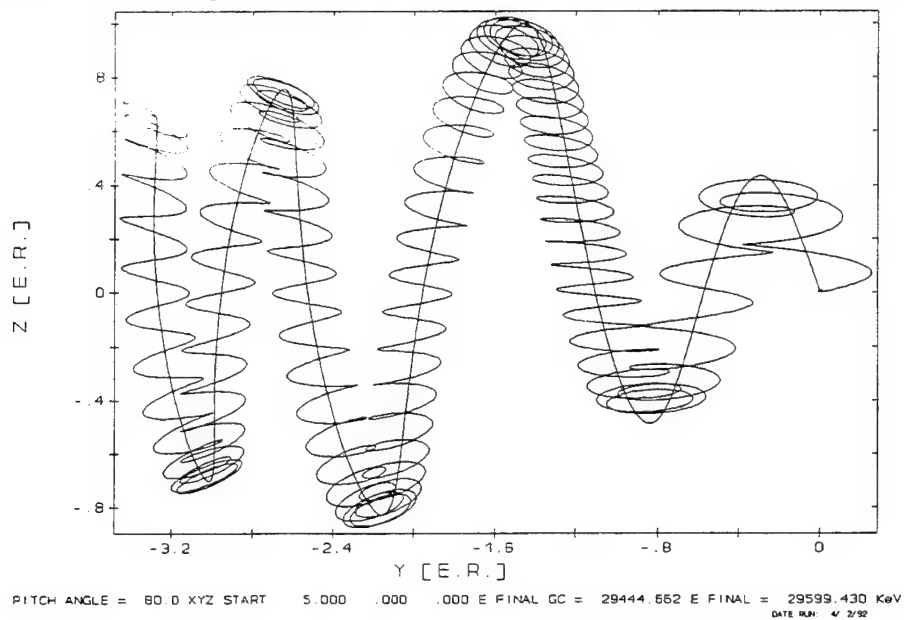


**Figure 17.** Comparison between guiding center trajectory and computed trajectory.

### 4.2.3 Magnetic Field Models:

A number of simple time-varying magnetic field models (and their induced electric fields) were used to examine the behavior of the protons. First, a dipole field with an "image" dipole at the stand-off distance was used, with the stand-off distance decreasing linearly from 10 to 5 Earth radii in 60, 30, and 5 seconds. Second, a dipole field with a fixed "image" dipole of variable strength, which increased in strength linearly from 1 to 10 times that of Earth over the same time intervals was used. The before/after field strengths were computed at the CRRES location, and were compared with the observed magnetic field observed at CRRES, with the result that these two field models could not reproduce the changes in the observed field strengths.

#### (i) Modified Mead Model

The Mead model was then used, with reasonable results, for the field strength changes for a 5 second decrease of the stand off distance from 10 to 5 Earth radii. The standoff distance  $b$  was assumed to have the following time dependence:

$$\begin{aligned} b(t) &= 10 - 2t(1 - t/10) && \text{for } 0 \leq t \leq 5 \text{ seconds} \\ &= 5 && \text{for } t > 5 \text{ seconds} \end{aligned}$$

Hilmer-Voigt [Hilmer, 1989] ring current terms, corresponding to a quiet magnetosphere, were added, and a series of trajectories was computed.

A combination of the Mead magnetic field model, the Hilmer-Voigt ring current model, and a higher order induced electric field (derived from the Mead magnetic field [Schulz and Lanzerotti, 1974] by requiring that  $\mathbf{E} \cdot \mathbf{B} = 0$ ) was used to compute proton trajectories. The results indicate that higher energies and lower midnight local time radii are obtained, but the addition of these terms to the model were insufficient to bring in the protons to an L value of 2.5 Earth radii.

#### (ii) Karl Pfizter's Dynamical Magnetic Field Model

Karl Pfizter's Dynamical Magnetosphere Model [Pfizter, 1992] is described by a vector potential which is parameterized by an instantaneous standoff distance  $b$  relative to a standard reference value  $b_0 = 10.5$  Earth radii. The dynamics is modeled by the time dependence of the standoff distance. In this model, the scalar potential is assumed to be constant.

The Karl Pfizter vector potential is given by

$$A(r) = \left[ \frac{b_0}{b} \right]^2 \sum_{i=0}^5 \sum_{j=0}^5 \sum_{k=0}^5 x_s^i y_s^j z_s^k A_{ijk} \quad (4-4)$$

where  $b_0 = 10.5$  Earth radii;  
 $(x_s, y_s, z_s)$  are scaled coordinates:

$$(x_s, y_s, z_s) = \left[ \frac{b_0}{b} \right] r$$

The functional form of the standoff distance is determined from a (magneto)hydrodynamic flow model for the solar wind. The vector expansion coefficients  $A_{ijk}$  are constant vectors, and are tilt dependent.

The Karl Pfizter trajectory code computes the magnetic field  $\mathbf{B}$  and the induced electric field  $\mathbf{E}$  from the vector potential by numerical differentiation.

In order to apply the Karl Pfizter magnetosphere model to compute trajectories using a relativistic implementation of the guiding center equations [Northrop, 1963], it is desirable not to rely on numerical differentiation. Here, it is not only necessary to compute the model's  $\mathbf{B}$  and  $\mathbf{E}$  fields, but also their partial derivatives with respect to the spatial coordinates and time. The accuracy of numerical differentiation for this purpose is questionable, and is likely to contribute to loss of accuracy over the trajectory integration. Instead, it was decided to convert the Karl Pfizter model into a spherical harmonic representation. The computations of the fields (and their derivatives for the guiding center computations) are then precise (subject to round off and truncation errors).

The conversion was accomplished by expressing  $x_s^i y_s^j z_s^k$  as the product of  $r_s^{i+j+k}$  and a sum of spherical harmonics by computing the integrals:

$$c_{l,m}(i,j,k) = \int_0^\pi \int_0^{2\pi} \cos^k \theta \sin^{i+j+1} \theta \cos^i \phi \sin^j \phi Y_{l,m}^*(\theta, \phi) d\theta d\phi \quad (4-5)$$

$i, j, k = 0, 1, \dots, 5$

using Mathematica [Wolfram, 1991], and computing the vector coefficients  $A_{l,m}$  of a spherical harmonic expansion as follows:

$$A_{l,m}(r_s) = \sum_{i,j,k} c_{l,m}(i,j,k) r_s^{i+j+k} A_{ijk} \quad (4-6)$$

In this manner, we obtain a spherical harmonic representation of the Karl Pfitzer vector potential:

$$A(r) = \left[ \frac{b_0}{b} \right]^2 \sum_{l=0}^5 \sum_{m=-l}^l A_{l,m}(r_s) Y_{l,m}(\theta, \phi) \quad (4-7)$$

where  $r_s = \left[ \frac{b_0}{b} \right] r$

The induced electric field  $E$  is given by:

$$E(r) = -\frac{\partial A(r)}{\partial t} = \frac{1}{b} \frac{db}{dt} \left[ \frac{b_0}{b} \right]^2 \sum_{l,m} (2 A_{l,m}(r_s) + r_s A'_{l,m}(r_s)) Y_{l,m}(\theta, \phi) \quad (4-8)$$

where  $A'_{l,m}(r_s) = \frac{dA_{l,m}(r_s)}{dr_s}$

and magnetic induction vector  $B$  is given by:

$$B(r) = \nabla \times A(r) = \left[ \frac{b_0}{b} \right]^2 \sum_{l,m} (\nabla Y_{l,m}(\theta, \phi) \times A_{l,m}(r_s) + Y_{l,m}(\theta, \phi) \left[ \frac{b_0}{b} \right] \frac{r_s}{r_s} \times A'_{l,m}(r_s)) \quad (4-9)$$

Note: For the gradient operator, the differentiation is performed with respect to the unscaled coordinates. From the identity

$$\frac{\partial}{\partial x_k} = \sum_{l=1}^3 \frac{\partial x_{sl}}{\partial x_k} \frac{\partial}{\partial x_{sl}}, \quad x_{sl} = \left[ \frac{b_0}{b} \right] x_l \text{ and } \frac{\partial x_{sl}}{\partial x_k} = \left[ \frac{b_0}{b} \right] \delta_{lk} \quad (4-10)$$

$$\text{it follows that } \nabla = \left[ \frac{b_0}{b} \right] \nabla_s$$

It then follows that  $\mathbf{B}$  may be expressed as:

$$\mathbf{B}(\mathbf{r}) = \nabla \times \mathbf{A}(\mathbf{r}) = \left[ \frac{b_0}{b} \right]^3 \sum_{l,m} (\nabla_s Y_{l,m}(\theta, \phi) \times \mathbf{A}_{l,m}(r_s) + Y_{l,m}(\theta, \phi) \frac{\mathbf{r}_s}{r_s} \times \mathbf{A}'_{l,m}(r_s)) \quad (4-11)$$

The partial derivative of  $\mathbf{E}$  with respect to the unscaled coordinate  $x_k$  (expressed in terms of scaled coordinates) is given by:

$$\frac{\partial \mathbf{E}(\mathbf{r})}{\partial x_k} = \frac{1}{b} \frac{db}{dt} \left[ \frac{b_0}{b} \right]^3 \sum_{l,m} [(2\mathbf{A}_{l,m}(r_s) + r_s \mathbf{A}'_{l,m}(r_s)) \frac{\partial Y_{l,m}(\theta, \phi)}{\partial x_{sk}} + \frac{x_k}{r} (3\mathbf{A}'_{l,m}(r_s) + r_s \mathbf{A}''_{l,m}(r_s)) Y_{l,m}(\theta, \phi)] \quad (4-12)$$

The partial derivative of  $\mathbf{E}$  with respect to  $t$  is given by:

$$\begin{aligned} \frac{\partial \mathbf{E}(\mathbf{r})}{\partial t} = & \left[ \frac{1}{b} \frac{d^2 b}{dt^2} - 3 \left[ \frac{1}{b} \frac{db}{dt} \right]^2 \right] \left[ \frac{b_0}{b} \right]^2 \sum_{l,m} (2\mathbf{A}_{l,m}(r_s) + \\ & r_s \mathbf{A}'_{l,m}(r_s)) Y_{l,m}(\theta, \phi) - \left[ \frac{1}{b} \frac{db}{dt} \right]^2 \left[ \frac{b_0}{b} \right]^2 r_s \sum_{l,m} (3\mathbf{A}'_{l,m}(r_s) + r_s \mathbf{A}''_{l,m}(r_s)) Y_{l,m}(\theta, \phi) \end{aligned} \quad (4-13)$$

The partial derivative of  $\mathbf{B}$  with respect to  $x_k$  is given by:

$$\begin{aligned} \frac{\partial B(r)}{\partial x_k} = & \left[ \frac{b_0}{b} \right]^4 \sum_{l,m} \left[ \frac{\partial \nabla_s Y_{l,m}(\theta, \phi)}{\partial x_{sk}} \times A_{l,m}(r_s) + Y_{l,m}(\theta, \phi) \frac{x_k}{r} \frac{r}{r} \times A_{l,m}''(r_s) \right. \\ & \left. + \left[ \frac{\partial Y_{l,m}(\theta, \phi)}{\partial x_{sk}} \frac{r}{r} + \frac{x_k}{r} \nabla_s Y_{l,m}(\theta, \phi) + Y_{l,m}(\theta, \phi) \left( \frac{1}{r_s} \frac{\partial r_s}{\partial x_{sk}} - \frac{x_{sk} r_s}{r_s^3} \right) \right] \times A_{l,m}'(r_s) \right] \end{aligned} \quad (4-14)$$

The partial derivative of  $B$  with respect to  $t$  is given by:

$$\begin{aligned} \frac{\partial B}{\partial t} = & -\frac{1}{b} \frac{db}{dt} \left[ \frac{b_0}{b} \right]^3 \sum_{l,m} [2 \nabla_s Y_{l,m}(\theta, \phi) \times A_{l,m}(r_s) \\ & + \left[ r_s \nabla_s Y_{l,m}(\theta, \phi) + 3 Y_{l,m}(\theta, \phi) \frac{r}{r} \right] \times A_{l,m}'(r_s) + Y_{l,m}(\theta, \phi) r_s \times A_{l,m}''(r_s)] \end{aligned} \quad (4-15)$$

The time dependence used for the CRRES trajectory computations was based upon a fit of magnetic field data for the March 1991 storm obtained by Karl Pfister. It is given in the following equation:

$$\begin{aligned} b(t) = & \left[ 1 + 9 \left[ \frac{t}{30} \right]^{1.3} \right]^{\frac{1}{3}} E.R. \text{ for } 0 \leq t \leq 30 \text{ sec.} \\ = & 10^{\frac{1}{3}} E.R. \text{ for } t > 30 \end{aligned} \quad (4-16)$$

The above expression has a mathematical singularity in its derivatives at  $t = 0$ . For the actual trajectory computations,  $t$  was replaced by  $(t + 0.001 \text{ sec.})$ .

In the first step of testing the trajectory program for direct integration of the equations of motion, proton trajectories were computed for a dipole field, and the results were compared to analytical computations. Since energy is conserved for this case, the variable step size control parameters were chosen to insure that the computed energy remained constant to an accuracy of a few electron volts. The guiding center trajectory code uses the same integration routines, and requires the computation of the electric and magnetic fields and their partial derivatives with respect to the spatial coordinates and the time. Parallel computations were performed, in which the initial conditions (position and velocity) for the proton guiding center calculation were used to compute the position vector for the direct proton computation. The parallel guiding center trajectories and the corresponding direct proton trajectories were then compared, using graphs similar to those in Figures 15 through 17.



#### 4.2.4 Applications

##### 4.2.4.1 Adiabatic Invariants

A simple way to check the results of the trajectory analysis is to compare the computed radial transport and acceleration with what would be obtained assuming that the adiabatic invariants are constant. In a dipole field, 20 MeV protons have drift periods of 22-45 sec, for  $L = 3-6 R_E$ , while 50 MeV protons have drift periods of 9-18 sec over the same  $L$  range. Thus, if we assume a time scale for the magnetic field compression of 30 sec, the adiabatic results for 50 MeV protons, with periods considerably smaller than 30 sec, should be in near agreement with the results obtained from the exact trajectories, while for lower energies, there should be some disagreement.

The adiabatic invariants are defined as the action integrals corresponding to the basic three approximately separable periodic components of the magnetospherically trapped particle's motion: the spiraling motion of the particle about a guiding center, the motion of the guiding center along field lines, and the longitudinal drift motion of the guiding center around Earth. In the absence of an electric field component parallel to the magnetic field, the first invariant reduces to a very simple expression:

$$\mu = \frac{p^2}{2mB_m} \quad (4-17)$$

where  $p$  is the particle's momentum,  $m$  its mass, and  $B_m$  is the mirror point magnetic field magnitude, given by:

$$B_m = \frac{B}{\sin^2 \alpha} \quad (4-18)$$

where  $B$  is the magnetic field magnitude at a given location traversed by the particle, and  $\alpha$  is the pitch angle at that location.

The second adiabatic invariant is given by

$$J = 2pI_m \quad (4-19)$$

where,

$$I_m = \int \sqrt{1 - \frac{B(s)}{B_m}} ds \quad (4-20)$$

with the integral taken along the field line between the particle's mirror points.  $B(s)$  is the magnetic field magnitude at a point  $s$  on the field line.

In these expressions and in what follows, the subscript  $m$  is used to designate a mirror point quantity. Thus,  $B_m$  is the magnetic field at the mirror point of a particle, as opposed the point of observation.  $I$ , without the subscript, can be considered a function of position if  $B_m$  is replaced by  $B$  at the position in question and the integral is taken between that position and its conjugate point. The subscript emphasizes the dependence of these quantities on the mirror points rather than the position of observation. The mirror point, in turn, is a function of the point of observation and the pitch angle.

The third adiabatic invariant is given by

$$\Phi = \int \mathbf{B} \cdot d\mathbf{a} \quad (4-21)$$

where the integral is over any surface enclosed by the drift orbit.

Note that, if the magnetic field is static, and no electric field is present, the particle momentum is fixed, and the parameters  $I_m$  and  $B_m$  serve equally as well as the adiabatic invariants for parameterizing the particle trajectories, since they are then functions of  $\mu$  and  $J$  and are, therefore, themselves invariant. Thus,  $I_m$  and  $B_m$  specify the set of mirror points through which the particle passes in its orbit, and therefore, completely specify the orbit. In this case, the third invariant, the flux enclosed by the drift orbit, is not an independent parameter. However, its place as a constant of the motion may be taken by the particle's energy. The constancy of these parameters disappears in time-varying fields, in which the resulting induction electric field does work on the particles, thus, changing their energies and momenta.  $I_m$  and  $B_m$  must correspondingly be adjusted to conserve  $\mu$  and  $J$ .

*McIlwain* [1963] has defined the shell parameter  $L_m$  as a function of  $I_m$  and  $B_m$ . This parameter is, therefore, adiabatically conserved if  $I_m$  and  $B_m$  are. In a dipole field,  $L_m$  is the equatorial crossing distance of the shell of field lines through which the particle passes. Therefore, at a given location all particles have the same  $L_m$  value, regardless of pitch angle. Since this relationship remains approximately valid in Earth's internal field,  $L_m$  has a distinct advantage over  $I_m$  for organizing the inner belts. As a function of position,  $L$  is constant along a dipole field line and approximately constant along field lines of Earth's internal field.

### *Equivalent Parameters*

A problem with the adiabatic invariants is their lack of familiarity. We are more accustomed to energy spectra, radial distributions, and pitch angle distributions. Thus, we are motivated to define a set of equivalent invariants - the energy,  $L_m$ , and equatorial pitch angle that particles with a given set of adiabatic invariants would attain if the magnetic field changed adiabatically to a reference dipole field [Roederer, 1970, 1972]. We call these parameters *dipole-equivalent invariants*. First, for the dipole-equivalent  $L_m$ , we have:

$$L_{md} = -2\pi M/\Phi \quad (4-22)$$

where  $M$  is the dipole moment of the chosen dipole reference field. A review of Roederer [1970] and Schulz and Lanzerotti [1974] leads to the conclusion that this is the  $L$  parameter used by them in diffusion equations, rather than McIlwain's parameter. Unlike the latter,  $L_{md}$  is a function of the third adiabatic invariant, and therefore would not change under adiabatic variations of the magnetic field. Furthermore, this  $L_{md}$  is actually independent of a particle's mirror points in a symmetric non-dipole field. Thus, any dependence on mirror points reflects shell-splitting in an asymmetric field.

To obtain the dipole-equivalent equatorial pitch angle,  $\alpha_d$ , we note the following [Roederer, 1970]:

$$I_m^2 B_m = \text{constant} \quad (4-23)$$

which follows from Eqs. (4-17) and (4-19), and constancy of  $J$  and  $\mu$ . After substituting known dipole expressions for  $B_{md}$  and  $I_{md}$ , as functions  $L_{md}$  and  $\alpha_d$ , we solve for  $\alpha_d$ . Finally, constancy of the first adiabatic invariant supplies the ratio  $p_d/p$ , where  $p_d$  is the dipole-equivalent momentum, and  $p$  is the observed momentum. From this ratio, we may obtain the dipole-equivalent energy  $E_d$  for any observed energy.

#### 4.2.4.2 Application

We consider a time varying Mead field with a standoff distance which changes from 10  $R_E$  to 5  $R_E$  in 60 and 30 seconds, respectively. For a proton at 90° equatorial pitch angle, we wish to compute its energy and radial position at 2.66 hr magnetic local time (the SSC local time at CRRES) in the final compressed field, as functions of its positions and energy in the initial field. This has been done in four steps:

- i. Compute the dipole equivalent  $L$  and momentum ratio  $(p_d/p)$  of a  $90^\circ$  equatorial pitch angle particle at 2.66 hr MLT as functions of radial (equatorial) distance in the final ( $5 R_E$  standoff distance) magnetic field. From the resulting table, radial distance and momentum ratio are developed as spline functions of the dipole-equivalent  $L$ , valid for the specified pitch angle and local time.
- ii. Compute the dipole-equivalent  $L$  and the momentum ratio for a specified initial position (equatorial radial distance and local time) of a  $90^\circ$  equatorial pitch angle particle in the initial magnetic field.
- iii. At this dipole equivalent  $L$ , which is assumed to be adiabatically conserved during the compression, interpolate the functions derived from step 1 (radial distance and momentum ratio as functions of dipole-equivalent  $L$ ) to obtain the radial distance and momentum ratio in the final field.
- iv. The ratio of final to initial energy, taking the protons to be nonrelativistic, is then

$$\frac{E_{final}}{E_{initial}} = \frac{(p_d/p)_{initial}^2}{(p_d/p)_{final}^2} \quad (4-24)$$

Tables 20 and 21 compare the results of the two methods for selected initial conditions in the noon and midnight meridians. Shown are the radial distances (at 2.66 hr MLT) and the percent energy changes, assuming that the adiabatic invariants are constant ("adiabatic"), and the corresponding results for the guided center trajectory for various initial energies. Actual trajectories were also computed, but better agreement was obtained for the guided center computations. Note that the "adiabatic" results are independent of energy. Sufficient results are given to warrant some conclusions:

- i. Although the particles starting at the larger distances can be transported inwardly and accelerated significantly, they cannot be transported to the CRRES location ( $2.55 R_E$ ) from outside  $4 R_E$ , the inner boundary of the prestorm solar proton population. Acceleration of the protons near the CRRES location is less than 36%, which is insufficient to account for the observed flux increase there if we exclude inward radial transport. This conclusion is consistent with both the adiabatic and the numerical results.
- ii. There is disagreement in detail between the adiabatic and numerical results, even at the highest energy (50 MeV), where we expected the agreement to be good.

A similar analysis was performed using the Karl Pfizter model. The results of the analysis are presented in Table 22.

### 4.3 TRAJECTORY COMPUTATION SUMMARY

#### 4.3.1 Description of Trajectories

The proton trajectory computations performed with the time variable Mead Model (60, 30, and 5 second change of the standoff distance from 10 to 5  $R_E$ ) indicate that additional fields or transient phenomena are required. To obtain an estimate of what is required, for the 5 second case an additional constant electric field (for the 5 second interval) of 1 V/m in the dawn direction was added, with the result that it was possible to move 90 degree pitch angle protons originally at noon MLT at  $L = 4 R_E$  to about  $L = 2.5$  at the CRRES location. Tables 23 and 24 provide a summary of the trajectory computations for the direct relativistic equations of motion and the relativistic guiding center equations of motion, respectively.

#### 4.3.2 Dependence of Initial Conditions

For the time-dependent field models, it was observed that energy gains were substantially larger for protons at local noon as compared to local midnight. In addition, the direction of the velocity vector had a noticeable effect. For the local noon protons, using the Guiding Center equations of motion, the energy gained for initial velocities in the +y and -y direction were identical; the energy gained was greater for the initial velocities in the +x direction than for the -x direction. For direct integration, the energy gain was variable, with protons gaining more energy on the outer portion (for pitch angle = 90 degrees) of the cycloid, than was lost on the inner portion. The energy gained was dependent on where (in the cycloid "phase") the proton was at the initial time, and at the time at which the field stopped changing.

#### 4.3.3 Results

We have been unable to find any trajectories using the time variable fields (and their induced electric fields) used in this study which correspond to the creation of the new radiation belt at the CRRES  $L = 2.5 R_E$  at 2.66 MLT location from lower energy pre-storm protons originally at  $L = 4$ . An additional electric field of about 1 V/m for the Mead model with Voigt-Hilmer ring current (somewhat less for the modified Mead model with Voigt Hilmer ring current) appears to be required.

**TABLE 20. Proton Trajectories for Compression of Standoff Distance  
from 10 to 5  $R_E$  in 30 Seconds**

Initial Magnetic Local Time (hr)	Initial SM Radial Distance ( $R_E$ )	Initial Energy (MeV)	Final SM Radial Distance ( $R_E$ ) at CRRES Local Time (2.66 hr)	% Energy Change
12	3.0	Adiabatic	2.76	36
		10	2.77	35
		20	2.83	27
		30	2.74	37
		40	2.73	39
		50	2.78	32
12	4.0	Adiabatic	3.37	84
		10	3.49	62
		20	3.43	69
		30	3.28	91
		40	3.43	67
		50	3.35	78
12	5.0	Adiabatic	3.81	152
		10	3.97	108
		20	3.70	143
		30	3.70	148
		40	3.80	129
		50	3.68	147
12	6.0	Adiabatic	4.25	217
		10	ejected	
		20	3.95	224
		30	3.98	214
		40	4.00	208
		50	3.90	224
12	7.0	Adiabatic	4.44	236
		10	ejected	
		20	4.10	305
		30	4.00	324
		40	4.14	284
		50	4.07	296
0	3.0	Adiabatic	2.76	36
		10	2.77	36
		20	2.72	43
		30	2.79	33
		40	2.80	31
		50	2.79	37
0	4.0	Adiabatic	3.35	81
		10	3.30	94
		20	3.31	92
		30	3.49	66
		40	3.34	85
		50	3.40	76
0	5.0	Adiabatic	3.76	142
		10	3.67	176
		20	3.84	143
		30	3.80	148
		40	3.70	163
		50	3.85	136
0	6.0	Adiabatic	4.11	198
		10	3.93	284
		20	4.12	236
		30	4.04	249
		40	3.95	265
		50	4.08	234

**TABLE 21. Proton Trajectories for Compression of Standoff Distance  
from 10 to 5  $R_E$  in 60 Seconds**

Initial Magnetic Local Time (hr)	Initial SM Radial Distance ( $R_E$ )	Initial Energy (MeV)	Final SM Radial Distance ( $R_E$ ) at CRRES Local Time (2.66 hr)	% Energy Change
12	3.0	Adiabatic	2.76	36
		10	2.83	27
		20	2.73	40
		30	2.76	35
		40	2.77	34
		50	2.75	36
12	4.0	Adiabatic	3.37	84
		10	3.42	71
		20	3.40	68
		30	3.35	79
		40	3.32	82
		50	3.36	76
12	5.0	Adiabatic	3.81	152
		10	3.73	146
		20	3.79	135
		30	3.81	129
		40	3.81	129
		50	3.75	135
12	6.0	Adiabatic	4.25	217
		10	3.95	228
		20	3.98	217
		30	4.01	211
		40	4.01	205
		50	4.03	189
12	7.0	Adiabatic	4.44	236
		10	4.10	312
		20	4.13	298
		30	4.15	287
		40	ejected	297
0	3.0	Adiabatic	2.78	36
		10	2.72	43
		20	2.80	32
		30	2.77	35
		40	2.76	36
		50	2.79	33
0	4.0	Adiabatic	3.35	81
		10	3.32	91
		20	3.34	87
		30	3.38	80
		40	3.42	73
		50	3.39	78
0	5.0	Adiabatic	3.76	142
		10	3.91	130
		20	3.73	163
		30	3.73	160
		40	3.77	152
		50	3.78	147
0	6.0	Adiabatic	4.11	198
		10	4.25	237
		20	3.99	265
		30	3.98	263
		40	4.02	251
		50	4.03	243

**TABLE 22.** Comparison of Adiabatic Calculations with Guiding Center Trajectory Calculations of Energy Gain and Radius at CRRES Location for Karl Pfitzer Dynamical Field Model

Initial Radius	Initial Energy	R at CRRES E. R.	Energy Gain %	R at CRRES E. R.	Energy Gain %
E. R.		Local Noon		Local Midnight	
3.0	adiabatic	2.79	30	2.80	30
	10 MeV	2.75	36	2.92	15
	20 MeV	2.87	19	2.75	37
	30 MeV	2.82	26	2.80	30
	40 MeV	2.78	31	2.83	25
	50 MeV	2.83	25	2.79	31
4.0	adiabatic	3.44	67	3.46	68
	10 MeV	3.50	59	3.62	49
	20 MeV	3.59	48	3.41	76
	30 MeV	3.44	67	3.55	56
	40 MeV	3.54	54	3.45	69
	50 MeV	3.48	61	3.52	59
5.0	adiabatic	3.92	118	3.96	124
	10 MeV	4.16	86	4.16	100
	20 MeV	4.05	102	4.03	116
	30 MeV	4.02	102	4.01	117
	40 MeV	4.03	101	4.04	111
	50 MeV	4.00	102	4.02	113
6.0	adiabatic	4.27	182	4.36	198
	10 MeV	4.66	129	4.62	165
	20 MeV	4.40	168	4.55	169
	30 MeV	4.52	147	4.39	193
	40 MeV	4.38	133	4.49	174
	50 MeV	4.46	150	4.45	179



TABLE 23. Proton Trajectory Data - Relativistic Equations of Motion				
Initial Position E. R.	Velocity Direction	Initial Energy MeV	Final Energy MeV	Midnight Radius E.R.
(8.5,0,0)	(0,-1,0)	20.0	125.74	3.6
(8,0,0)	(0,-1,0)	20.0	120.52	3.5
(7,0,0)	(0,-1,0)	20.0	106.54	3.3
(6,0,0)	(0,-1,0)	20.0	90.27	3.1
(5,0,0)	(0,-1,0)	20.0	77.65	2.8
(4,0,0)	(0,-1,0)	20.0	58.09	2.5
(3.5,0,0)	(0,-1,0)	20.0	48.78	2.4
(3,0,0)	(0,-1,0)	20.0	41.03	2.2
(2.5,0,0)	(0,-1,0)	20.0	33.58	2.0
(8,0,0)	(0,1,0)	20.0	162.77	3.6
(6,0,0)	(0,1,0)	20.0	115.22	3.6
(4,0,0)	(0,1,0)	20.0	68.16	2.8
(3,0,0)	(0,1,0)	20.0	43.79	2.3
(-8,0,0) to (-3.5,0,0)	(0,-1,0)	20.0 10.0		ejected
(-3,0,0)	(0,-1,0)	20.0	13.71	3.6
(-2.5,0,0)	(0,-1,0)	20.0	14.92	2.7
(-8,0,0) to (-4,0,0)	(0,1,0)	20.0		ejected
(8.5,0,0)	(0,-1,0)	10.0	96.60	3.5
(8,0,0)	(0,-1,0)	10.0	90.37	3.3
(7,0,0)	(0,-1,0)	10.0	76.47	3.2
(6,0,0)	(0,-1,0)	10.0	60.87	3.1
(5,0,0)	(0,-1,0)	10.0	40.09	2.8
(4,0,0)	(0,-1,0)	10.0	31.85	2.6
(3.5,0,0)	(0,-1,0)	10.0	26.29	2.4
(3,0,0)	(0,-1,0)	10.0	21.24	2.2

TABLE 24. Proton Trajectory Data - Guiding Center Equations of Motion				
Initial Position E. R.	Velocity Direction	Initial Energy MeV	Final Energy MeV	Midnight Radius E.R.
(8.5,0,0)	(0,-1,0)	20.0	148.54	3.6
(8,0,0)	(0,-1,0)	20.0	137.10	3.6
(7,0,0)	(0,-1,0)	20.0	116.94	3.6
(6,0,0)	(0,-1,0)	20.0	91.20	3.4
(5,0,0)	(0,-1,0)	20.0	83.20	3.1
(4,0,0)	(0,-1,0)	20.0	62.48	2.7
(3.5,0,0)	(0,-1,0)	20.0	51.80	2.6
(3,0,0)	(0,-1,0)	20.0	42.24	2.4
(2.5,0,0)	(0,-1,0)	20.0	34.44	2.1
(8.5,0,0)	(0,-1,0)	10.0	95.58	3.5
(8,0,0)	(0,-1,0)	10.0	91.59	3.4
(7,0,0)	(0,-1,0)	10.0	80.34	3.3
(6,0,0)	(0,-1,0)	10.0	65.75	3.1
(5,0,0)	(0,-1,0)	10.0	49.38	3.0
(4,0,0)	(0,-1,0)	10.0	33.76	2.7
(3.5,0,0)	(0,-1,0)	10.0	27.17	2.6
(3,0,0)	(0,-1,0)	10.0	21.73	2.4
(2.5,0,0)	(0,-1,0)	10.0	17.50	2.1

## 5. ONR-604 PROCESSING FOR HEAVY ION COMPOSITION AND SPECTRA

### 5.1 INTRODUCTION--GOALS

The University of Chicago's heavy ion/solar flare instrument detects protons and heavy nuclei up to  $Z=26$  in the energy range  $\sim 25$ -300 MeV/nucleon [Simpson, *et al.*, 1985]. Ideally, determination of fluxes is performed by detailed analysis of the trajectories and energy losses of particles passing through the instrument's detector stack [Wefel and Guzik, 1991]. Rather than pursue this analysis, we have focussed on the separation of pure Helium from one of the priority count rates, P2, using a simpler procedure recommended by University of Chicago personnel. The P2 count rate nominally includes Helium nuclei in the range 42-105 MeV/nucleon, plus heavier nuclei up to Neon. Application to the March, 1991, magnetic storm is reported here. Although extraction of the rates of individual heavier species up to Neon was hoped for, this has not been carried out, due to the far greater number of orbits that must be processed to overcome the poor statistics associated with lower counting rates of these species.

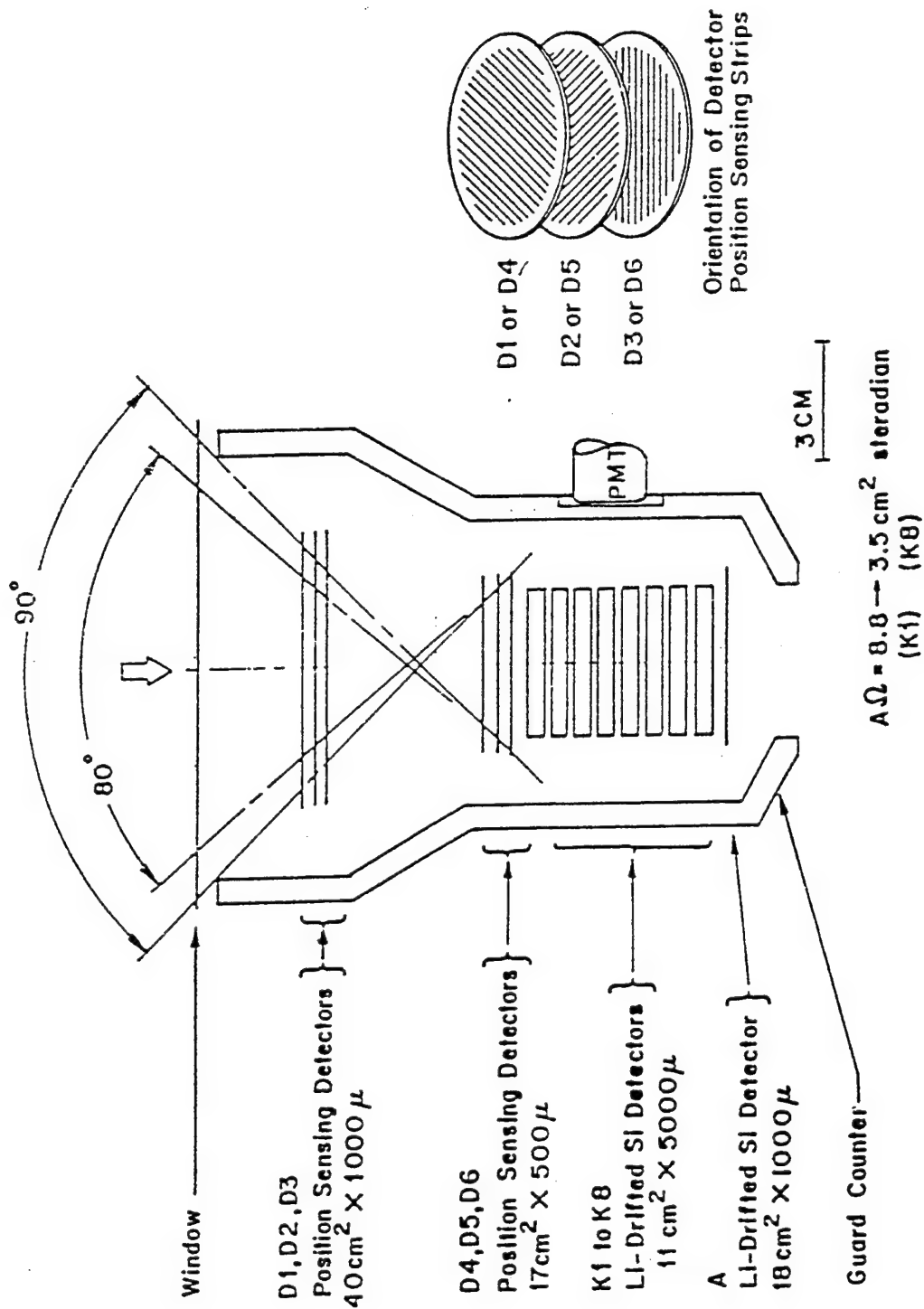
### 5.2 DESCRIPTION OF INSTRUMENT

The nuclei can be identified by specie and energy through a detailed analysis of the pulse heights that a particle generates in a stack of detectors shown in Figure 18 [Simpson, *et al.*, 1985]. Two series of detectors are shown: those labeled D1-D6, which are also used to determine the trajectory of the particle, and detectors K1-K8. The D1-D6 (position-sensing) detectors each provide two pulse heights. The E pulse height gives the total energy lost in the detector, while the P and E pulse heights together tell us which of a series of parallel gold strips the particle crossed. Thus one coordinate in a direction normal to the telescope axis is available from each position-sensing detector. At least 4 such readings are needed to determine the trajectory; six are provided for redundancy. A matrix of total energy lost in a set of one or more consecutive detectors vs the total energy lost in a group of subsequent detectors (Fig. 19) ideally results in a display of tracks representative of the various nuclear species. Thus, an individual particle can be identified by the track it lies on, and its energy by the detector in which it stops. Such a clear picture arises only if all the particles are incident normally to the detectors; thus, we get a fuzziness due to the spread in directions. Chicago has developed algorithms to apply corrections for angular direction, but these have not been used here.

Also shown are an "A" detector in the back of the stack, and a scintillation guard counter, also referred to as "S", surrounding the stack. There is no pulse height information from these two detectors; all that is given for each detector is a flag bit indicating whether the detector was hit. Particles hitting the scintillator either entered the side, or passed through the detector at a wide enough angle to exit the side. Those which hit the A detector are in aperture, but have too much energy to stop in the instrument.

Only 2 full PHA (Pulse Height Analysis) readouts can be obtained per second. Thus, a priority

# High Energy Telescope



The University of Chicago

Figure 18. The ONR-604 design.

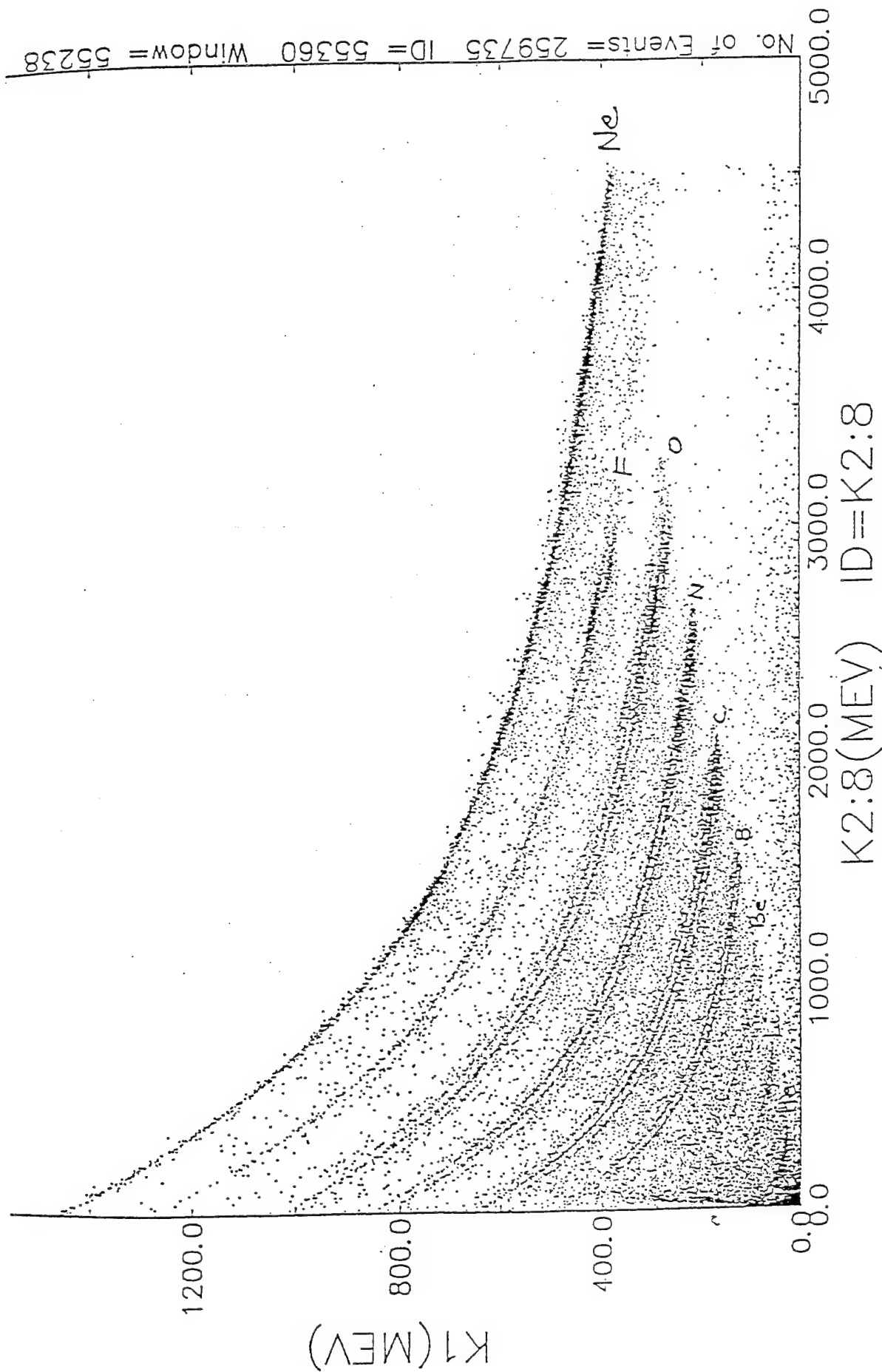


Figure 19. A matrix of energy loss in detector K1 vs total energy loss in K2-K8, for individual events, denoted by points. Note the tracks characteristic of individual nuclear species.

scheme has been set up such that an event (particle passing through the instrument) occurring in a certain priority group takes precedence over any earlier events of lower priority which occurred in the same half-second readout interval. Three priority groups are defined: the highest, P1, includes particles heavier than Neon. The medium priority, P2, nominally consists of Helium through Neon, while the lowest, P3, is everything else, principally Hydrogen and electrons. The priority of an event is identified by predefined coincidence/anticoincidence requirements. Rate counters accumulate the total number of events (not just those read out) in each priority for normalization of the results of the readout events. The heavier nuclei that are detected, beginning with He, are not necessarily bare (fully charged) upon arrival at the instrument. Such nuclei can lose electrons in the front entrance window (Fig. 18), and subsequently travel through the telescope as fully charged. The instrument cannot distinguish these events from those of nuclei which actually do arrive fully charged.

Table 25 shows the coincidence/anticoincidence requirements for the three priorities. In this notation, multiplication means logical "and", while addition means logical "or". A bar over a symbol means anticoincidence. Thus, the P3 logic requirement is that detectors D1, D2, and D3 were all hit, and that either the scintillation guard counter (S) was not hit, or at least one of the first two K detectors was hit. This logic requirement, also referred to as "gate control", must be satisfied, in addition to other specific requirements for the medium and high priorities. In these latter two priorities, the terms K1M, K2M, K1H, etc., refer to the medium (M) and high (H) energy loss thresholds which must be exceeded for the various K detectors. These are given in Table 26.

Also shown in Table 25 is the ground command word. The important bit here is the proton mode bit, which indicates whether the instrument is in proton or "normal" mode. This is defined by D detector energy loss thresholds given in Table 26. The purpose of the normal mode is to screen out the high proton "background" associated with the belts. Therefore, after initial exploratory phases, the instrument operated on a schedule (beginning with orbit 63) of normal mode below 26000 km altitude and proton mode above. Figure 20 shows the effect on the rates of switching between the two modes (the count rates in P3 and P2 jump up when switching from normal to proton mode, and back down when switching back to normal mode.). Notice also, in Figure 20, that, outside the heart of the inner proton belt, the P1 and P2 count rates are very low ( $\sim 10/\text{min}$  for P2,  $1/\text{min}$  for P3). At such low levels, it is expected that, in the priority system, the detailed pulse height analysis would be read out for nearly all P1 and P2 events. Then the count rate for a particular subgroup of events (say He) could be obtained by directly counting the events read out that can be classified within this group. The high counts in P3 during proton mode are evidently due to electrons. In spite of the high threshold settings in normal mode, the P2 and P3 count rates peak in the belts. This is evidently due to multiple proton pileup, if, for instance, the combined energy loss in a detector due to two protons exceeds the threshold. Energy loss matrix plots taken during belt passage do not contain the characteristic He track, indicating that He makes negligible or no contribution to the P2 peaks.

TABLE 25. ONR-604 Pulse Height Analysis Gate Control and Priority Logic, and Ground Command		
Gate Control	$GC = DID2D3\bar{S} + DID2D3(K1 + K2)$	
Priority 3 (Low)	$P3 = GC$	
Priority 2 (Medium)	$P2 = GC (K1M + K2M) \bar{A}$	
Priority 1 (High)	$P1 = GC (K1H + K2H + K3H + K4H + K5H + K6H + K7H + K8H)$	
Ground Commands	16 Bit Serial Digital Command Word	
Bit No. (In Order Received)	Function	
1	Start Calibrate Sequence	
2	Override Calibrate	
3	Disable D1	
4	Disable D2	
5	Disable D3	
6	Disable K1	
7	Disable K2	
8	Disable A	
9	Disable S	
10	Inhibit P2	
11	Inhibit P3	
12	Set Proton Mode	
13 - 16	Spares	

TABLE 26. ONR-604 Detector Thresholds (MeV)			
Detector	Normal Mode	Proton Mode	
D1	4.45	0.77	
D2	4.53	0.78	
D3	4.55	0.78	
D4	1.65	0.28	
D5	1.71	0.29	
D6	1.69	0.29	
Normal Mode and Proton Mode			
	Low	Medium	High
K1	0.693	36.9	1205
K2	0.647	37.9	1082
K3	0.653	-	1199
K4	0.654	-	1197
K5	0.668	-	1197
K6	0.649	-	1201
K7	0.680	-	1209
K8	0.664	-	1194
A	0.214	-	-



1990-11-26

QNR 604: ORBIT # 75 DAY 237 YEAR 90

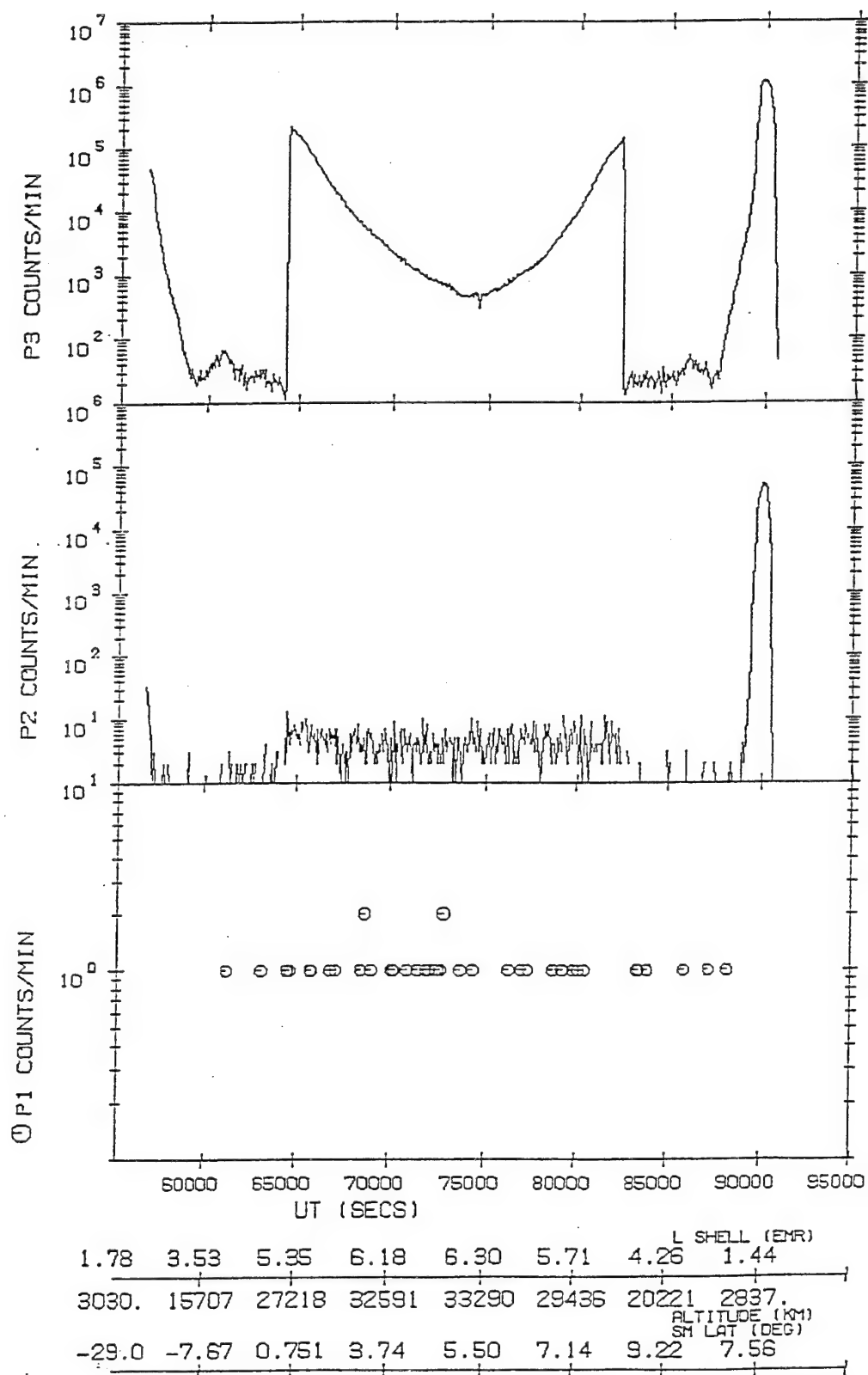


Figure 20. Count Rates for the priority groups P1, P2, and P3, for orbit 75.

### 5.3 EVENTS AND RATE TIMINGS

The assignment of times to individual events and the priority rates, based on the master frame times in the Phillips Laboratory (PL) Time History Data Base (THDB), is based on the following information. Each 4.096 second time period is divided into 8 segments, each 0.512 seconds in duration. These are numbered (mpx or mux number) from 0 through 7. At most, one event is read out from each segment. The priority rates are accumulated in a 4.096 second interval, beginning at the start of the segment whose mux number is 0. They must be read out during the 4.096 second interval following their accumulation. On the PL THDB, one master frame is a collection of 4.096 seconds of telemetered data. The mux number of the first time segment in the master frame in the THDB varies, and thus, is not necessarily zero. The time given in the THDB for the master frame is the readout time of the first segment given. This is at the end of the data collection interval for this segment. From this, it follows that the event, if any, recorded during this segment occurred during the 0.512 second interval ending at the THDB master frame time. For simplicity, we have assigned the event time to be at the midpoint of this interval, 0.256 before the THDB master frame time. A more accurate assignment within the 0.512 second interval will not be needed for our purposes. The times of the subsequent events included in the master frame readout are later than this time by the appropriate multiples of 0.512 seconds. Thus, in general

$$t_i = t_{mf} - 0.256s + [\text{modulo}(\text{mux}_i - \text{mux}_0 + 8, 8)]0.512s \quad (5.1)$$

where  $t_i$  is the time of event in segment  $i$  in the master frame,  $t_{mf}$  is the master frame time,  $\text{mux}_i$  is the mux number of the segment  $i$ , and  $\text{mux}_0$  is the mux number of segment 0, the first segment in the master frame.

The master frame time is the time at the end of the data collection interval of segment  $\text{mux}_0$  of the current 4.096 second rate accumulation interval, which began at the beginning of the most recent  $\text{mux}=0$  segment. The rates given in this master frame apply to the previous rate accumulation interval, which began 4.096 seconds before the current accumulation interval began. Therefore, the start time of the accumulation interval for the rates given in the current master frame is:

$$t_r = t_{mf} - 4.096s - 0.512s (\text{mux}_0 + 1) \quad (5.2)$$

#### 5.4 EXTRACTION OF PURE PROTON AND HELIUM COUNT RATES

The basic equation for the count rate  $N_i$  of a nuclear type is

$$N_i = R_j f_i \quad (5.3)$$

where  $R_j$  is the count rate of priority group  $j$  (P1, P2, or P3) to which the nuclear type belongs and  $f_i$  is the fraction of counts of the priority group  $j$  due to this type. The nuclear type is specified by the specie (such as H or He) or specie group (such as CNO, Carbon-Nitrogen-Oxygen) and possibly by further delimiting parameters such as energy.

The fraction  $f_i$  is estimated as

$$f_i = C_i / C_j \quad (5.4)$$

where  $C_i$  is the count of events identified by pulse height analysis due to nuclear type  $i$ , and  $C_j$  is the total number of events in the appropriate priority group that have been pulse-height analyzed over the same time period. Figures 21 and 22 show sample matrices for the priority groups P2 (containing Helium) and P3 (protons). The points due to protons and Helium are clustered in tracks surrounded by polygons in the figures. We define the counts of the target species as the count of points lying within the polygons. This represents a compromise between simply counting all points below a prescribed straight line, which would include many points significantly distant from the tracks, and some more elaborate method of characterizing the curvatures and widths of the track. For protons there is approximately a 20-50% difference between the two simpler methods. In the He case, it is seen that counting all the particles on the grid would include a triangular cluster well below the main track.

The matrices include only those nuclei which are stopped in the K2-K8 detector stack corresponding to energies of 52-108 MeV/nucleon. For the P3 priority group this typically includes less than 10% of the particles. Most of the rest are stopped before reaching the K stack (they may be electrons, or protons with insufficient energy to reach the stack), or particles that travel all the way through the instrument to the A detector, or to the surrounding shield. A candidate is rejected if it meets one of the following 5 conditions:

ONR 604: ORBITS 586 - 586  
PROTON MODE  
EPH HIGH  
PRIORITY: 2

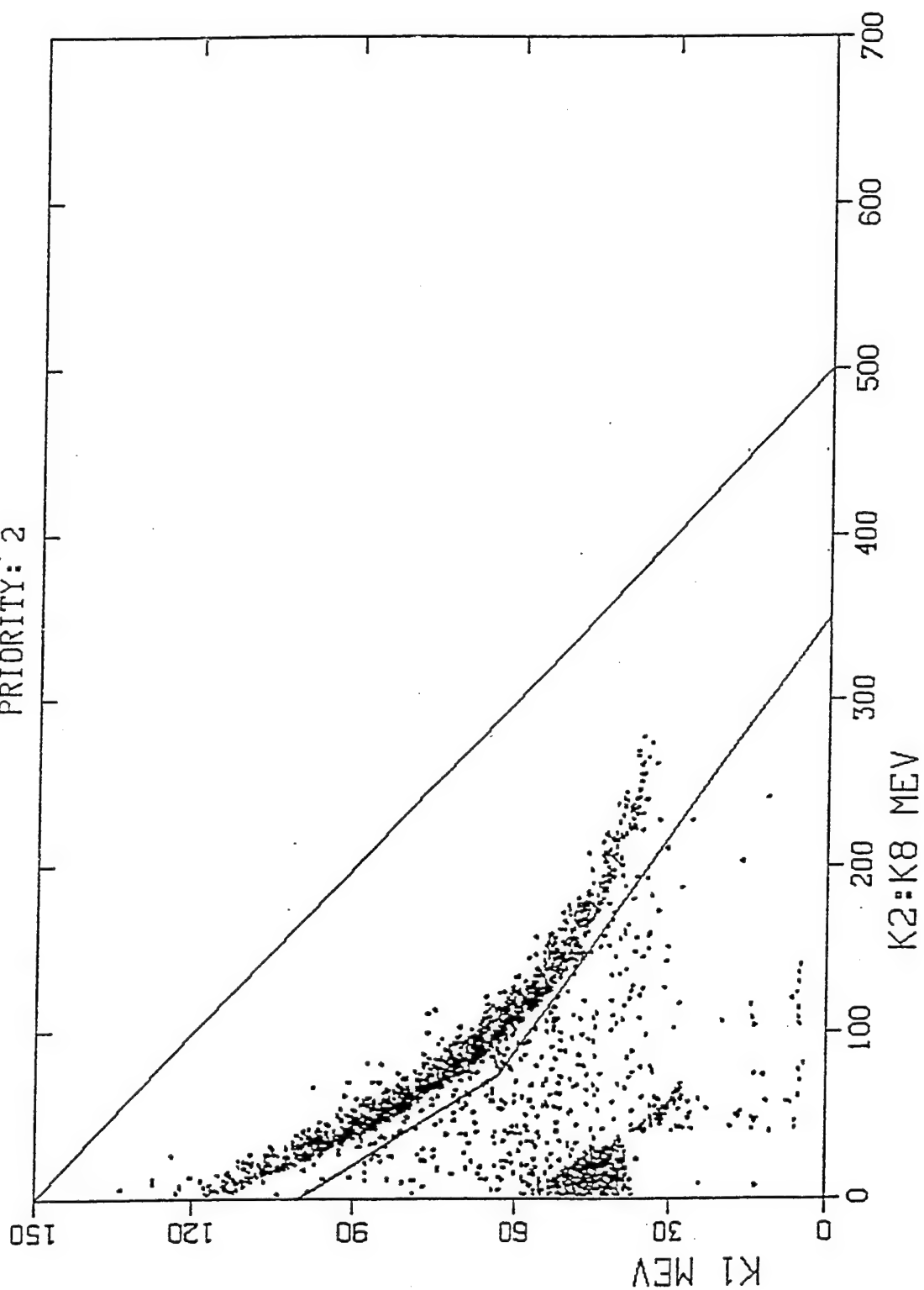


Figure 21. P2 proton mode event matrix for orbit 586.

ONR 604: ORBITS 586 - 586  
PROTON MODE  
ALL EPH  
PRIORITY: 3

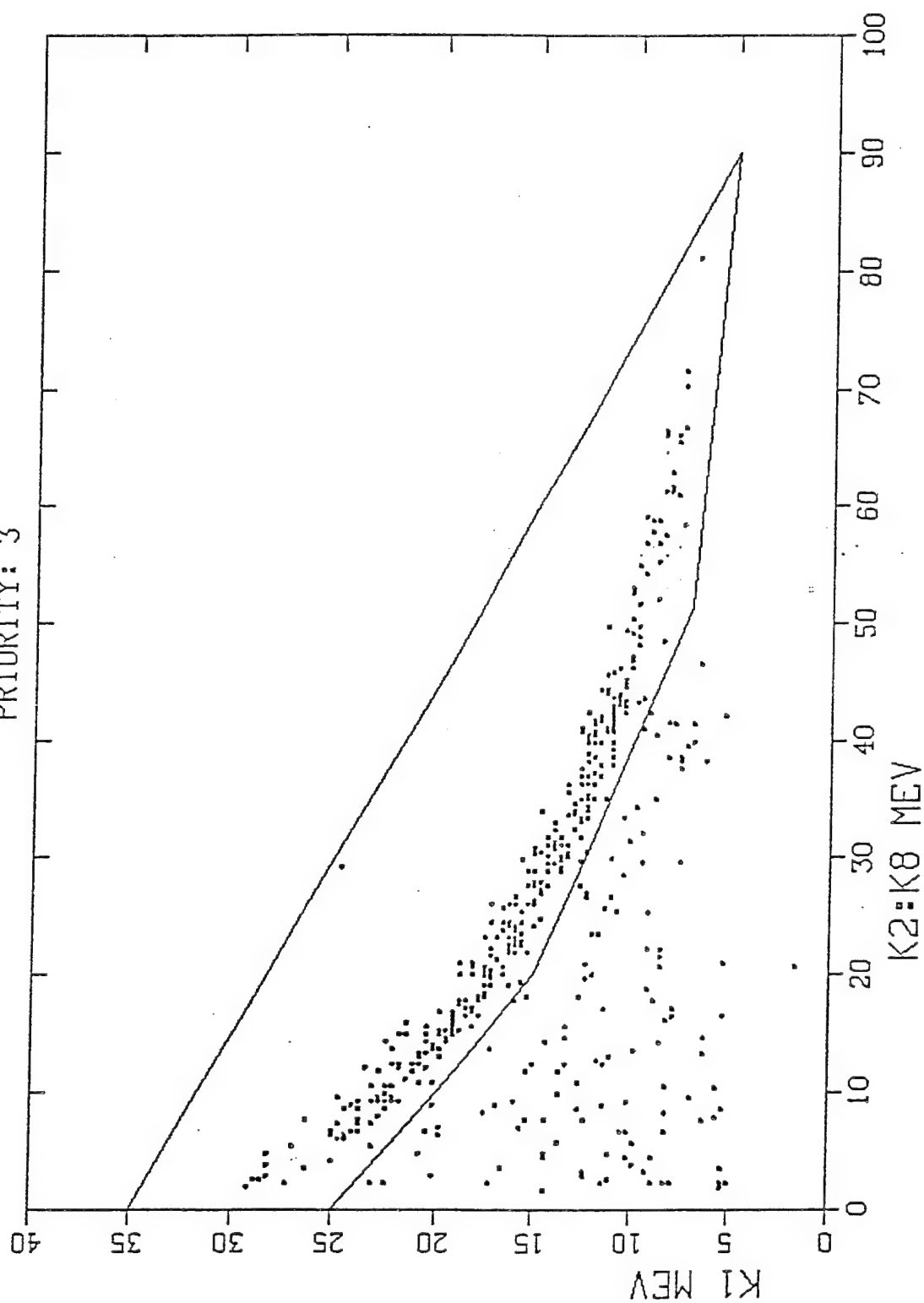


Figure 22. P1 proton mode event matrix for orbit 586. The polygon shows events that were counted as Hydrogen.

1. Failed to hit detector K2.
2. Hit the A detector or the shield.
3. The low discriminator bit is off for a K detector while the high discriminator bit is on.
4. Hit alternating K detectors
5. For He events, the ratio of the energy loss in a D detector to the sum of the losses in its nearest neighbor D detectors is outside the interval specified below:
 
$$0.48 \leq D2/(D1+D3) \leq 0.68$$

$$0.51 \leq D3/(D2+D4) \leq 0.69$$

$$0.29 \leq D4/(D3+D5) \leq 0.39$$

$$0.42 \leq D5/(D4+D6) \leq 0.56$$

The first two conditions, discussed above, account for the overwhelming majority of rejections. The others are readout errors. Conditions 3 and 4 are readout errors which should never occur for actual events. Condition 5 is a requirement suggested by University of Chicago personnel to filter out corner-cutting trajectories. Note that the events rejected by these criteria must nevertheless be included in the total event count  $C_j$  of Eq. (5-4), which is the sum of all the events in the matrix and those that have been rejected.

## 5.5 MARCH, 1991, STORM

Although the rate counters output every 4.096 sec., more time is needed to determine a statistically significant individual nuclear type event count ( $C_i$  in Eq. 5-4), since, at most, two events are pulse-height analyzed per second. Thus, we used 5 minute averages for the total rates  $R_j$  in the priority groups, but longer periods when necessary to obtain fractions  $f_i$  of the nuclear species. This procedure depends on the assumption that these fractions are slowly varying compared to the total priority group rates. This is obviously not true in the belts, where protons are not counted by design, and the middle priority group, which includes He, is overwhelmed by proton pileup. Thus, in Figure 23, we plotted the proton counts in proton mode only (high altitudes), and He for both proton and normal mode, but excluding the belts. The data shown are for the proton event of March, 1991, accompanied by the storm commencing at 0343 on 23 March (indicated by the label SSC in the figure). In the last pass before SSC (orbit 587), the high P2 count rate prevented any pulse height readouts of nuclei (i. e. protons) in the lower priority group P3. Therefore, we couldn't obtain a proton fraction  $f_1$  directly from this orbit, but used instead the average from the previous orbit. The reason why the curve for H for this orbit is smooth compared to those of the other orbits is that we used this same fraction (2.5%) for the entire orbit, while the proton fraction was computed at each point in the other orbits.

Figures 24 and 25 show, in stacked format, the He count rates vs.  $L$  for orbits 575-584. The results include Poisson error bars, assuming that the relative error in the data is  $1/n^{1/2}$ , where  $n$  is the number of He events counted for the data point. In these first 10 orbits, the counts are sparse, with the error bars generally running from twice the plotted values to zero, i. e., most of the nonzero instances arise from one event. Figures 26 and 27 show orbits 585-595. The results for these orbits are close to what had been obtained before. Significant counts begin

# ONR-604 HE-H COMPARISON (52-115 MEV/NUCLEON)

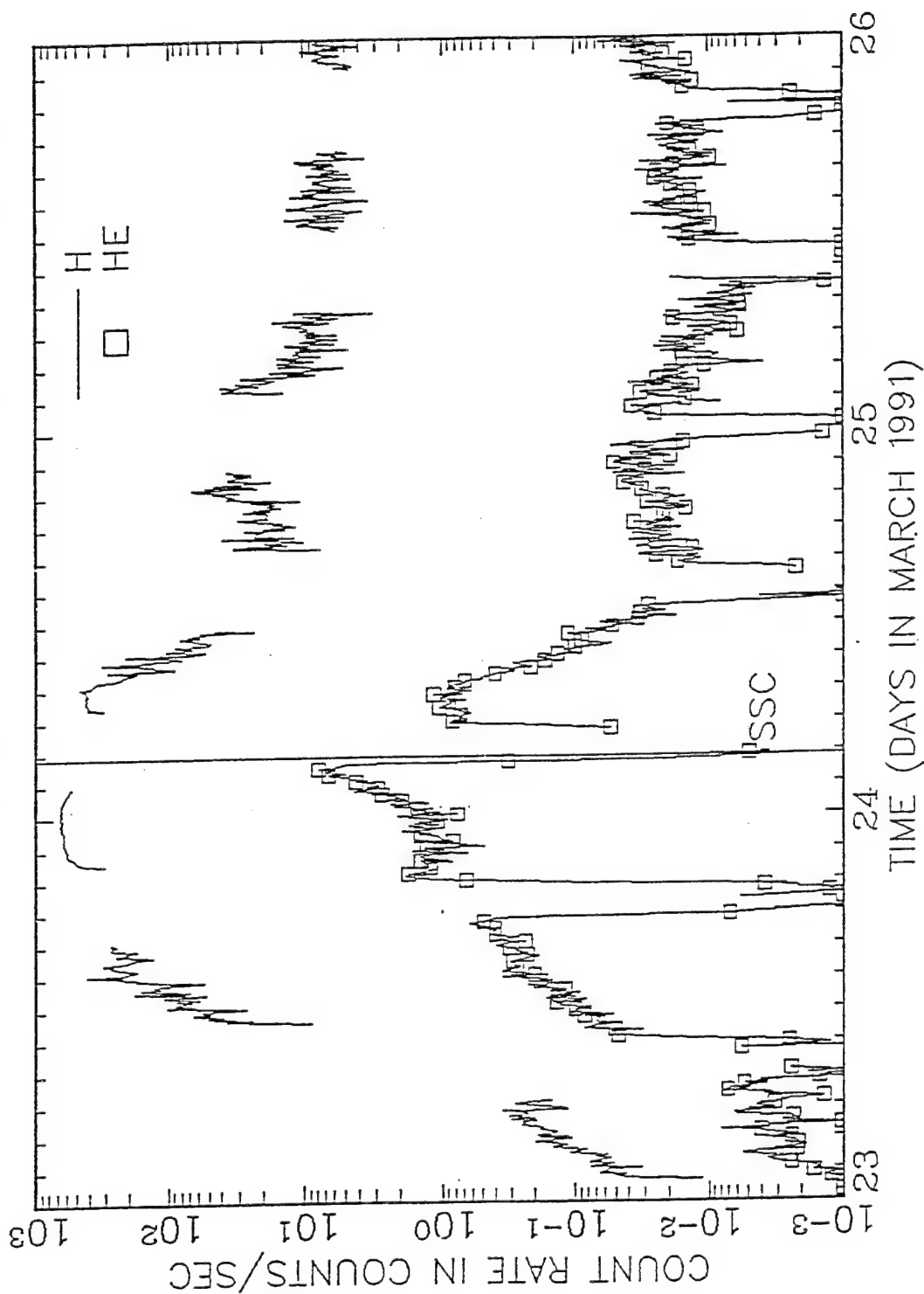
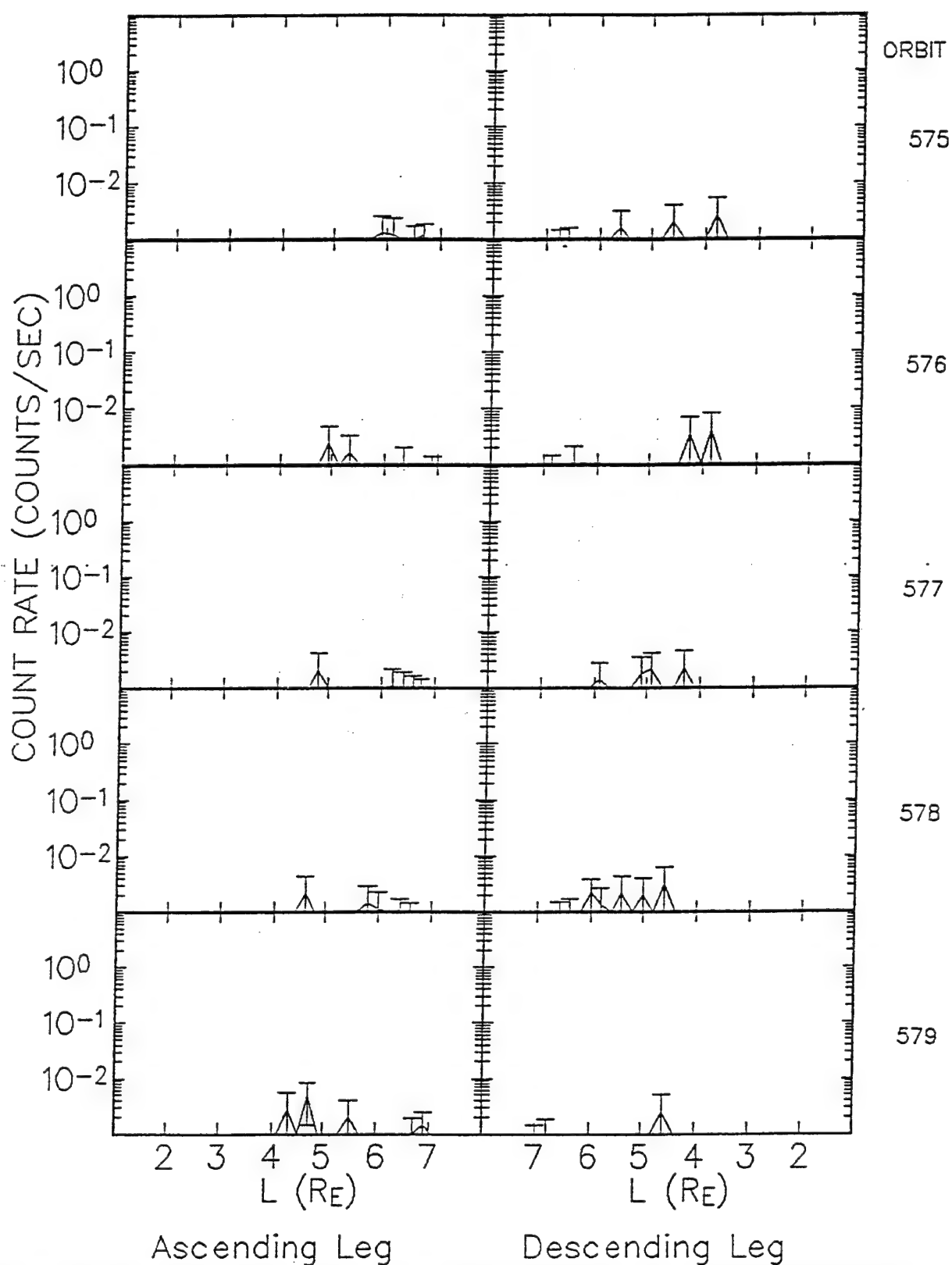


Figure 23. H and He count rates before and after the Sudden Storm Commencement (SSC) of 24 March, 1991.

# Normalized He Count Rate (Counts/sec)



**Figure 24.** Helium count rate as function of L for ascending (left half) and descending (right half) legs of orbits 575-579, with error bars.



# Normalized He Count Rate (Counts/sec)

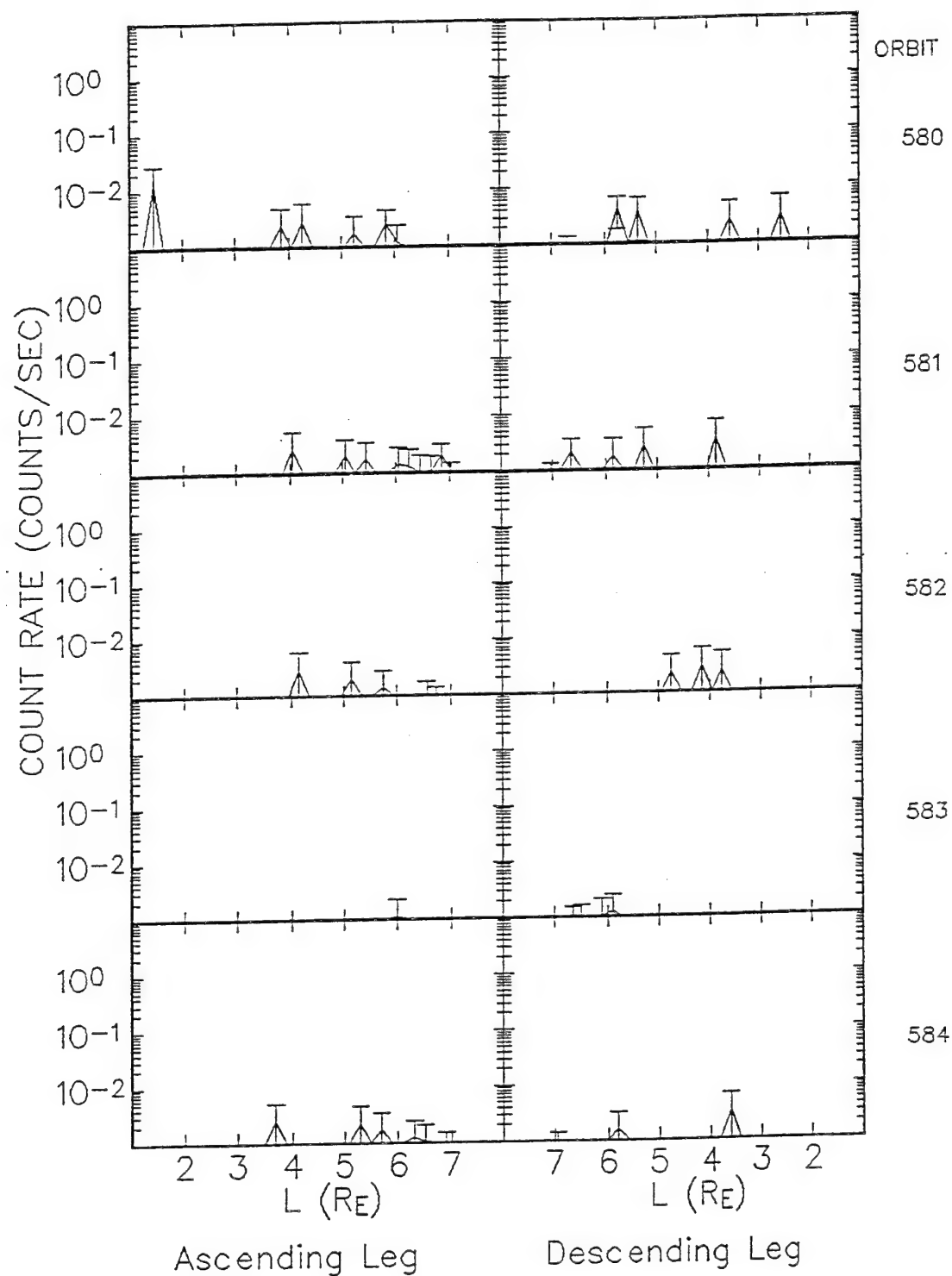


**Figure 25.** Same as Figure 24, except for orbits 580-584.

# Normalized He Count Rate (Counts/sec)

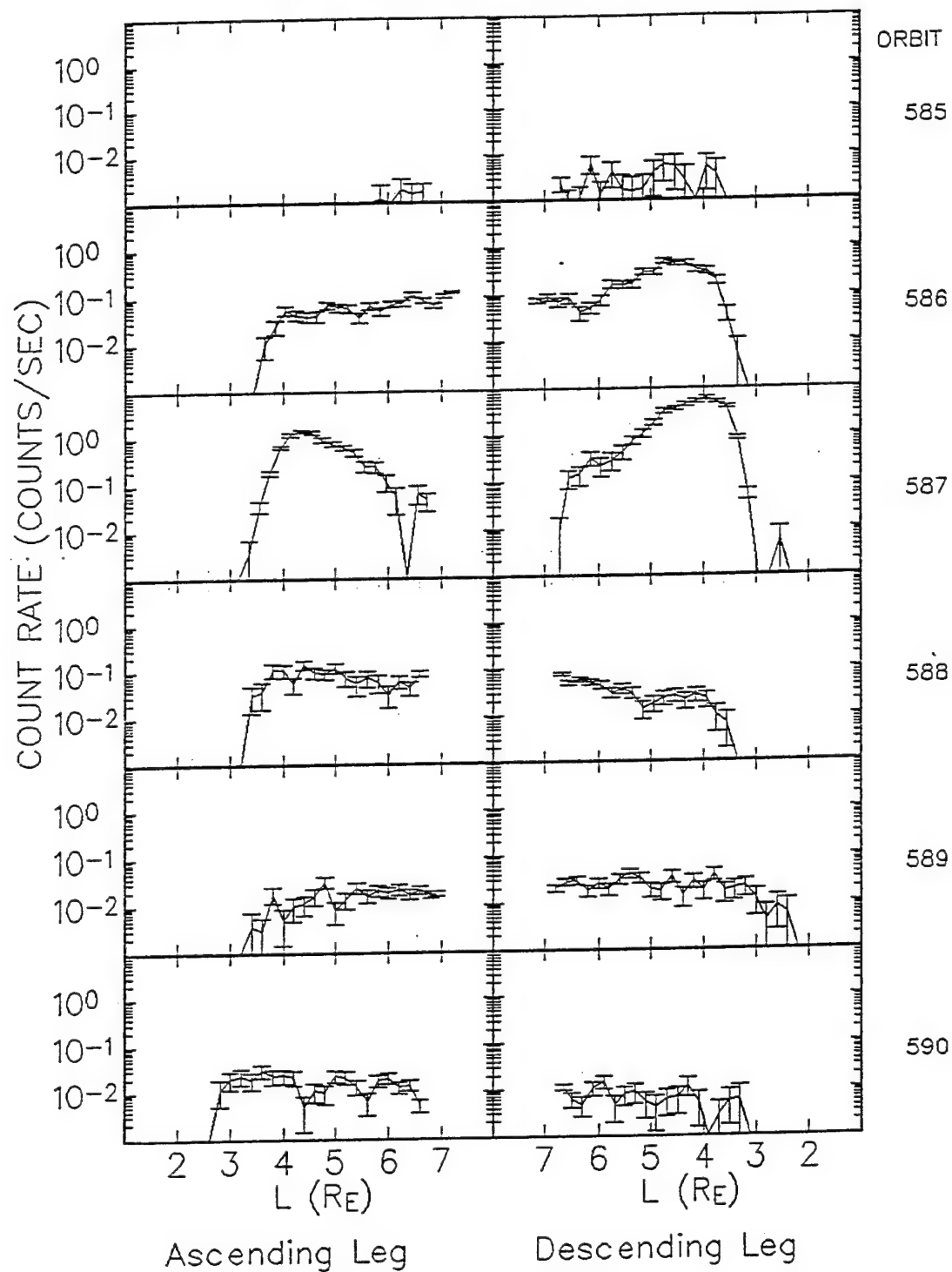


**Figure 26.** Same as Figure 24, except for orbits 585-590.

# Normalized He Count Rate (Counts/sec)

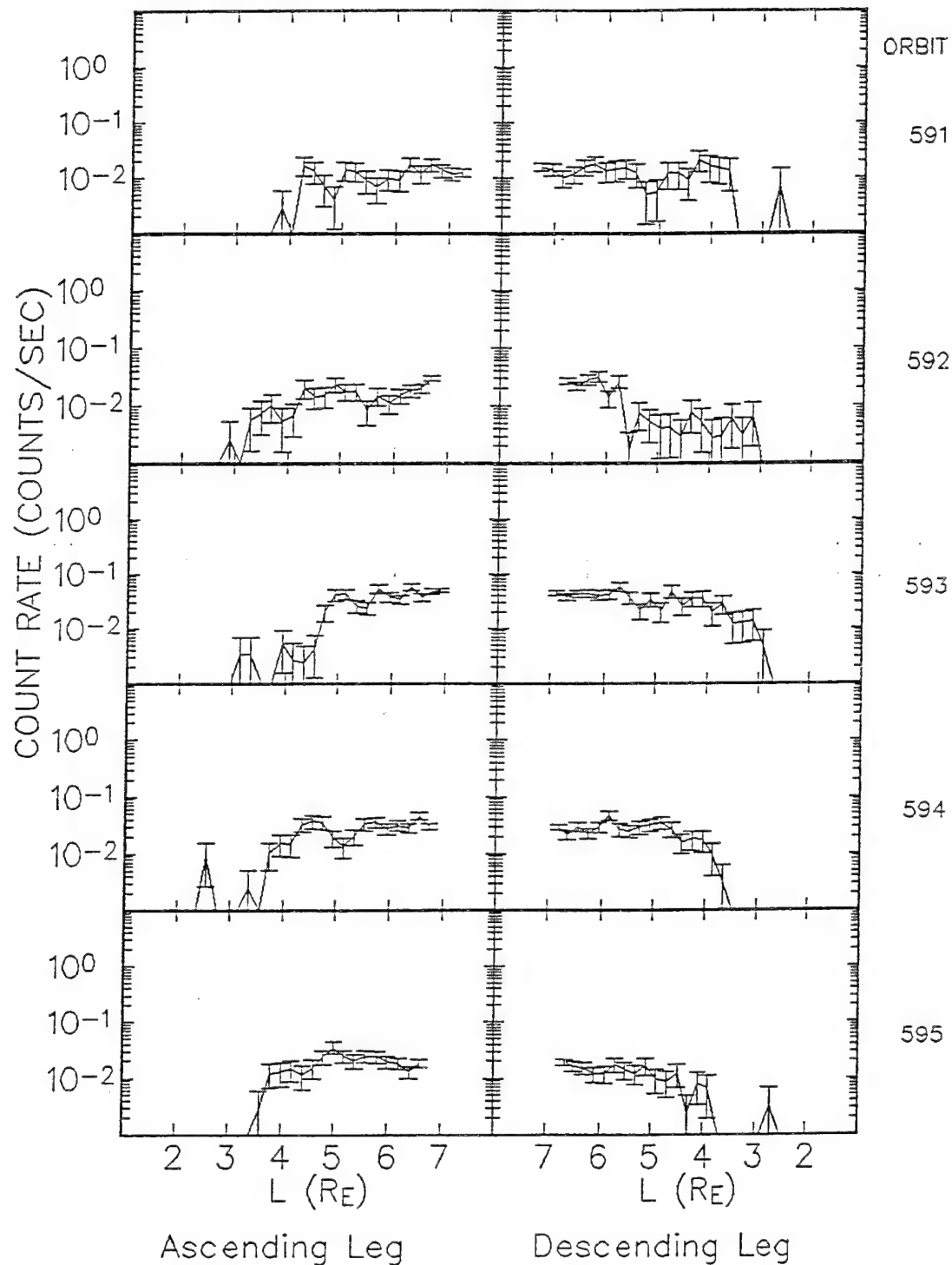


**Figure 27.** Same as Figure 24, except for orbits 591-595.

# Normalized He Count Rate (Counts/sec)

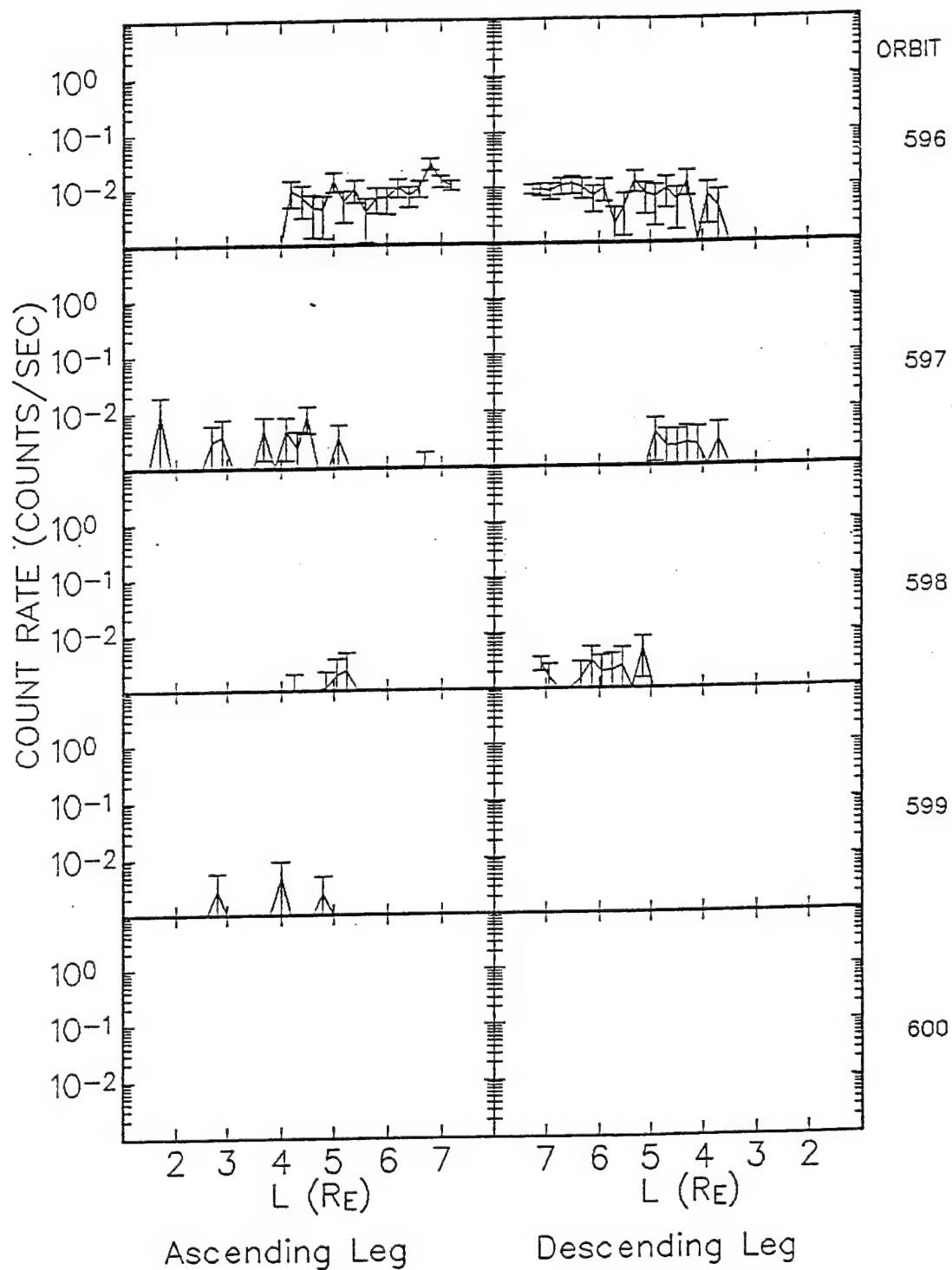


**Figure 28.** Same as Figure 24, except for orbits 596-600.

appearing in orbit 585. By the descending leg of orbit 587, just prior to the SSC at  $L=2.5 R_E$ , a significant radial profile has been built up, with a maximum at  $4 R_E$ , and cutoff at  $3.5 R_E$ . The profile quickly flattens out in subsequent orbits, but counts remain significant at higher  $L$  through orbit 596 (Figure 28). There is some evidence, but not overly convincing, that He penetrates to the region where the new proton belt formed,  $L=2-3 R_E$ , particularly in the descending leg of orbit 589 and the ascending portion of orbit 590. Sparse He counts are seen inside  $L=3$  in each of the next 5 orbits (591-595), and in orbit 587. However, in the last 10 orbits examined (596-605, Figures 28 and 29), all that appear in this region are single counts in orbits 597 and 601. This suggests that, although He may have penetrated during the storm to the region where the new proton belt formed, it did not form a permanent belt.

# Normalized He Count Rate (Counts/sec)

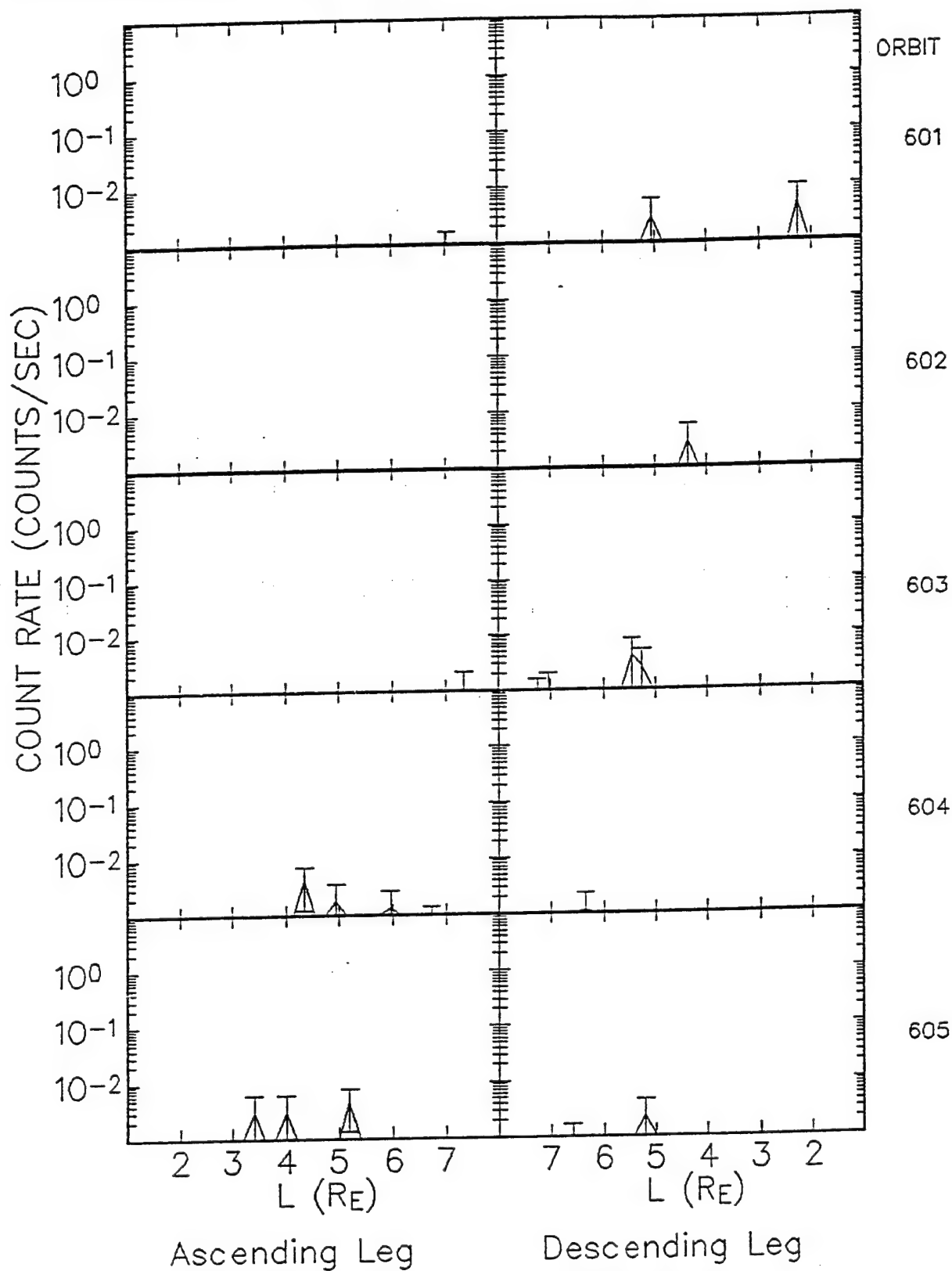


**Figure 29.** Same as Figure 24, except for orbits 601-605.

## 6. PROTON EVENT OBSERVATIONS

A major magnetic storm such as the event commencing at 0342 UT on 24 March, 1991, is often associated with enhancements in solar proton infiltration of the magnetosphere over the preceding 1-2 days. The ability to understand how these protons have access to the inner magnetosphere would be enhanced by simultaneous observations along different locations of possible access routes. The presence of IMP-8 in the solar wind and far tail during the CRRES mission afforded an opportunity for such comparisons. Also present in geosynchronous orbit were the GOES satellites. These satellites possess proton spectrometers measuring in energy ranges comparable to the PROTEL instrument on CRRES. The elliptical orbit of CRRES allows one to estimate the fractional penetration of protons as a function of L, relative to that seen in the far tail or solar wind by IMP-8, or at geosynchronous altitudes by GOES.

Tables 27 and 28 show the IMP-8 and GOES-7 energy channels that were used. The IMP-8 data are from the Charged Particle Measurement Experiment (CPME) (John's Hopkins/Applied Physics Laboratory) and were provided to us by T. Armstrong as 5.5 minute averages. The GOES-7 data (Space Environment Monitor) are provided by NOAA as 5 minute averages. Since the energy channel widths in each case are larger than those on PROTEL, an average PROTEL-measured flux over each energy channel of the other two instruments was estimated by integrating a power law fit of the measurements over appropriate PROTEL channels, and dividing by the IMP-8 or GOES-7 channel width:

$$F = \frac{\int_{E_1}^{E_2} f(E) dE}{E_2 - E_1} \quad (6-1)$$

where  $f(E)$  is the power law differential flux at energy  $E$ ,  $\alpha E^\beta$ , and  $E_1$  and  $E_2$  are the lower and upper energy limits of the IMP-8 or GOES-7 channel with which the PROTEL data is to be compared.

The PROTEL energy channels used for each IMP-8 and GOES-7 channel are given in Tables 27 and 28. The energy assigned to each PROTEL channel for this purpose was the average energy of the channel's response function, as determined by calibrations (Table 29). To define the PROTEL data as a function of L the PL (Phillips Laboratory) L-binned data base was used. This data base provides, for each  $1/20 R_E$  wide L bin, averaged measured fluxes in 19 pitch angle bins that are  $5^\circ$  wide, except at the loss cone, where the bin is  $2.5^\circ$  wide. Also given for each pitch angle bin is the number of observations. This allowed us to compute the average flux over the entire pitch angle range for each L-bin, essentially a time-averaged flux for comparison with the other instruments.

TABLE 27. PROTEL and IMP-8 (CPME) Channels		
IMP-8 Channel	Energy Range (MeV)	PROTEL Channels
P4	2.0 - 4.6	3,5,6
P5	4.6 - 15	6-15
P7	15 - 25	13-17
P8	25 - 48	16-22
P9	48 - 96	21-24

TABLE 28. PROTEL and GOES-7 Channels		
GOES-7 Channel	Energy Range (MeV)	PROTEL Channels
P1	0.6 - 4.2	3,5,6
P2	4.2 - 8.7	5-7, 11
P3	8.7 - 14.5	7,11,12,13,15
P4	15 - 44	13, 15-21
P5	38 - 82	19-24

TABLE 29. PROTEL Energy Channels		
Channel Number	Energy Range (MeV)	Average Energy (MeV)
1	1.0 - 2.1	1.5
2	2.0 - 2.3	2.1
3	2.2 - 2.8	2.5
4	2.8 - 3.2	2.9
5	3.2 - 4.1	3.6
6	3.9 - 4.8	4.3
7	4.6 - 7.0	5.7
8	7.3 - 9.4	8.4
9	6.0 - 7.7	6.8
10	7.5 - 9.6	8.5
11	9.3 - 10.2	10.7
12	9.9 - 11.5	13.2
13	11.2 - 15.2	13.2
14	14.7 - 15.9	15.2
15	15.5 - 18.3	16.9
16	18.0 - 20.8	19.4
17	25.3 - 27.2	26.3
18	26.1 - 35.6	30.9
19	34.9 - 37.7	36.3
20	37.8 - 48.1	42.3
21	44.3 - 53.5	47.5
22	53.5 - 62.1	57.0
23	62.1 - 73.1	67.5
24	73.1 - 100.0	82.9



Figures 30 and 31 compare the proton fluxes observed by PROTEL and IMP-8 in the energy ranges 4.6-15 MeV and 48-96 MeV, respectively, before and after the sudden storm commencement (SSC), which is marked by the arrow above the data in the upper center portion of the figures. The SSC was marked by sudden increases in the readings of both ground-based and space-based magnetometers (not shown here). An increase in the proton population at the IMP-8 position, which is in the magnetotail at  $\sim 30 R_E$ , is seen at  $\sim 20$  hours before the sudden commencement. In the lower energy range shown, they are not seen by PROTEL until CRRES crosses the  $L=6$  shell, when the fluxes measured by the two are nearly equal. In the higher energy range, PROTEL sees the protons at  $L=5$ . In general, the higher energy protons are seen by PROTEL to lower  $L$  shells. In the first upleg pass (orbit 588) after the sudden commencement PROTEL sees at all  $L > 4$  fluxes much higher than those seen by IMP-8. This suggests that there was a magnetospheric process, presumably particle acceleration due to the magnetopause compression at the SSC, which affected the solar protons that had reached the inner magnetosphere, but not those in the far magnetotail. Theoretical modeling of this acceleration is discussed in another section of this report. In the subsequent downward leg of the same orbit, and in the upward pass of the next orbit (in the middle of day 83), the particle fluxes observed by PROTEL in the lower energy range agree with those seen by IMP-8, except below  $L=5$  in the downward leg, and  $L=5.5$  in the subsequent upward leg. Finally, there is a small increase in the magnetotail (IMP-8) proton flux which is seen by PROTEL at all  $L$ -values shown. The higher energy protons behave about the same, except that, as before the SSC, they penetrate to lower  $L$ .

Figures 32 and 33 show, for  $L=4$  and 5 respectively, the ratios of the PROTEL-measured flux at the specified  $L$  to the flux measured by GOES-7 in the specified energy ranges. Also shown, for reference, is the flux measured by GOES-7 in the 4.2 - 8.7 MeV energy range. The SSC is associated with the steep rise in the GOES-7 flux at  $\sim 4$  hr UT on day 83. The lowest GOES-7 energy range, 0.6 - 4.2 MeV is not shown because the fluxes at  $L=4$  even before the SSC were higher than the GOES-7 fluxes both before and after the SSC, indicating that there was a previously trapped population in this energy range. For the other energies, if we interpret the ratio of flux at the specified  $L$  to the GOES-7 flux as a percent of particles penetrating to that  $L$ , we find that before the SSC at  $L=4$ , the penetration was less than 1% at all energies, while at  $L=5$ , it was less than 50%. The penetration is monotonically increasing with energy, except at  $L=4$ , where the lowest energy range apparently achieves the second highest penetration percentage, which may be due to the statistical error associated with low counts. After the SSC the penetration percentage is considerably higher, rising to near 100% at  $L=5$  at the highest energies, a level also achieved immediately after the SSC at both  $L=4$  and  $L=5$  at all energies. This again suggests a magnetospheric process, associated with the SSC, which may have accelerated the particles already in the magnetosphere and transported them inward. The continued high flux levels, with energy-dependent penetration, for up to  $\sim 1$  day after the SSC may be due to changes in the magnetospheric state caused by the SSC, permitting greater penetration. There is possibly a small compression near the end of day 83, increasing the flux levels both at geosynchronous and lower altitudes. At this time, the penetration percentage is uniformly high at all the energies, before falling later in day 84, most dramatically at lower energies. At the highest energy the penetration remains above 10% at  $L=4$  during the period shown, and above 50% at  $L=5$ .

PROTEL-IMP8 COMPARISON (4.60 - 15.0 MEV PROTONS)  
DIFFERENTIAL FLUX (PART/CM\*\*2/SR/MEV/SEC)

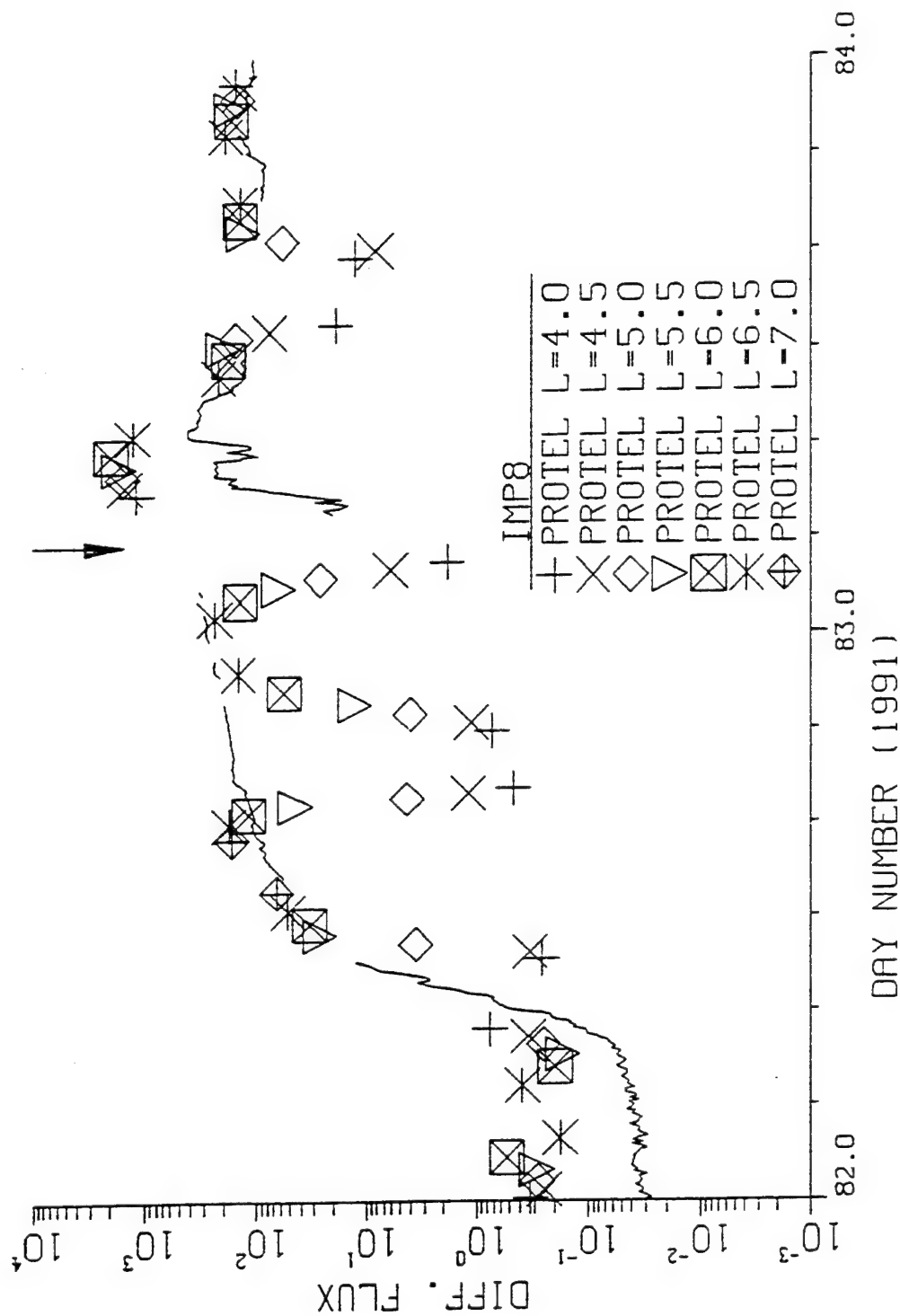


Figure 30. Comparison of 4.6-15 MeV proton mean differential fluxes measured by PROTEL and IMP-8 during March 24-25, 1991.

PROTEL-IMP8 COMPARISON (48 - 96 MEV PROTONS)  
DIFFERENTIAL FLUX (PART/CM\*2/SR/MEV/SEC)

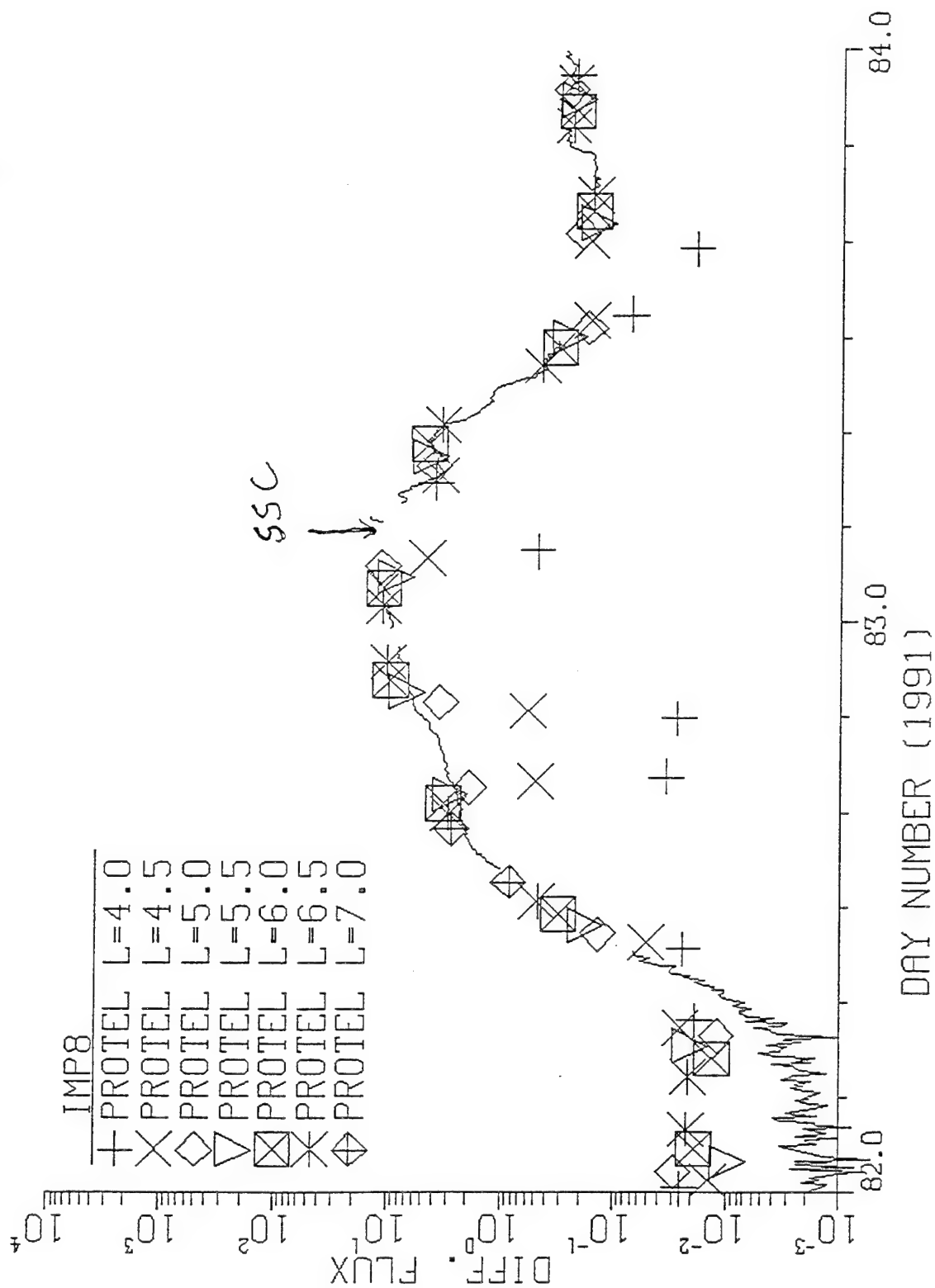


Figure 31. Same as Figure 30, except at the energy range 48-96 MeV.

# PROTEL-GOES Comparison L = 4

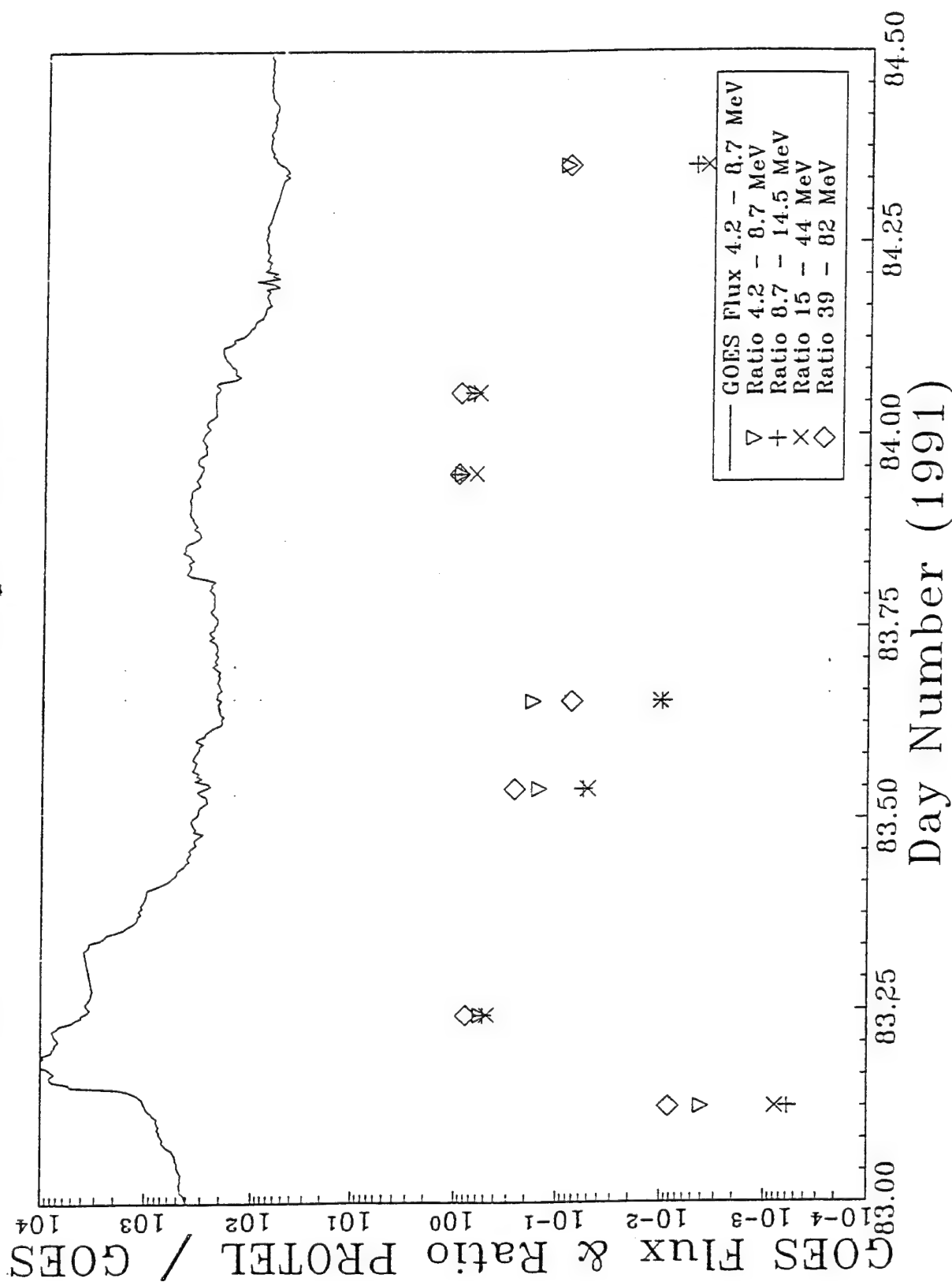


Figure 32. Ratios of PROTEL-measured mean differential fluxes at L=4 in various energy ranges to those measured by GOES-7 in same energy ranges during March 24-25, 1991.

# PROTEL-GOES Comparison L = 5

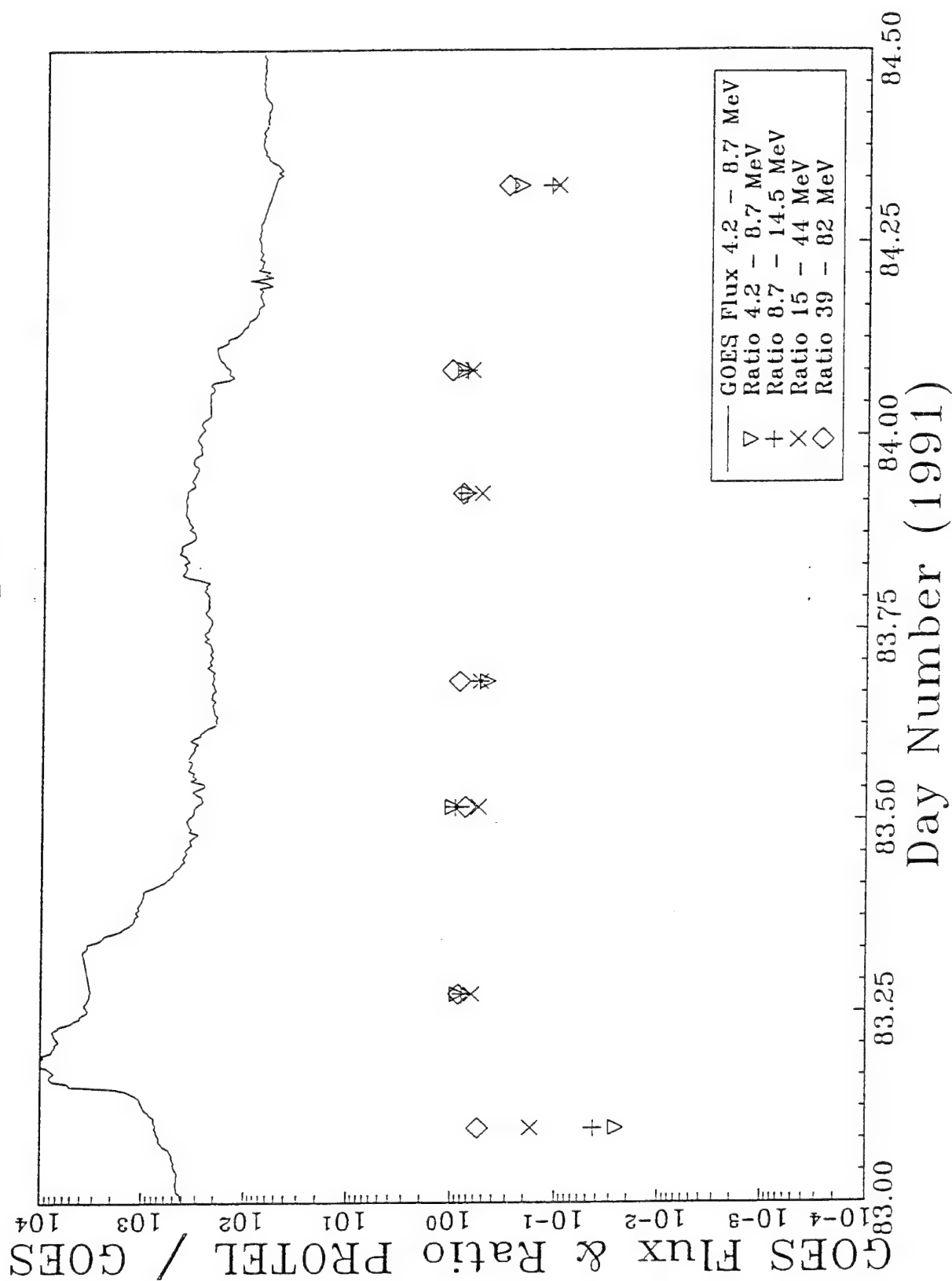


Figure 33. Same as Figure 32, except for L=5.

## 7. CRRES INSTRUMENT MODELING: PROTEL

### 7.1 PROTEL CONTAMINATION CODE

The Proton Telescope (PROTEL) is one of several CRRES instruments used to measure proton energy and flux. Instruments of different types were used to obtain data over a wide energy range, and to provide redundancy where there was an overlap. PROTEL collected proton flux data in the 1 to 100 MeV energy range in the radiation belts. It consisted of two detector instruments, the Low Energy Head (LEH) (1-10 MeV) and the High Energy Head (HEH) (6-100 MeV), and a dedicated processor which processed the raw data, and at 1 second intervals, handed off the reduced data to the satellite's telemetry system. The reduced data consists of counts in 24 energy channels (8 for LEH, 16 for HEH) spaced logarithmically in the 1-100 MeV energy interval, together with environmental data and raw counts for each of the solid state particle detectors.

The PROTEL instrument operated in a hostile environment, where it was subjected to a high density flux of electrons, protons and, to a lesser extent, heavier ions, particularly while passing through the radiation (Van Allen) belts. In addition to using passive shielding techniques and magnetic deflection of electrons, both the LEH and HEH used a technique which is sometimes called "active" shielding. Each head had an array of disk shaped silicon particle detectors, many of which had a second (ring shaped) active detection region. The energy deposited by a charged particle in each of the solid state detector's active regions was measured by pulse height analysis, and the on-board processor used coincidence and anti-coincidence in the detector array (detection logic) to reduce false counts by excluding counts which resulted from protons entering outside the nominal acceptance cone, which entered from the rear, or did not deposit the correct energies corresponding to the proton energy channels.

In order to compare PROTEL data with data obtained from other CRRES instruments, it was necessary to model its behavior. In the radiation belts, it was expected that the flux detected by the LEH would be too high as a result of false counts (contamination) resulting from the penetration of high energy protons (above 100 MeV) from angles outside the entrance cone. In an earlier report [Redus, *et al.*, 1990], it was suggested that the HEH would also have significant problems resulting from contamination. The effect of contamination on observed counts strongly depends upon the energy spectrum and the angular distribution of the high energy protons.

The PROTEL Contamination Code, a software package which models the contamination problem for the HEH, was developed by Radex. The results provided here indicate that for certain "hard" proton spectra, particularly in the range between 100 and 350 MeV, the PROTEL HEH would be subjected to a high level of "contamination". The results obtained from this study (response functions) have been used to compare PROTEL data with data obtained from the CRRES dosimeters, and corrections obtained from the PROTEL modeling described here for the isotropic case have been successfully applied to the CRRES dosimeter data and to data obtained from other satellite instruments [Violet, 1992].

A detailed description of the PROTEL instrument is provided in a recent report [Lynch, *et al.*, 1989]. The PROTEL HEH detector contains six solid state detectors D1-D6. D1-D5 each contain two detection areas, a central disk, and a ring surrounding the disk. D6 has only a circular disk. Pulse height circuitry, coincidence and anti-coincidence circuitry, and logic are used to classify detection events in the several particle detectors. A detection event is recorded in one of the energy channels only if it meets the energy deposit requirements of the detectors associated with the energy channel and the requirements of the coincidence/anticoincidence logic. The ring detectors and D6 are used in connection with the anti-coincidence logic. The anti-coincidence logic is used to reduce or eliminate counts due to protons which enter through the back or enter the detector from directions outside the nominal acceptance cone.

The geometry of the HEH is provided in Figure 34. The materials used for the passive shielding and in the construction of the HEH are indicated by shading.

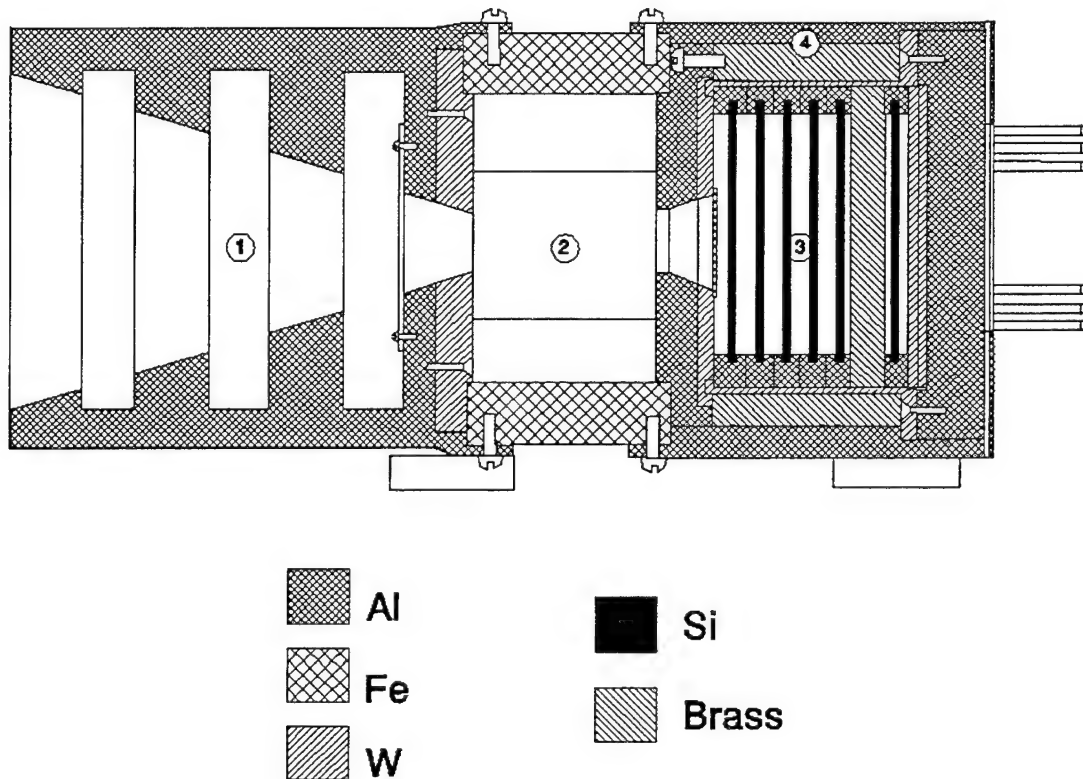


**Figure 34.** Protel HEH Cross Section (Not to Scale). (1) baffle, which defines the nominal entry cone. (2) electron magnetic deflection housing. (3) detector housing. (4) shielding for the detector array.

### 7.1.1 Description of the PROTEL Contamination Code

The assumptions made in developing the PROTEL contamination code are as follows:

The primary effect is due to protons which penetrate the PROTEL housing/shielding and are decelerated in the direction of motion while interacting with the electrons in the material through which they pass. The protons are assumed to travel in straight lines until they either are stopped by or penetrate the material they are passing through. This is a relatively good assumption for high energy protons. However, important effects are neglected, such as Coulomb scattering with the nuclei, inelastic scattering off of the nuclei, including "STARS" -- nuclear reactions which produce protons, neutrons, and/or gamma rays.

Under this assumption, the computation of contamination effects proceeds as follows:

(1) A simplified mathematical description of the mass/geometry of the HEH was developed using the original blueprints. From the latter, measurements were made of the different materials used in the construction of the HEH and their locations. The materials used were aluminum, iron, brass, and tungsten. In addition, a magnet was used to deflect high energy electrons. The magnet was made of samarium and cobalt. From the blueprint diagrams of the magnet, it was not possible to determine the location of the actual boundary between the iron magnet holder and the magnet pieces. Partly for this reason, and partly to simplify the computations, it was decided to treat the entire magnet as iron.

(2) A ray tracing algorithm was developed which would determine the number of layers, compute the thickness of each layer, and identify the materials which a ray pointing in an arbitrary direction (starting from an arbitrary point within the detector volume) would encounter. Except for the case in which the path intersects the ridges on the inside surface of the PROTEL HEH baffle, the computed thicknesses are accurate to approximately 0.1 mm, which is better than the estimated 0.5 mm accuracy to which the dimensions of the various components of the PROTEL housing/shielding can be measured from the blueprints. Using the Janni energy-range relations and the Janni tables [Janni, 1982], a fast algorithm was developed which would, given a proton input spectrum, compute the spectrum resulting from passage through the materials associated with a given point and direction.

As a test of the methodology, calibration tests of the PROTEL HEH performed at the Harvard University cyclotron were successfully modeled using an early version of the PROTEL Contamination Code [Hein, 1990].

(3) A Monte Carlo code was used to model the behavior of the High Energy Head. For each Monte Carlo trial, a point on the surface of the first detector was randomly selected. Then a direction (unit vector) was randomly selected (based upon the proton pitch angle distribution - isotropic, mirror plane, or  $\sin^N \alpha$ ). For each such point and direction, the ray-tracing routine was used to compute the thickness of each of the material "layers" through which a proton passes in the body and shielding of PROTEL in its path to each reference point on the first



detector.

(4) The ray-tracing algorithm has a high computation overhead. For this reason, and the fact that the contamination computation will be repeated for various input spectrum and values of input parameters, it was necessary to generate a file containing the ray trace output data for each of the Monte Carlo "trials". The number  $N$  of "trials" required was determined by comparing runs performed with different "seeds";  $N = 20,000$  points was chosen over a solid angle defined by a 60 degree half-angle. For larger half angles, the fraction of protons which would strike more than one detector was small. The file contains the following information for each of the 20,000 reference points and reference directions:

- (a) The location of the reference point on the first detector.
- (b) The unit vector describing the direction of the ray.
- (c) The number of "layers" of material the ray passes through
- (d) For each layer, a matter flag which indicates what material the ray passes through (aluminum, iron, brass, tungsten, etc.)
- (e) The thickness of each layer.

(5) A variety of input spectra would be studied, thus, the *response function* which describes the instrument's response to a flat energy spectrum as a function of energy was computed. For incident energies in the range of 5-105 MeV, the response function was computed at energy intervals of 0.1 MeV; from 105-400 MeV at 1 MeV intervals. The direction and thickness information in the file described above is used to compute the energy loss in each of the material layers using the Janni energy/range relation for each of the materials. For each trial in which the particle actually reaches the first detector, a determination is made, as to which detectors the ray passes through; then the path length through the detector is calculated, and the detector coincidence logic is used to determine the channel into which the corresponding "count" is to be recorded. For each of the incident energies, the fraction of counts detected is compared to the total number of trials.

(6) The tabulated response function is then used to compute the actual number of predicted counts for an arbitrary energy spectrum.

### 7.1.2 Results

A detailed description of the methodology and of the results of the PROTEL Contamination Code computations has already been published [Hein, 1993]. A brief summary of the results is provided below.

Tables 30-32 give the fraction of PROTEL HEH counts due to contamination for proton energy spectra of the form  $E^q$  where  $E$  is in MeV and  $q$  varies in 0.5 steps from 0 to -6 for an isotropic distribution. Table 30 gives the contamination due to protons of all energies. Tables 31 and 32 give the fraction of the PROTEL HEH counts due to contamination from protons above 100 and 200 MeV, respectively. Tables 33 and 34 provide the data which corresponds to the first

data set of Table 30 for the mirror plane case, for an orientation of the mirror plane of 0 and 90 degrees, with respect to the direction of the maximum obstruction of the electron deflection magnet.

The tables are obtained from integrating the product of the computed response function with the indicated power law spectrum over the total energy range for Tables 30, 33, and 34, and over the ranges  $E > 100$  MeV and  $E > 200$  MeV for Tables 31 and 32. The differences in the entries in Tables 30 and 31 reflect the contamination contribution for the range  $0 < E < 100$ ; similarly for Tables 30 and 32 ( $0 < E < 200$ ) and Tables 31 and 32 ( $100 < E < 200$ ).

Response functions for some of the HEH channels are provided in graphical form in Figures 35 and 36 for the isotropic case, and Figures 37 and 38 for the two mirror plane orientations. For the latter, the two response functions are provided in each graph. The non-contamination response of each detector is represented by a "spike" in the  $0 < E < 100$  MeV range, with the spike "width" being the actual channel width. The bulk of the contamination occurs in the  $E > 100$  range, as is evident in the graphs. On Figures 37 and 38, solid vs. dashed lines are used to mark each of the response functions at occasional values.

The response function for the isotropic case was used to cross calibrate PROTEL data with data obtained from the CRRES dosimeters and other instruments. The data, associated with solar proton events, covered 20 orbits in March and June of 1991. The data was collected at high altitudes and was known to be near-isotropic; the energy spectra appeared to be relatively flat and stable over periods of several hours. This study [Violet, 1992] also compared the same PROTEL data with data obtained from the GEOS satellite. In this study, the PROTEL data was fitted to a power law spectrum of the form  $(J(10 \text{ MeV})/J(E))^N$ . The response function was used to compute corrected values of  $J(10)$  and  $N$ . The latter were compared, with good agreement to similar fits of data obtained from the CRRES dosimeter and the GEOS detectors [Gussenhoven, *et al.*, 1993]. The corrections were found to be substantial, and increase for power law spectra as  $N$  approaches 0.

TABLE 30.  
FRACTION OF PROTEL HEH COUNTS DUE TO CONTAMINATION  
Isotropic Distribution  
POWER LAW SPECTRUM E\*\*q

CHAN	q = 0	-.5	-1.0	-1.5	-2.0	-2.5	-3.0	-3.5	-4.0	-4.5	-5.0	-5.5	-6.0
1	.9928	.9606	.8153	.4671	.1882	.0950	.0687	.0581	.0513	.0460	.0416	.0377	.0343
2	.9833	.9210	.7056	.3537	.1421	.0739	.0526	.0433	.0373	.0327	.0289	.0255	.0227
3	.9659	.8616	.6045	.3344	.2086	.1660	.1491	.1396	.1326	.1268	.1217	.1171	.1129
4	.9642	.8607	.5986	.2906	.1293	.0729	.0526	.0430	.0371	.0326	.0290	.0260	.0234
5	.9768	.9152	.7416	.4557	.2313	.1313	.0943	.0791	.0712	.0662	.0626	.0599	.0579
6	.9736	.9119	.7556	.5167	.3267	.2338	.1949	.1767	.1660	.1584	.1522	.1468	.1421
7	.9721	.9103	.7543	.5002	.2746	.1539	.1018	.0786	.0663	.0583	.0523	.0475	.0434
8	.9817	.9459	.8535	.6673	.4246	.2340	.1314	.0839	.0613	.0489	.0412	.0356	.0314
9	.9762	.9370	.8474	.6868	.4882	.3256	.2274	.1753	.1472	.1304	.1190	.1104	.1034
10	.9828	.9573	.8993	.7846	.6071	.4114	.2582	.1643	.1125	.0837	.0666	.0553	.0471
11	.9739	.9406	.8733	.7573	.5996	.4388	.3129	.2303	.1800	.1492	.1292	.1153	.1048
12	.9835	.9643	.9255	.8537	.7379	.5855	.4283	.2995	.2101	.1532	.1175	.0944	.0786
13	.9770	.9543	.9127	.8430	.7403	.6128	.4818	.3689	.2837	.2241	.1835	.1554	.1353
14	.9852	.9717	.9473	.9052	.8381	.7423	.6240	.5000	.3888	.3008	.2366	.1914	.1596
15	.9872	.9770	.9594	.9299	.8830	.8137	.7207	.6102	.4952	.3897	.3028	.2362	.1874
16	.9884	.9807	.9682	.9485	.9182	.8735	.8113	.7306	.6346	.5310	.4297	.3391	.2636

TABLE 31.  
FRACTION OF PROTEL HEH COUNTS DUE TO CONTAMINATION  
due to protons with E > 100 MeV  
Isotropic Distribution  
POWER LAW SPECTRUM E\*\*q

CHAN	q = 0	-.5	-1.0	-1.5	-2.0	-2.5	-3.0	-3.5	-4.0	-4.5	-5.0	-5.5	-6.0
1	.9893	.9503	.7849	.4031	.1104	.0224	.0042	.0008	.0001	.0000	.0000	.0000	.0000
2	.9765	.9039	.6655	.2909	.0775	.0169	.0035	.0007	.0002	.0000	.0000	.0000	.0000
3	.9458	.8088	.4919	.1783	.0462	.0107	.0025	.0006	.0001	.0000	.0000	.0000	.0000
4	.9494	.8282	.5395	.2178	.0617	.0153	.0037	.0009	.0002	.0001	.0000	.0000	.0000
5	.9650	.8887	.6867	.3699	.1348	.0396	.0109	.0029	.0008	.0002	.0001	.0000	.0000
6	.9546	.8674	.6615	.3638	.1426	.0462	.0140	.0042	.0013	.0004	.0001	.0000	.0000
7	.9570	.8794	.6960	.4132	.1769	.0615	.0197	.0062	.0019	.0006	.0002	.0001	.0000
8	.9718	.9265	.8169	.6072	.3463	.1532	.0582	.0207	.0073	.0025	.0009	.0003	.0001
9	.9595	.9041	.7859	.5855	.3513	.1721	.0742	.0302	.0121	.0048	.0020	.0008	.0003
10	.9727	.9388	.8662	.7299	.5286	.3171	.1615	.0742	.0325	.0140	.0060	.0026	.0011
11	.9563	.9087	.8184	.6707	.4800	.2961	.1620	.0823	.0404	.0197	.0096	.0047	.0023
12	.9735	.9470	.8962	.8064	.6676	.4925	.3202	.1870	.1017	.0533	.0275	.0142	.0073
13	.9626	.9300	.8730	.7814	.6518	.4972	.3454	.2217	.1347	.0794	.0462	.0268	.0157
14	.9770	.9581	.9249	.8695	.7840	.6657	.5242	.3810	.2580	.1659	.1034	.0635	.0389
15	.9823	.9691	.9467	.9101	.8531	.7706	.6621	.5360	.4079	.2939	.2032	.1370	.0913
16	.9884	.9806	.9682	.9485	.9182	.8735	.8112	.7304	.6344	.5308	.4295	.3387	.2631

TABLE 32.  
FRACTION OF PROTEL HEH COUNTS DUE TO CONTAMINATION  
due to protons with E > 200 MeV  
Isotropic Distribution  
POWER LAW SPECTRUM E\*\*q

CHAN	q = 0	-.5	-1.0	-1.5	-2.0	-2.5	-3.0	-3.5	-4.0	-4.5	-5.0	-5.5	-6.0
1	.3742	.3256	.2417	.1105	.0267	.0047	.0008	.0001	.0000	.0000	.0000	.0000	.0000
2	.3436	.2897	.1931	.0759	.0181	.0035	.0006	.0001	.0000	.0000	.0000	.0000	.0000
3	.4039	.3141	.1724	.0559	.0129	.0026	.0005	.0001	.0000	.0000	.0000	.0000	.0000
4	.4096	.3271	.1938	.0706	.0179	.0040	.0008	.0002	.0000	.0000	.0000	.0000	.0000
5	.4049	.3421	.2412	.1178	.0386	.0102	.0025	.0006	.0001	.0000	.0000	.0000	.0000
6	.4076	.3382	.2339	.1158	.0405	.0116	.0031	.0008	.0002	.0001	.0000	.0000	.0000
7	.4225	.3561	.2569	.1381	.0531	.0165	.0047	.0013	.0003	.0001	.0000	.0000	.0000
8	.4673	.4155	.3400	.2332	.1221	.0492	.0169	.0054	.0017	.0005	.0002	.0000	.0000
9	.4590	.3980	.3163	.2139	.1156	.0506	.0193	.0069	.0024	.0008	.0003	.0001	.0000
10	.5276	.4797	.4152	.3266	.2196	.1215	.0566	.0236	.0093	.0036	.0014	.0005	.0002
11	.5568	.4910	.4070	.3043	.1967	.1085	.0525	.0233	.0099	.0041	.0017	.0007	.0003
12	.7133	.6662	.6023	.5148	.4023	.2781	.1680	.0903	.0448	.0211	.0097	.0044	.0020
13	.7408	.6830	.6075	.5111	.3972	.2794	.1771	.1025	.0555	.0287	.0145	.0072	.0036
14	.8093	.7683	.7144	.6432	.5515	.4418	.3253	.2189	.1356	.0788	.0438	.0237	.0125
15	.8470	.8136	.7703	.7138	.6409	.5504	.4458	.3369	.2366	.1553	.0965	.0576	.0334
16	.9013	.8766	.8447	.8033	.7499	.6826	.6006	.5063	.4060	.3085	.2224	.1531	.1014

TABLE 33.  
FRACTION OF PROTEL NEH COUNTS DUE TO CONTAMINATION  
MIRROR PLANE LIMIT, Azimuth = 0 degrees  
POWER LAW SPECTRUM E\*\*q

CHAN	q = 0	-0.5	-1.0	-1.5	-2.0	-2.5	-3.0	-3.5	-4.0	-4.5	-5.0	-5.5	-6.0
1	.9867	.9245	.6768	.2874	.1022	.0560	.0436	.0382	.0345	.0316	.0290	.0268	.0247
2	.9608	.8377	.5352	.2252	.0872	.0446	.0308	.0248	.0213	.0187	.0166	.0148	.0133
3	.8197	.5192	.2596	.1544	.1196	.1057	.0980	.0928	.0887	.0853	.0823	.0796	.0772
4	.8146	.5089	.2194	.0897	.0458	.0296	.0219	.0174	.0143	.0121	.0104	.0091	.0080
5	.9201	.7522	.4642	.2273	.1186	.0784	.0627	.0554	.0513	.0488	.0472	.0462	.0457
6	.8602	.6428	.3864	.2287	.1605	.1315	.1170	.1082	.1019	.0969	.0929	.0895	.0864
7	.8407	.6098	.3433	.1765	.1016	.0689	.0525	.0427	.0360	.0310	.0271	.0239	.0213
8	.9108	.7695	.5369	.3098	.1710	.1044	.0733	.0571	.0475	.0410	.0363	.0328	.0301
9	.8697	.7089	.4962	.3184	.2120	.1561	.1258	.1075	.0950	.0857	.0782	.0721	.0668
10	.8986	.7751	.5865	.3897	.2456	.1608	.1141	.0873	.0705	.0588	.0500	.0431	.0374
11	.8696	.7394	.5655	.3990	.2781	.2029	.1579	.1299	.1112	.0977	.0872	.0789	.0719
12	.9030	.8057	.6589	.4897	.3417	.2368	.1704	.1293	.1030	.0851	.0721	.0621	.0542
13	.8904	.7981	.6692	.5256	.3973	.3005	.2341	.1897	.1596	.1382	.1223	.1099	.0999
14	.9153	.8453	.7410	.6107	.4771	.3628	.2769	.2168	.1756	.1469	.1261	.1105	.0983
15	.9239	.8668	.7814	.6696	.5445	.4252	.3260	.2508	.1966	.1582	.1306	.1104	.0951
16	.9288	.8841	.8190	.7321	.6278	.5167	.4113	.3207	.2482	.1929	.1517	.1211	.0982

TABLE 34.  
FRACTION OF PROTEL NEH COUNTS DUE TO CONTAMINATION  
MIRROR PLANE LIMIT, Azimuth = 90 degrees  
POWER LAW SPECTRUM E\*\*q

CHAN	q = 0	-0.5	-1.0	-1.5	-2.0	-2.5	-3.0	-3.5	-4.0	-4.5	-5.0	-5.5	-6.0
1	.9879	.9311	.6980	.3099	.1144	.0635	.0489	.0420	.0374	.0336	.0305	.0278	.0254
2	.9647	.8519	.5629	.2481	.1008	.0537	.0376	.0303	.0257	.0222	.0194	.0171	.0151
3	.8290	.5357	.2747	.1665	.1298	.1144	.1054	.0990	.0938	.0895	.0857	.0823	.0792
4	.8300	.5357	.2426	.1069	.0599	.0419	.0328	.0270	.0228	.0195	.0168	.0146	.0127
5	.9246	.7632	.4806	.2432	.1327	.0912	.0745	.0662	.0612	.0577	.0552	.0534	.0522
6	.8640	.6519	.3994	.2423	.1735	.1439	.1287	.1192	.1122	.1066	.1018	.0977	.0940
7	.8563	.6385	.3729	.1993	.1199	.0852	.0678	.0574	.0500	.0444	.0399	.0361	.0328
8	.9172	.7832	.5545	.3218	.1756	.1052	.0727	.0563	.0469	.0406	.0362	.0330	.0305
9	.8807	.7291	.5208	.3395	.2282	.1693	.1375	.1186	.1059	.0965	.0890	.0829	.0776
10	.9069	.7906	.6065	.4059	.2536	.1625	.1124	.0840	.0666	.0548	.0461	.0394	.0341
11	.8806	.7573	.5866	.4168	.2900	.2100	.1620	.1324	.1129	.0989	.0884	.0800	.0731
12	.9118	.8212	.6804	.5121	.3594	.2485	.1772	.1329	.1046	.0855	.0717	.0613	.0531
13	.8981	.8103	.6849	.5412	.4094	.3080	.2374	.1900	.1578	.1350	.1181	.1051	.0947
14	.9228	.8578	.7589	.6320	.4980	.3803	.2901	.2261	.1819	.1511	.1288	.1121	.0990
15	.9314	.8791	.7995	.6928	.5703	.4503	.3481	.2692	.2117	.1705	.1409	.1190	.1023
16	.9357	.8947	.8341	.7518	.6510	.5410	.4343	.3407	.2648	.2064	.1625	.1298	.1052

# Protel Contamination Code Monte Carlo - 20000 Trials, Isotropic Distribution

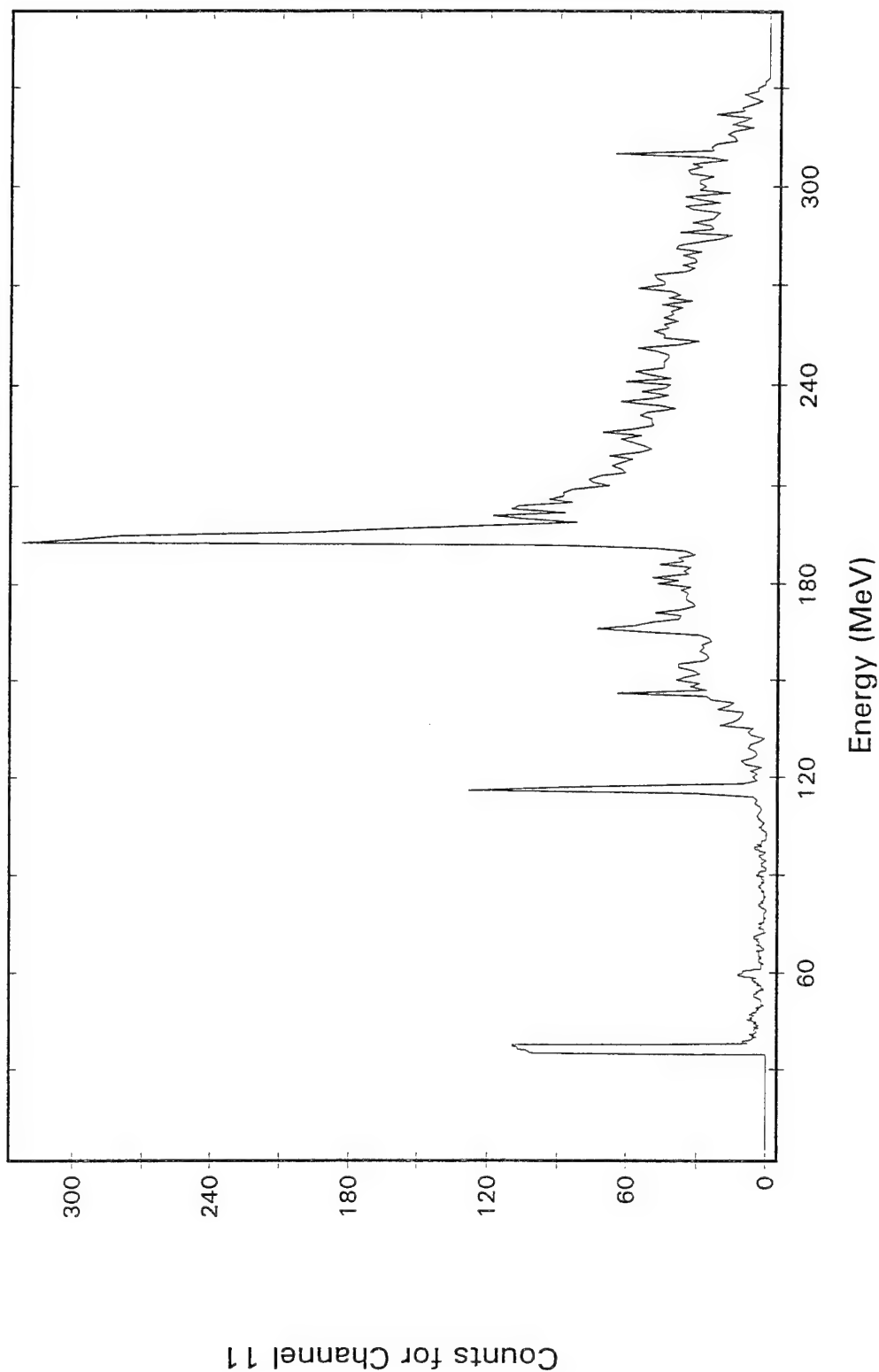


**Figure 35.** Response function for PROTEL HEH Channel 11 for isotropic distribution. The actual non-contamination channel response is the "spike" at the extreme left of the graph.

## Protel Contamination Code

Monte Carlo - 20000 Trials, Isotropic Distribution

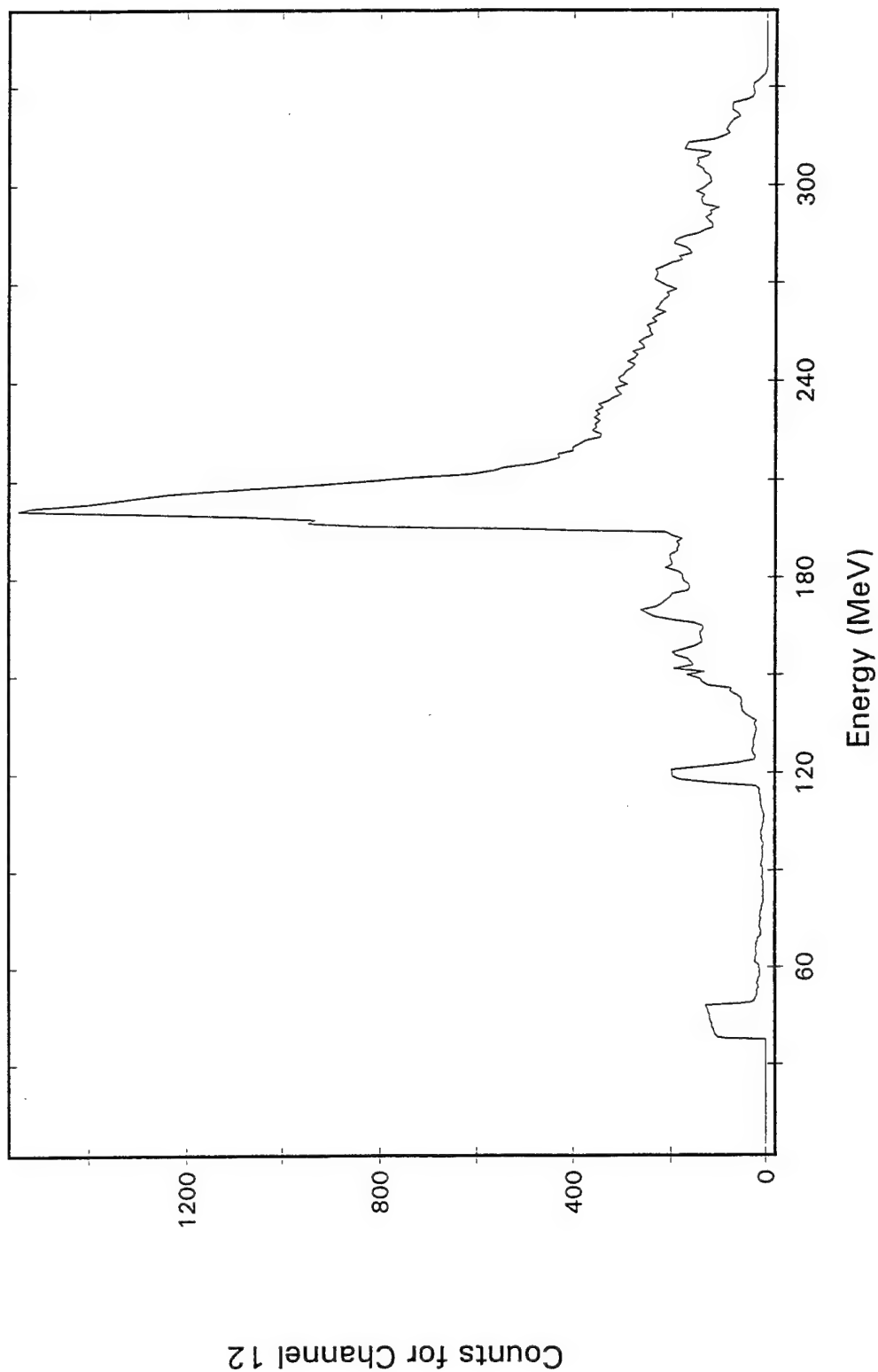
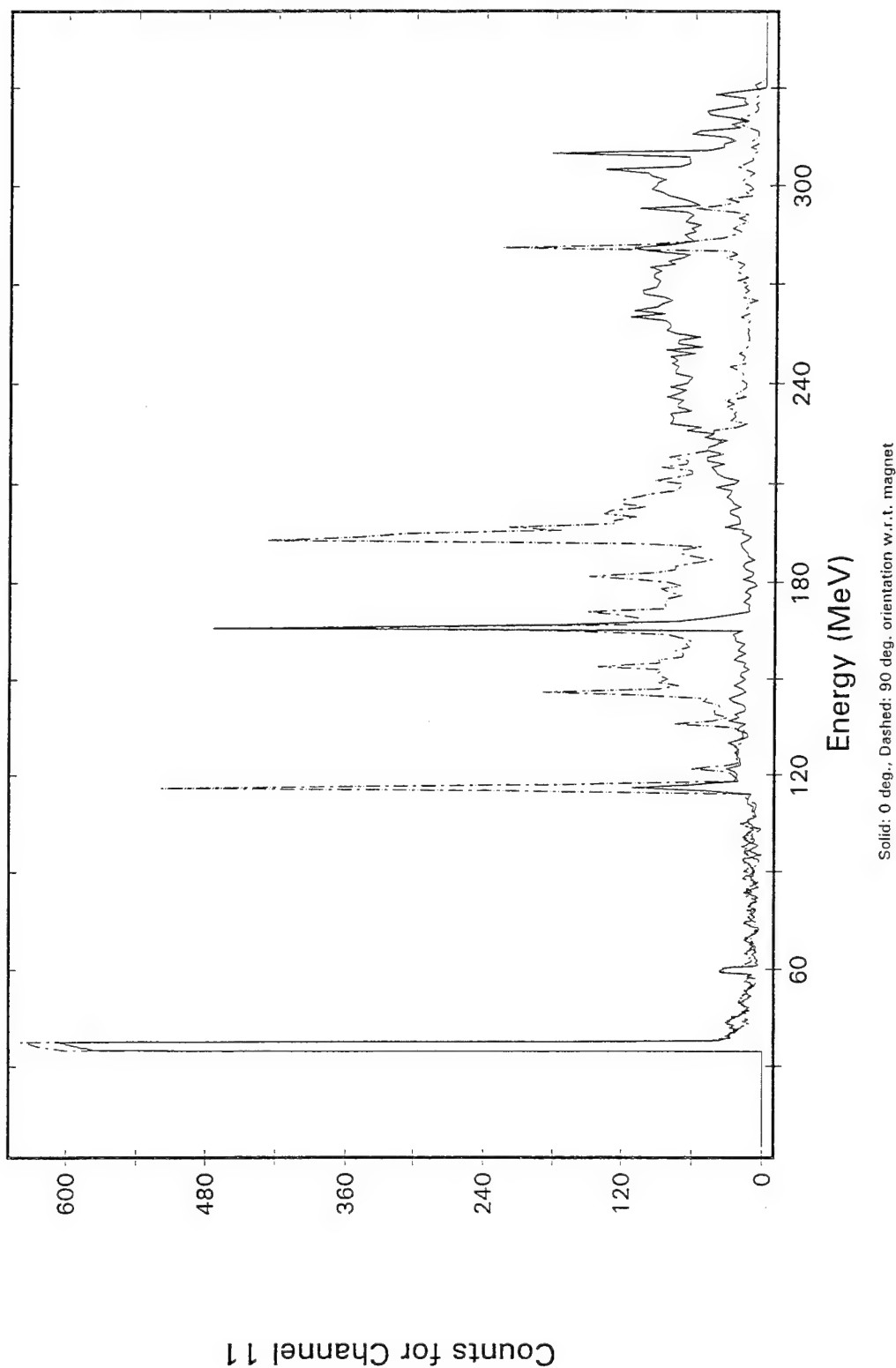


**Figure 36.** Response function for PROTEL HEH Channel 12 for isotropic distribution. The actual non-contamination channel response is the "spike" at the extreme left of the graph.

# Protel Contamination Code

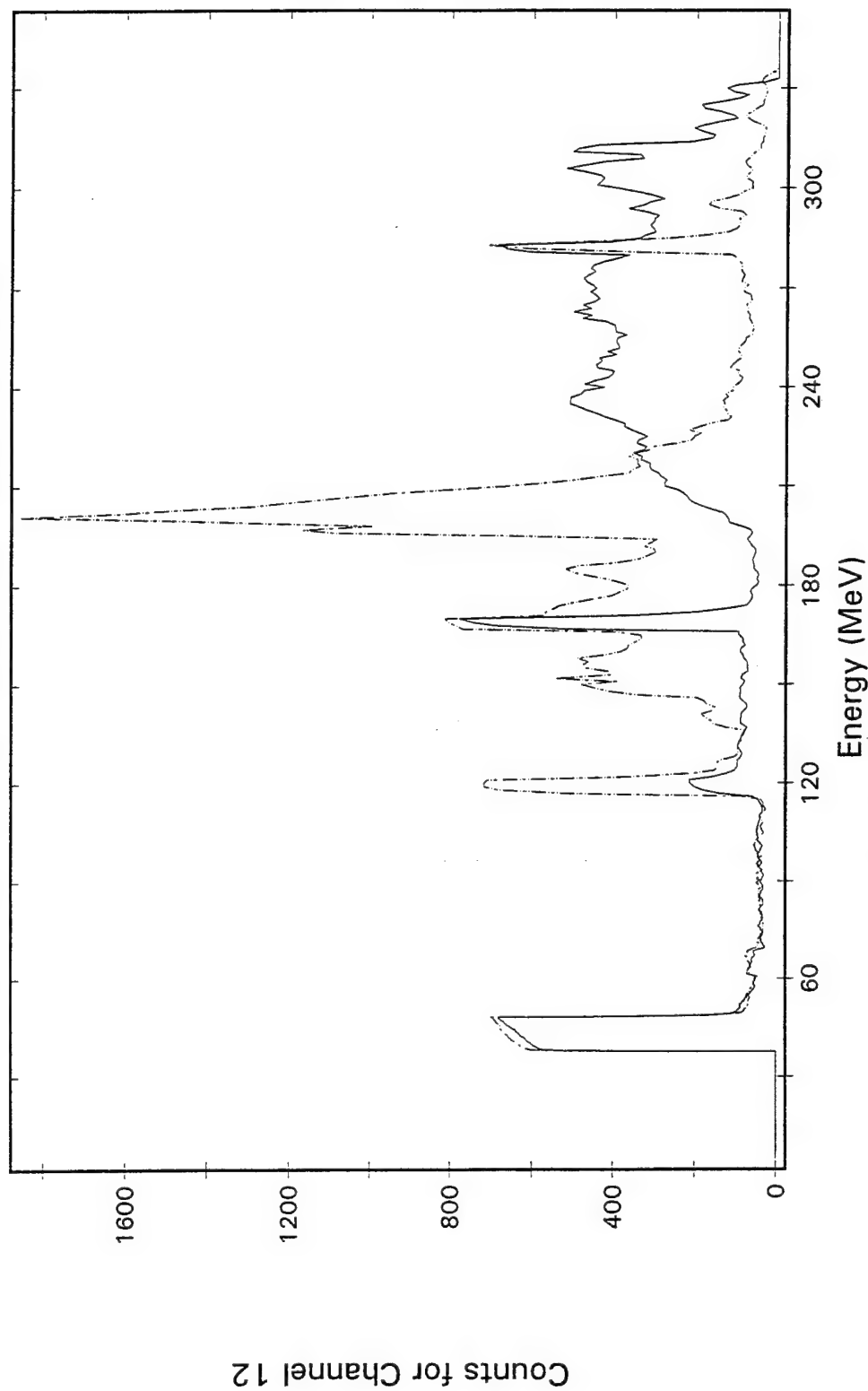
Monte Carlo - 20000 Trials, Mirror Plane Distribution



DATE RUN: 3/22/93

**Figure 37.** Response functions for PROTEL HEH Channel 11 for mirror plane distribution for two orientations of the mirror plane with respect to the deflection magnet 0° (solid line) and 90° (dashed line). The actual non-contamination channel responses are the "spikes" at the extreme left of the graph.

## Monte Carlo - 20000 Trials, Mirror Plane Distribution



Solid: 0 deg., Dashed: 90 deg. orientation w.r.t. magnet

DATE RUN: 3/22/93

**Figure 38.**

Response functions for PROTEL HEH Channel 12 for mirror plane distribution for two orientations of the mirror plane with respect to the deflection magnet  $0^\circ$  (solid line) and  $90^\circ$  (dashed line). The actual non-contamination channel responses are the "spikes" at the extreme left of the graph.



## 7.2 EFFECT OF APERTURE AND ROTATION ON OBSERVATIONS OF PROTON PITCH ANGLE DISTRIBUTIONS

During the lifetime of the CRRES satellite, the Proton Telescope (PROTEL) provided detailed measurements of the Proton Population in the radiation belts and in the near Earth environment up to geosynchronous altitudes. The proton populations were measured as functions of energy and pitch angle over approximately 1000 orbits. An intense magnetic storm (proton event) occurred in March of 1991. This storm produced significant changes in the distribution of trapped particles (electrons, protons, and other ions). For the periods preceding the storm and following the storm, the observed proton population in the radiation belts appeared to be very stable. For purposes of discussion in this report, the data obtained before the storm is referred to as "Quiet", and the data obtained after the storm is referred to as "Active".

This report describes the effect that the aperture ( $8.5^\circ$  half-angle acceptance cone) for the PROTEL High Energy Head (HEH) and the satellite rotation would have upon the observations of pitch angle distributions in order to better understand the Quiet and Active model data. Error estimates based upon the simulation are also provided.

### 7.2.1 Introduction

Earth's radiation belt is a region in space in which charged particles (electrons, protons and ions) are trapped by Earth's magnetic field. The motion of a trapped particle is generally a spiral up and down the magnetic field lines. At a given instant of time, the velocity vector of the charged particle makes an angle  $\alpha$  with respect to the magnetic field vector; the angle  $\alpha$  is called the pitch angle. During the motion of a charged particle, the pitch angle of the particle as it crosses the magnetic equator determines the latitude at which the particle "mirrors", at which the particle reverses direction along the direction of the magnetic field. As a result, it is customary to characterize the motion of trapped charged particles by their equatorial pitch angle and their L-shell value, the length of the radius vector to the magnetic equator field line crossing (in Earth radii). Charged particles are "lost" when they encounter (collide with, or are scattered by) neutral or other charged particles in regions of higher density. Thus, for lower L-shell values, charged particles will be absent from the ends (for equatorial pitch angles  $\alpha$  near  $0^\circ$  and  $180^\circ$ ) of the distribution. For stable populations of charged particles, the distribution in equatorial pitch angle will be (nearly) symmetric around  $90^\circ$ . The range of values of equatorial pitch angle for which particles will be absent is referred to as the loss cone, and will be characterized by the loss cone angle  $\alpha_c$ . The pitch angle range for stable particles is:  $\alpha_c < \alpha < 180^\circ - \alpha_c$ .

Neglecting the loss cone, because of the symmetry around  $90^\circ$ , it is customary to mathematically fit equatorial pitch angle distributions to functions of the form  $\sin^N \alpha$ . To represent the effect of the loss cone, it is preferable to use (what we shall call here) a "modified"  $\sin^N \alpha$ , that is, a distribution of the form:

$$j(\alpha, E, L) = A(E, L) \left[ \frac{\sin^2 \alpha - \sin^2 \alpha_c}{1 - \sin^2 \alpha_c} \right]^{\frac{N(E, L)}{2}} \quad (7-1)$$

With the normalization chosen above,  $A(E, L)$  is the flux at  $\alpha = 90^\circ$ . Note that  $\alpha_c$  depends upon  $L$ . The above distribution reduces to the  $\sin^N \alpha$  distribution when  $\alpha_c = 0$ .

In this report, we will examine the effects of the PROTEL HEH aperture ( $8.5^\circ$ , and of the flux averaging due to the rotation of the CRRES spacecraft during the 1 second integration period per observation, the latter corresponding to a  $12^\circ$  rotation. We will assume that the actual equatorial pitch angle distribution is a modified  $\sin^N \alpha$  distribution (Eq. (7-1)). As a result of the rotation, there will be an apparent shrinking of the loss cone. The result is that protons will be observed in the loss cone.

In the actual PROTEL data analysis, the flux in the first bin below the loss cone was attributed to contamination (particle entry into the detector of higher energy protons through the passive shielding triggering responses which appear valid to the coincidence/anticoincidence detector logic). The loss cone flux was subtracted from the observed fluxes, and the resulting data was fit to a single modified  $\sin^N \alpha$  distribution, and to the sum of two such distributions (as described below).

In the PROTEL Quiet and Active Model equatorial pitch angle distribution data fits, much of the data fits well to a single distribution of the form of Eq. (7-1). In many cases, a fit to the sum of two such distributions (performed as described below) provides a substantial improvement.

In Section 7.2.2 we shall describe the assumptions and methodology used in the research presented in this report. In Section 7.2.3 we shall present the results of the simulations described in Section 7.2.2. Tables and graphs will be provided.

### 7.2.2 Methodology

For each channel, the PROTEL detector measures the number of protons hitting the detector with energy in the channel range during a single integration period ( $\sim 1$  second). The observed proton count is used to compute the corresponding flux for the local pitch angle bin (determined from the spacecraft orientation, magnetometer data, and computed magnetic field vector, the latter obtained from magnetic field model) and  $L$ -shell bin. The corresponding data is mapped to an equivalent equatorial pitch angle bin and averaged over a data collection time interval. For the Quiet and Active models, the time intervals were the duration of the data collection periods for the models.

The approach used here is to simulate the effect of aperture and rotation upon observations of a "pure" modified  $\sin^N \alpha$  pitch angle distribution by computing the average instantaneous flux over the aperture, and then averaging the result over the  $12^\circ$  rotation.

In order to compute the flux integral, the following coordinate system (fixed relative to the PROTEL HEH axis) was used. The unit normal  $\mathbf{n}$  (also the PROTEL HEH symmetry axis) to the first detector surface is the z-axis  $\mathbf{n} = (0,0,1)$ . The orientation in the spin plane is described by an angle of rotation,  $\gamma$ , with the reference direction  $\gamma = 0$  chosen so that the projection of the Magnetic field vector  $\mathbf{B}$  upon the PROTEL HEH spin plane is taken to be the y direction. The unit vector  $\mathbf{b}$  in the direction of  $\mathbf{B}$  is given by:

$$\mathbf{b} = (\sin i, \cos i \sin \gamma, \cos i \cos \gamma) \quad (7-2)$$

where  $i$  is the angle between the mirror plane and spin axis, and  $\gamma$  is the angle in the spin plane describing the current orientation of the PROTEL HEH relative to the projection of  $\mathbf{B}$  onto the spin plane. The unit vector  $\mathbf{u}$  pointing to the direction of an arbitrary incoming particle is given by

$$\mathbf{u} = (\cos \phi \sin \theta, \sin \phi \sin \theta, \cos \theta). \quad (7-3)$$

The particle count corresponding to a given differential flux is given by the following integral:

$$N(E,L) = \int_{\Delta t} dt \int_{\Delta E} dE \int_{\Omega} \eta(\Omega, \dots) j(E,L,\Omega) \mathbf{u} \cdot \mathbf{n} d\Omega \quad (7-4)$$

where  $t$  is the time,  $E$  the energy,  $j$  the differential flux,  $\Omega$  solid angle, and  $\eta$  describes the detection efficiency. Here, we chose  $\eta = 1$  for directions within the PROTEL HEH acceptance cone, and 0 otherwise.

We are therefore interested in evaluating the following integral for each value of  $N$  and  $\gamma$  of interest:

$$\int_{\theta=0}^{8.5^\circ} \int_{\phi=0}^{360^\circ} \left[ \frac{\sin^2 \alpha - \sin^2 \alpha_c}{1 - \sin^2 \alpha_c} \right]^{\frac{N}{2}} \cos \theta \sin \theta d\theta d\phi \quad (7-5)$$

where  $\cos \alpha = \mathbf{b} \cdot \mathbf{u}$ . An analytic expression of this integral is not available. Monte Carlo methods were used to compute this integral for each appropriate angle bin for selected values of  $N$  ranging from 2 to 100 at intervals of  $\gamma$  of 0.5 degrees.

For the Monte Carlo integration, for each value of  $N$  and  $\gamma$ , 10,000 trials were used. For each trial, the integrand was computed, where  $\theta$  and  $\phi$  were randomly chosen from a uniform distribution in the range between  $0^\circ$  and  $8.5^\circ$  and  $0^\circ$  -  $360^\circ$ , respectively. The sum of the integrand (over the number of trials) was then computed. The normalization is obtained by performing the parallel sum of  $\sin \theta \cos \theta$ . The ratio represents the average value of the differential flux (for the value of  $N$  and  $\gamma$ ) over the aperture.

The effect of rotation is then taken into account by computing the average of the computed flux over a  $12^\circ$  interval (in  $\gamma$ ), centered at each of the PROTEL pitch angle bin angles. For fixed  $N$  and  $i$ , a simulated "observed" pitch angle distribution is obtained by computing the pitch angle  $\alpha$  corresponding to  $\gamma$  using the equation  $\cos \alpha = \cos i \cos \gamma$ .

In order to emulate the data reduction procedure used for the PROTEL pitch angle observation data, the value of the (simulated) flux for the first PROTEL pitch angle bin below  $\alpha = \alpha_c$  was subtracted from each of the flux bins. The resulting data was then fit to both a single and the sum of two functions of the form of Eq. (7-1) using the same value for the loss cone boundary  $\alpha_c$ .

The final simulated pitch angle distributions obtained in this manner reflect the combined results of the simplified modeling of the PROTEL HEH detector, the flux averaging due to the rotation of the spacecraft, and of the data reduction methods used to generate the CRRES Active and Quiet Model database, as applied to the case of a single pitch angle distribution of the form of Eq. (7-1).

Fits of the Active and Quiet model equatorial pitch angle distributions to functions (a single, and the sum of two distributions) of the form of Eq. (7-1) were made. For the case of a fit to a single modified  $\sin^N \alpha$ , linear least squares fits were made to  $\log_{10} j(E, L, \alpha)$ , for which the basis functions are given by:

$$1, \quad \frac{1}{2} \log_{10} \left( \frac{\sin^2 \alpha - \sin^2 \alpha_c}{1 - \sin^2 \alpha_c} \right) \quad (7-6)$$

The fits to the sum of two distributions of the form of Eq. (7-1) were performed as follows:

A fit to a single distribution was made using a set of points (usually from  $5^\circ$  to  $35^\circ$  above  $\alpha_c$ ). The fluxes corresponding to the fits were computed, and subtracted from the observed fluxes. The differences were then used for a fit to a second distribution, using a set of points (spanning  $\sim 30^\circ$ ) near  $\alpha = 90^\circ$ . To compare the results of a single and a "double" fit, correlation coefficients were computed between the  $\log_{10}(\text{flux})$  from the original data, and the result  $\log_{10}(\text{fit values})$  of the fit.

### 7.2.3 Results

Monte Carlo computations for the flux were performed for  $N = 4, 5, 6$ , and  $8$ , for  $L$ -values of  $1.25 - 3.70$  at  $0.05$  intervals. The  $L$  - dependence arises from the dependence of  $\alpha_c$  on  $L$ ; the same values of  $\alpha_c$  were used for the fitting of the PROTEL Quiet and Active model data. Note that  $\alpha_c$  ranges from  $47.5^\circ$  on the left, to  $0.25^\circ$  on the right. The low values on the left hand side of the graph result from the subtraction of the "loss cone" flux. Figure 39 provides an estimate of the error in the flux for equatorial pitch angles of  $\alpha = 90^\circ$ . Caution should be used in using the data in Figure 39 for estimates at other pitch angles.

Figure 39 below shows the computed equatorial flux (incorporating the effects of the HEH aperture and rotation) at  $\alpha = 90^\circ$ , as a function of  $L$  for the four  $N$  values.

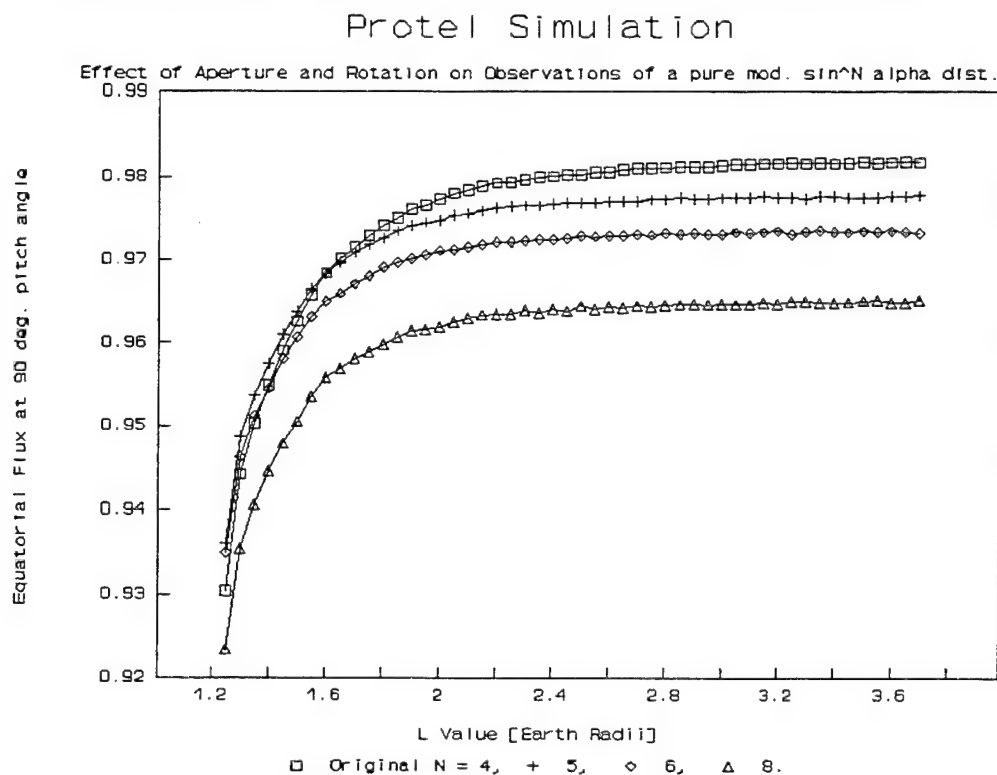


**Figure 39.** Computed equatorial flux at  $\alpha = 90^\circ$  (incorporating the effects of the PROTEL HEH aperture and rotation), as a function of  $L$  for modified  $\sin^N \alpha$  distributions for  $N = 4, 5, 6$  and  $8$ . Note that  $\alpha_c$  ranges from  $47.5^\circ$  on the left to  $0.25^\circ$  on the right. For the original distributions,  $A(E, L)$  was taken to be 1.

The resulting pitch angle distributions have been fit to both a single and the sum of two modified  $\sin^N \alpha$  equatorial pitch angle distributions. The quality of these fits are generally not as good as those obtained from the actual active and quiet model data in much of the radiation belt regime. For single fits to the actual data, it was found that if data points near the loss cone were included in the fitting process (usually a single point), then the values of  $N$  obtained (as a function of  $L$ ) were very "noisy". The same behavior was found in attempting to fit the "simulated" pitch

angle distributions. A test was performed, in which different "seeds" for the random number generator were used for the same case, in which fit parameters varied only slightly ( $\sim 2\%$ ). For the simulation, it was necessary to exclude data points from within at least  $2.5^\circ$  of the loss cone from the fit.

Figure 40 is a graph of  $A(E,L)$  obtained from the fit to a single modified  $\sin^N \alpha$  distribution; if the quality of the fits were better, the data represented here should be approximately the same as that found in Figure 39.

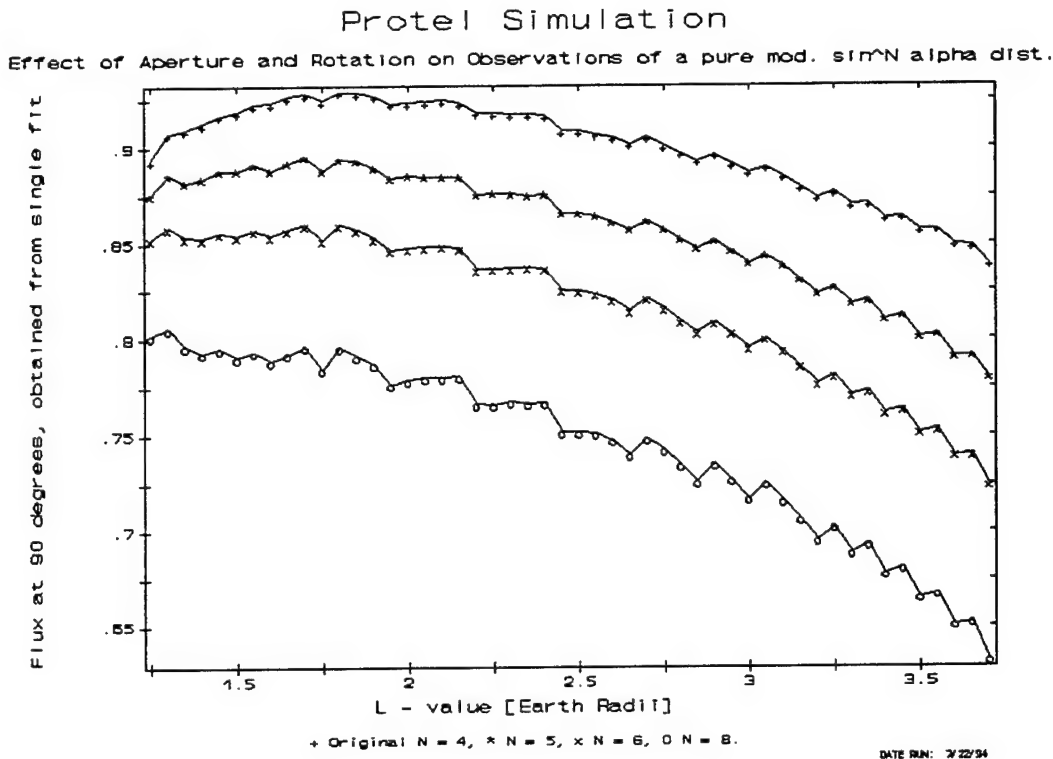


**Figure 40.** The computed distributions (incorporating the effects of aperture and rotation) have been fitted to a single modified  $\sin^N \alpha$  distribution.  $A(E,L)$  from the single fits is plotted vs  $L$  for  $N = 4, 5, 6$ , and  $8$ .

In the single fits, the value obtained for  $A(E,L)$  was generally below the computed flux at  $\alpha = 90^\circ$ . Data from the single fits was used to compute the equatorial omnidirectional flux. The results of the computations are provided in Figure 41, in which the vertical axis represents the ratio of the omnidirectional flux (computed from the fit of the simulation data/nominal).

The fits of the simulation pitch angle distributions to the sum of two modified distributions were only slightly better, but  $A_1(E,L) + A_2(E,L)$  from the dual fits is in good agreement with the computed equatorial omnidirectional flux. Figure 42 provides the dual-fit version of the data presented in Figure 41.

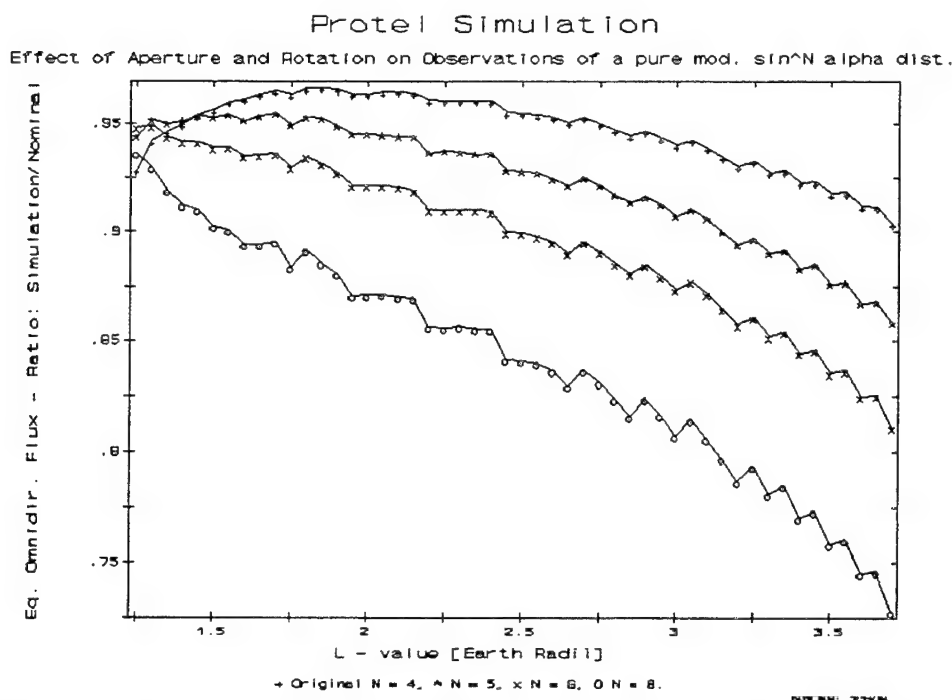


**Figure 41.** Ratio of equatorial omnidirectional flux (from fits of the computed pitch angle distribution to a single modified  $\sin^N \alpha$  distribution) to that of the original modified  $\sin^N \alpha$  distribution is plotted as a function of L for N = 4, 5, 6, and 8.

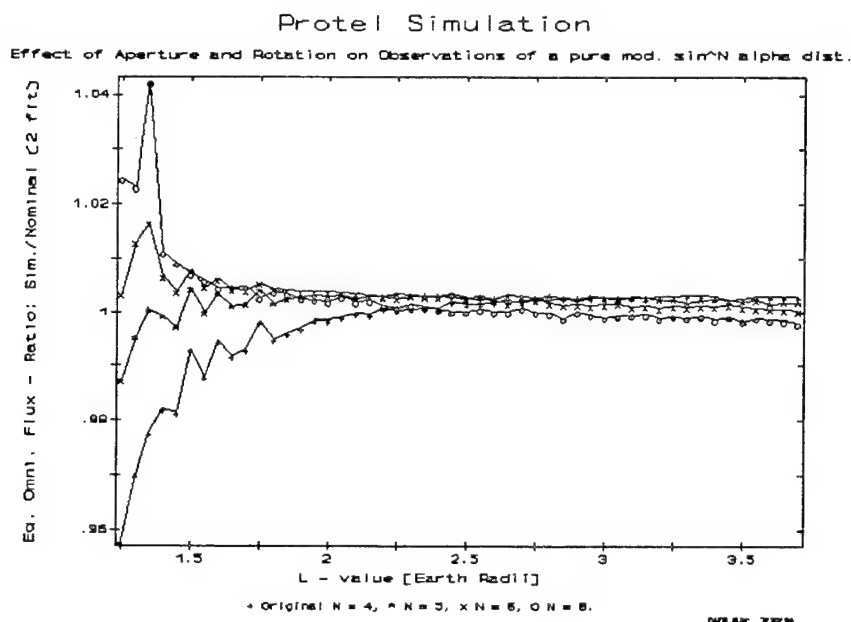


**Figure 42.** Ratio of equatorial omnidirectional flux (from fits of the computed pitch angle distribution to the sum of 2 modified  $\sin^N \alpha$  distributions) to that of the original modified  $\sin^N \alpha$  distribution is plotted as a function of L for original N=4, 5, 6, and 8.

A direct comparison of the original and simulated pitch angle distributions is provided in Figure 43, for the case of  $N = 4$ ,  $L = 1.25$ . Other cases illustrate similar behavior, the only difference is the scale of the differences which appears to be proportional to the differences at  $\alpha = 90^\circ$  (see Figure 39).

EFFECT OF AVERAGING (APERTURE OF HEH, ROTATION)  
ORIGINAL DIST. AND RESULT OF AVERAGING

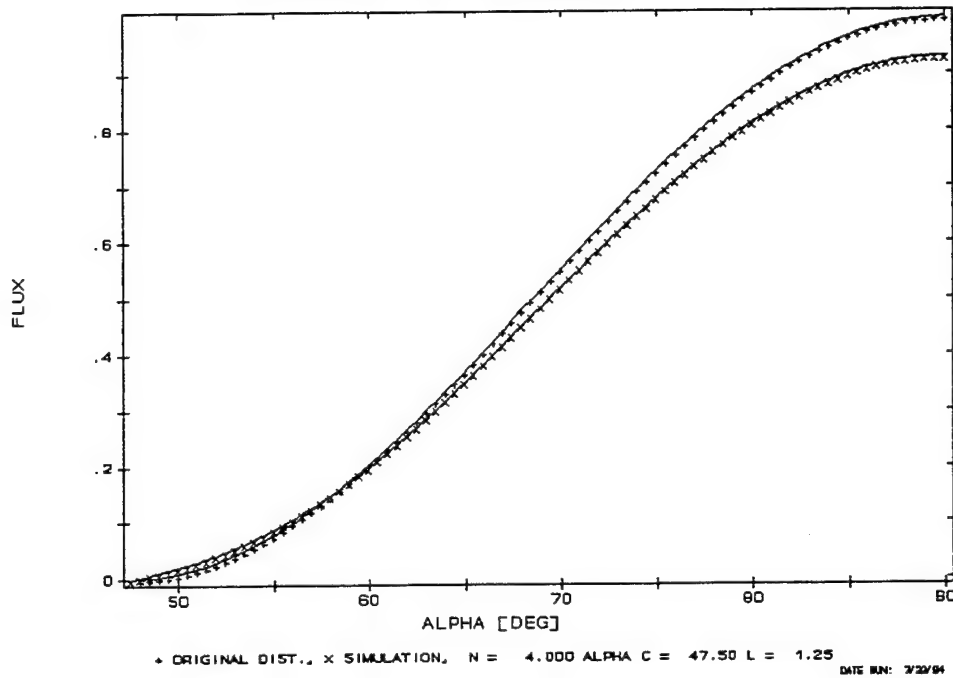


**Figure 43.** Sample comparison ( $N=4$ ,  $\alpha_c=47.5$ ,  $L=1.25$ ) of the computed pitch angle distribution with the original modified  $\sin^N \alpha$  pitch angle distribution.



## 8. CRRES INSTRUMENT MODELING: CRRES DOSIMETER

The design of the CRRES dosimeters is based on the Space Radiation Dosimeters successfully used on the DMSP 7 satellite [Gussenhoven, *et al.*, 1986]. Modifications of the original DMSP design were required because of the different operational environment and the orbit of the CRRES satellite; in particular, the CRRES orbit passes through the radiation belts, subjecting the CRRES dosimeter to much higher count and dose rates than those encountered by the 800 km altitude circular orbit of DMSP. A report describing the modeling of the DMSP and CRRES dosimeters using the path length distribution method [Hein and Bass, 1993] has already been published. In this section, we shall provide a summary of the results of the modeling.

A description of the CRRES dosimeters may be found in Morel, *et al.* [1989]. An overall description of the CRRES Satellite and Experiments can be found in Gussenhoven, *et al.* [1985]. The CRRES dosimeters are a set of four disk shaped silicon particle detectors, each of which is mounted on a platform at the center of a hemispheric aluminum shell. The thickness of the hemispherical shell is chosen to set the lower energy limits of charged particles which will arrive at the detector. The physical and geometrical parameters of the detectors are presented in Table 35.

TABLE 35. Physical and Geometric Parameters of the CRRES Detectors					
Detector #	Detector Area [cm <sup>2</sup> ]	Detector Thickness [microns]	Ratio: thickness/radius D/R	Thickness of Al. Hemisphere [gm/cm <sup>2</sup> ]	Minimum Proton Energy Required to Penetrate Aluminum Hemisphere [MeV]
1	0.00815	403	0.79123	0.55	20
2	0.051	434	0.34063	1.55	35
3	0.051	399	0.31326	3.05	51
4	1.000	406	0.07196	5.91	75

The objective of the modeling effort was to develop a software model of the CRRES dosimeter to compute proton counts and dose for proton energy spectra, in particular, for the following proton angular distributions: isotropic, mirror plane, and  $\sin^N \alpha$  pitch angle distributions. The modeling of PROTEL and the CRRES dosimeter was performed in order to cross-calibrate the two instruments. The silicon detectors measure the energy loss of a charged particle passing through their active regions. For simplicity in computation, only the active portion of the detectors is modeled. The modeling assumes that the protons penetrate the detectors, travel in a straight line, and undergo deceleration in the direction of motion (and energy loss) due to the

interaction of the protons with the electrons in the detector. Energy losses in silicon were computed using both the Janni energy-range relations [Janni, 1982] and power law fits to the Janni data. For each detector, there are two count and dose channels, LOLET, and HILET. The LOLET channels are sensitive to electrons and respond to energy losses less than 1 MeV. The proton contribution to the LOLET channels is expected to be small compared to that produced by high energy electrons which penetrate the aluminum hemisphere.

In previous studies, the infinite slab approximation was used to compute proton counts, dose, and geometric factors. The infinite slab approximation is best suited to the case in which the thickness of the detector is small compared to its other dimensions. The loss of accuracy with thickness results from edge effects, that is, due to particles which enter the top and exit through the edge of the detector, or enter the side and leave the side of the detector. The ratio of the thickness of the silicon detector to its linear dimensions for detector 1 is small compared to the detectors used for the DMSP, or the other CRRES dosimeter detectors. The validity of the infinite slab assumption does not appear to hold for detector 1.

The methodology used by Radex was to compute the path length distributions for the above proton angular distributions for the CRRES dosimeters, and use them to compute the usual flux and dosage integrals, geometric factors, and response functions.

The path length distribution may be considered to be either a histogram of possible path lengths or as the probability that a particle passing through the material object in a straight line will have a given path length. The path length distribution depends upon the geometry of the detector and on the particle angular distribution. The application of the path length distribution approach to electrons is unsuitable, because it is doubtful that a substantial fraction of electrons will travel in straight lines while passing through the detector.

A Monte Carlo approach was used to compute the path length distributions. Only the simplest case, an isotropic distribution, will be described here.

To facilitate the Monte Carlo computation, it was necessary to break the calculation into two parts. Case 1 corresponds to the case in which a proton strikes the top surface, and leaves either through the bottom of the detector or through the side of the detector. Case 2 corresponds to the case in which a proton enters the detector through the side and leaves either through the bottom or through the side of the detector. A geometric argument is then needed to combine the results of the two cases.

For Case 1, a Monte Carlo "trial" consists of the following steps: Select a random point (position vector)  $(x,y,D)$  on the top surface. Then select the velocity direction (unit vector) of the particle  $\mathbf{u} = (\cos\psi \sin\beta, \sin\psi \sin\beta, -\cos\beta)$  as follows: Select  $\mu = \cos \beta$  from a uniform distribution in the interval  $[0, 1]$ , where  $\beta$  is the angle between the normal to the surface and the direction of incidence. Compute  $\sin \beta$ . Select the direction of the projection of the velocity vector onto the plane of the disk  $\psi$  from a uniform distribution in the interval  $[0, 2\pi]$ , and compute  $\mathbf{u}$ .

We then use a trial value  $q=D/\cos\beta$ , and test whether  $(x+q \cos\psi \sin\beta)^2+(y+q \sin\psi \sin\beta)^2 \leq R^2$ . If so, increment the appropriate top-bottom bin counter for  $q$  by 1. If not, solve the quadratic equation  $(x+q \cos\psi \sin\beta)^2+(y+q \sin\psi \sin\beta)^2 = R^2$  for  $q$ , and increment the appropriate top-side bin counter for  $q$  by 1.

For Case 2, a Monte Carlo "trial" consists of the following steps: For an arbitrary point on the circumference of the disk, randomly select a height  $h$  above the bottom surface from a uniform distribution in the interval  $[0, D]$ . For reasons of symmetry, the position vector of that point may be chosen to be  $(-R,0,h)$ . The velocity direction (unit vector)  $\mathbf{u} = (\cos\psi \sin\beta, \sin\psi \sin\beta, -\cos\beta)$  of the particle is selected as follows: Select  $\beta$  from a uniform distribution between  $[0, \pi/2]$ . Select  $\psi$  from a uniform distribution in the interval  $[-\pi/2, \pi/2]$  and compute  $\mathbf{u}$ . For the trial value  $q=h/\cos\beta$ , test whether  $(-R+q \cos\psi \sin\beta)^2+(q \sin\psi \sin\beta)^2 \leq R^2$ . If so, increment the appropriate side-bottom bin counter for  $q$  by 1. If not, select the trial value  $q=2R \cos\psi/\sin\beta$ . If  $0 \leq q \cos\beta \leq h$  increment the appropriate side-side bin counter for  $q$  by 1.

To combine the Case 1 and Case 2 Monte Carlo results into a single path length distribution, it is necessary to provide suitable geometric and physical reasoning which justifies the assumptions underlying the computation. First, it is necessary to normalize both distributions. It is then necessary to determine the relative path length contributions entering from the top and from the side. For the Case 1 computation, the number of particles striking the top of the detector is proportional to the surface area,  $\pi R^2$ . The Case 2 computation was based upon the contribution due to particles striking the detector along a vertical line on the boundary. The number of particles striking the detector from the side is proportional to  $2\pi DR$ . The total contribution is the weighted sum of the two contributions, and is given by:

$$f(q) = (T(q) + 2 D S(q))/(1 + 2 D) \quad (8-1)$$

where  $T$  and  $S$  are the normalized Case 1 and Case 2 path length distributions.

Figure 44 shows the path length distribution computed using the Monte Carlo method described above for CRRES dosimeter detector 1 (together with the corresponding infinite slab distribution). Note that the minimum path length for the infinite slab distribution is equal to the thickness of the detector. The two distributions are normalized.

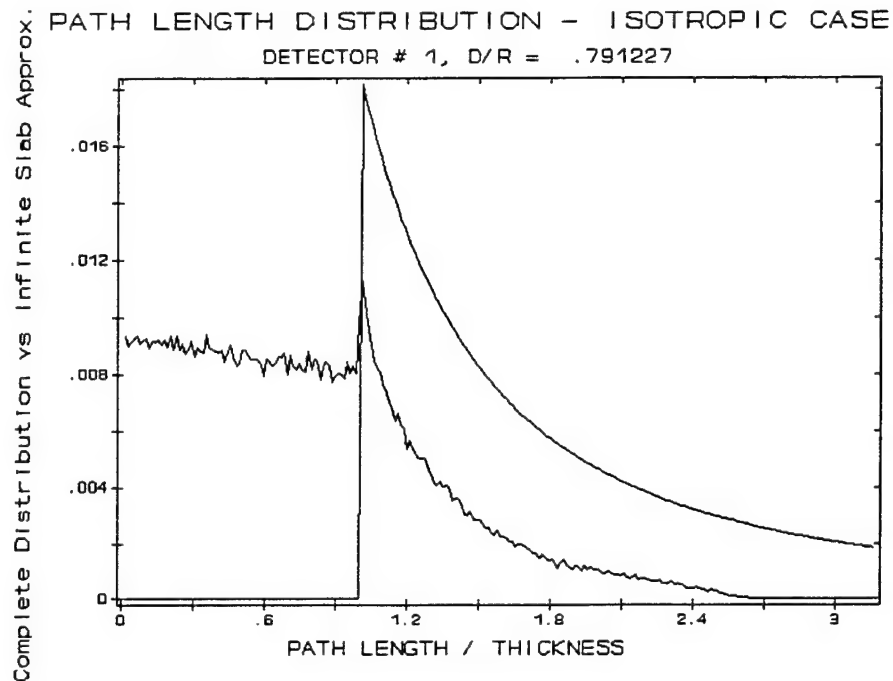


**Figure 44.** Path length distribution computed using the Monte Carlo method for CRRES dosimeter detector 1.

The computations for the mirror plane and  $\sin^N \alpha$  path length distributions were performed in a similar manner, using the appropriate angular distribution functions. These distributions are angle dependent, depending on the angle made by the detector and the magnetic field direction. Path length computations were performed at 1 degree intervals from 0 to 90 degrees for the mirror plane distribution, and at 5 degree intervals for  $N = 6, 8, 10$ , and 12 for the  $\sin^N \alpha$  distributions. Typically, 100,000 trials were performed for each path length computation, using 2,500 "bins".

The computation of the response functions proceeds as follows: For each energy incident on the external dome, the corresponding energy arriving at the detector surface is computed using the Janni energy range relations for aluminum. Then, for each path length, the corresponding energy loss in silicon is computed; depending on the energy loss, the appropriate LOLET or HILET count channel is incremented by the value of the path length distribution function. For dose, the corresponding dose counter (as discretized by the Dosimeter's on-board processor) is incremented using the nominal dose multiplied by the value of the path length distribution. The resulting functions of energy for the LOLET and HILET channels are the count and dose response functions. The geometric factors are obtained by integrating the response functions over a particular proton energy spectrum. Tables of geometric factors for power law spectra have been provided in *Hein and Bass [1993]* for various pitch angle distributions.

## 9. LOW ENERGY PLASMA MOMENTS FROM CRRES LEPA DATA

There are data files containing measurements made by the scientific magnetometer and the Low Energy Plasma Analyzer (LEPA), two of the instrument packages flown on the Combined Release and Radiation Effects Satellite (CRRES) mission. Several PC-based software codes have been written to numerically derive the three-dimensional profile of electron and ion plasma density from piecewise post-processing of the aforementioned data files. The purpose of this report is to provide assistance in running those codes and to furnish essential information for better understanding of the outputs from the programs. The initial discussion in this section will focus on the general operation of the LEPA instrument. Immediately following is an overview of the theoretical concepts incorporated into the software packages. Next, the basic steps in the software processing will be outlined. The final paragraph in this section will be a brief review on the subsequent sections where detailed descriptions of the programs are provided.

Other documentation is available that provides a more detailed description of LEPA. The basic principles of the LEPA design and operation are described in *Hardy, et al.*, [1993a]. Considerable details on electronic operations and calibrations of the LEPA are available in *Hardy, et al.* [1993b]. Outlined discussion on algorithms needed to process the LEPA datafiles is given in a supporting document [*Kerns*, 1993]. With the wealth of information available, this guide will only describe how to use the software codes developed by Radex for processing the particle data collected by LEPA and the geomagnetic field measurement made by the scientific magnetometer. There will be some discussion on the theoretical motivations and the basic background details necessary to fully understand the outputs of the software codes. The enclosed text will provide step by step details of the software processing from determining the measured geomagnetic field components to binning the differential directional fluxes for extracting the three-dimensional distribution functions.

### 9.1 BACKGROUND INFORMATION ON LEPA

CRRES was launched in July 1990 with the planned 5-year mission to sample radiation levels by detecting charged particles, and to measure geomagnetic fields over a large portion of near-Earth space. The satellite occasionally ejected canisters filled with materials and measured the resulting induced radiation effects. At other times, onboard instrumentation observed a nominal radiation environment. Two types of experiments were conducted onboard the satellite. The majority of the experiments were designated as being of the Geosynchronous Transfer Orbit (GTO) class; the remainder relegated to the Low Altitude Satellite Studies of Ionospheric Irregularities (LASSII) class. CRRES orbited Earth in a low-inclination geosynchronous transfer orbit collecting and transmitting data until a battery malfunction cut off the telemetry link permanently in October of 1991. Among the experiments and instrument packages on the satellite was LEPA, the key instrument relevant to this guide.

LEPA is capable of detecting charged particles with energy ranging from 10 ev to 30 kev. The device is actually a pair of tri-quadraspherical electrostatic analyzers; each analyzer is designed to sample only the incident particles within a spatial resolution defined by an operational mode and within a certain energy range selected by a voltage mode. The energy of the particle being detected at a given time is a function of the voltage difference between concentric spherical sections. This voltage difference is controlled by a sweep circuit which sequences through 30 or 120 energy steps. Essentially, the instrument package collects data on both the electrons and ions within selected energy range concurrently in time but separately by charge polarity of the species. The triggering and timing operations of LEPA is done in conjunction with other systems.

At this point, it is sufficient to mention only briefly the sensors and systems that would contribute to the data gathering by LEPA. The onboard scientific magnetometer measures the geomagnetic field and notifies onboard systems of the directional angles of the field lines. The triggering of detection by LEPA for energetic particles within specific pitch angle ranges is governed by signals from the magnetometer. By observing the passing of the sun with a sensor, CRRES confirms its spinning rate with LEPA; the analyzers then synchronize their operation to execute an integral number of voltage sweeps per spin. Since the satellite is spinning, LEPA samples the region of space around the spin axis and needs only to store the data as a time-dependent series of sensors sweeps.

The spatial resolution of LEPA is delimited by its sensor field of view (FOV) subdivided into discrete angular bins. The FOV for the device is limited to an aperture width of 5.5 degrees with a elevation range from 26 to 154 degrees relative to the spin axis. This detection "fan" can angularly resolve the counts into sixteen 8-degree bins, arranged symmetrically with respect to the plane normal to the spin axis. These bins are henceforth referred to as "zones", and numbered 0 to 15. Zone 15 is covered and is used for collecting background counts. Each spin is divided into 64 sectors (5.6° per sector), with one voltage sweep executed per sector.

LEPA is designed to measure the flux at 30 or 120 energy steps for each of 32 sectors within each of 8 zones for ions and for electrons. Constraints on the telemetry data rate require reduction in the amount of data actually transmitted. To accomplish this, LEPA has a number of operational modes which sacrifice resolution in energy, direction, time, or some combination of these. The mode used at any given time is controlled by ground commands. The modes we are concerned with in this report are modes 0 and 10.

In mode 10 (sometimes designated "A") the voltage sweep sequences through 30 energy steps. The amount of telemetry data is reduced by combining the results (ion results are summed; electron results are averaged) for 4 adjacent sectors and two adjacent zones. The combined sectors and zones are sometimes called coarse sectors and zones. In mode 0, the ion data are collected in the same format as in mode 10. However, the electron data are collected only for sectors which contain the loss cone, or are located approximately perpendicular to the loss cone (1/4 spin from the loss cone), without being combined into coarse sectors or zones. There are usually 2 loss cone sectors and 2 "perpendicular" sectors per spin. Detection of these sectors



is based on signals from the onboard magnetometer. Additional data are sent in these modes, but not used in this work.

Regardless of the operating mode and voltage level, LEPA packs detector signals and passes the compressed data to the telemetry system. The transmitted data contains specific information assigned at particular locations within the byte streams that are related to the CRRES instrument packages and onboard systems, such as the sensors and magnetometer. These telemetry data are received, processed, and separated into files based on orbit number and a single-digit index related to placement on the CRRES body. The files of interest are the CMF####0 and CPC####0 files. The former data base is the measurement made by the CRRES scientific magnetometer; the latter is the measurement made by various instrument packages, including LEPA. In this guide, the "####" field will represent the orbit number, which ranges from 63 to 1067 for LEPA. The suffix "0" in the file names means that those instruments are located on a specific portion of the CRRES body. Knowing the placement of the instruments is crucial when using attitude determination software to translate the look angles of the FOV originally defined in a satellite body-centered frame of reference to an ECI-based coordinate system.

The orbital files mentioned above are available to Phillips Laboratory staff personnel. Certain codes have been written to extract specific information necessary for post-processing. The CMF####0 files are processed directly by Radex to get ECI-based geomagnetic field vectors, and will be discussed in Section 9.5. The CPC####0 files have been processed by PL personnel to produce LEPA#### files containing only the LEPA data for orbit ####.

## 9.2 PROCESSING OF LEPA DATAFILES

LEPA#### is the instrument data base whose basic file format and procurement are detailed in Appendix B of *Griffin* [1995]. The detailed contents of the data record depend on the operating mode, as described in *Hardy, et al.* [1993b]. To summarize the aforementioned document, LEPA detects background and incident counts as a function of zone and sector per channel for a given operating mode. Each data record contains measurements collected by LEPA within a half-spin.

LEPA software documentation [*Kerns*, 1993] describes how to extract the differential directional fluxes, time tags, look direction in the spacecraft coordinate system, and pitch angle. To perform this post-mission processing, PL staff personnel have written and used Borland Turbo PASCAL codes to strip out specific information from LEPA#### files. The PASCAL codes in question can read in a LEPA#### file, extract out specific details (dependent on the operating and voltage modes), and generate both the raw and averaged background counts. The embedded algorithms then test for consistent or corrupted counts. Portions of the code define calibration values and employ conversion expressions to assist in translating the net counts to equivalent differential directional flux values,  $j(\Omega, E)$ . Supporting routines are used to read post-processed magnetometer data and satellite ephemeris parameters concurrent to the time of the detector signals.

For portability and flexibility between machine platforms, Radex converted these routines over to FORTRAN and validated by comparison between the outputs from the original and modified executables. The reason for the cross-language conversion is that, while the object-oriented features of Turbo PASCAL are useful, the compiler is available only on the DOS-based personal computer system. Conversion to FORTRAN enables a wider pool of platforms to be available for programmers and users to port codes, to modify existing modules, and to incorporate additional features within driver software. For example, LEPAFLUX is the simple driver using the converted routines to obtain the fluxes with the corresponding pitch angle for each sector and zone within every half-spin. LEPAFLUX then passes the information to an user-defined module where additional codes could be inserted. As another example, GET3DBIN uses these converted routines to derive and to bin individual differential directional fluxes prior to computing the mean differential directional fluxes separately for the electrons and ions.

### 9.3 THE BASICS OF THE LEPA FILE PROCESSING

Note that LEPAFLUX is significantly different from GET3DBIN in two aspects. First, LEPAFLUX reads the magnetometer files already created by PL staff. Second, the program does not presently have embedded routines for converting fluxes from a satellite body-centered coordinate system to other frames of reference. What is in common for both codes are the user-interface features, and use of general support routines designed for reading the LEPA data file to extract and convert the net counts into fluxes. For this reason, detailed discussion on LEPAFLUX is deferred to the next section after a brief mention in this section.

#### 9.3.1 Theoretical Motivations

It is necessary to establish an initial frame of reference that is satellite body-centered, i. e., the spacecraft coordinate system. To visualize the physical setup of CRRES, imagine a rigid disk-like body bearing eight flat sides. Let there be an imaginary cylinder defined by the surface containing the flat sides on the satellite body. To complete the picture, let the "disk" rotate so that the spin axis is coaxially centered through the imaginary cylinder and exiting from the endcaps. This means that the eight flat sides move in a constant radius around the spin axis; the surface of the cylinder will then be rotating rather than the endcaps.

Let there be a normal projection from the spin axis passing perpendicularly through the flat plate where LEPA is mounted. This projection would be in the center of the FOV with eight zones on each side closer to the spin axis. By defining that normal projection via the FOV as the x-axis and the spin-axis, the z-axis, the y-axis nominally follows from applying the right-hand rule of orthogonality. Since LEPA is fixed relative to the satellite body, its FOV could only sweep in the positive x-z half-plane. The rotation of the satellite allows the x-axis to be spun about the z-axis. From the satellite frame of reference, this x-axis would be sweeping out an equatorial plane, while the look angles within the FOV fan would be able to scan up and down through the plane. The discussion simply means that LEPA is capable of sampling around the spin axis of



the satellite; the specific look angles due to a zone within the FOV fan will cover a solid annular ring parallel to the equatorial plane.

The raw counts as detected within a given sector and zone can be converted into directional differential number fluxes. The relationship between the raw counts and the resulting fluxes is given as

$$j(\Omega, E) = f_s \bar{\eta}[\Omega] G[E, V] (n[\Omega] - \langle n[\Omega] \rangle_{bgnd}) \quad (9-1)$$

where  $f_s$  is the sweep frequency;  $G$ , geometric factor;  $n$ , detected raw count;  $\langle n \rangle$ , averaged background count; and  $\bar{\eta}$ , effective detector efficiency. The latter is actually the original efficiency modified to take into account the fact that the coarse zones measurement are either added or averaged raw counts, depending on the species. See sections 4.3 and 4.4 of *Kerns* [1993] for more detail.

Both the LEPAFLUX and GET3DBIN codes can read the LEPA data file and compute the fluxes as discussed so far. At this point, LEPAFLUX will output the flux values, differentiated by species and operational modes, to a file before terminating its run; GET3DBIN does some additional processing with the data. GET3DBIN makes use of the known satellite attitude to transform the fluxes to a more suitable coordinate system. This is accomplished by knowing that the spinning rate of CRRES has been nearly constant, and that the orientation of the spin axis has already been worked out in earlier research. Therefore, any measurement made relative to the spin axis can then be transposed to a non-rotating coordinate system. All that is sufficient for LEPA operational goals is to make a series of measurements, time-tagged to the spin rate. Given the satellite spin rate, position, and attitude for all data points, coordinate transformations of the measurement are possible.

The current software uses the CRRES attitude determination routines, previously developed by Radex for coordinate transformation from a satellite body-centered frame of reference to a non-rotating system. For more details, see *McNeil* [1991]. Note that the technique allows transformation of both the measured geomagnetic field components and instrumental look directions to be mapped to the ECI frame of reference from the satellite body-centered coordinates. Once the ECI components are defined, standard coordinate transformation routines can be used to recast the values into another frame of reference for additional specialized post-processing.

In most studies of magnetospheric plasma, the plasma velocity distributions are considered to be gyrotropic, i. e., independent of the direction of the component normal to the magnetic field. The distribution function then depends only on the energy and the pitch angle, which can be determined entirely within the spacecraft coordinate system. To express meaningful results for non-gyrotropic distributions, it is necessary define a despun coordinate system, one not rotating with the satellite spin. It is further desired to have the z axis of this system aligned with the magnetic field, so that one can specify direction by pitch angle and azimuth, the latter being an angle of rotation in the plane normal to the field.

To define the azimuth, one can invoke a rectangular coordinate system, called the "magnetic field meridian" system, as follows:

- z axis: parallel to the magnetic field direction B
- x axis: parallel to the cross product (magnetic east)  $\times B$
- y axis: completes right-handed rectangular system with z and x.

Magnetic east is the y or "D" direction in the "VDH" coordinate system (Figure 3-20, from *Bhavnani and Vancour* [1991]), which has the dipole vector as its z, or "H" direction, while x ("V") points radially outward. If the magnetic field and the dipole vector are parallel, as is the case near the magnetic equator, then the coordinate system defined here is identical to the VDH system. One could define azimuth as being the angle of rotation from +x to +y.

Repeated sampling by or prolonged exposure to a detector is usually required in order to have confidence in the measured number of charged particles within a specific energy range. There are variations in background levels as well as particle density; spurious data points can and do occur. By nature of LEPA operations, data consist of only discrete components for the plasma energy spectrum. To address these issues in reconstructing the continuous energy spectrum in three-dimensional space, data from several spins must be combined or fitted.

In an attempt to combine the data on a physical basis, Radex has employed a binning scheme using the VDH coordinate system. By defining a two-dimensional grid based on azimuth and pitch angles, it is possible to map the measurements from an initially satellite body-centered frame of reference to, ultimately, the  $(\Phi, \alpha)$  points on the grid. The distribution of the discrete fluxes would hint at structures within the plasma data as detected by LEPA. By dividing the grid into intervals of azimuth and pitch angles as bins, several half-spins worth of measurements can be accumulated in order to increase confidence in the data above the background levels. Spatial resolution may be reduced but general trends can be determined and even fitted as a function of these indices.

The values for  $\Phi$  are restricted to the interval 0 to  $2\pi$  radians ( $360^\circ$ );  $\alpha$ , 0 to  $\pi$  radians ( $180^\circ$ ). Binning by  $\Phi$  is simple; the range can be divided into equal-sized bins. Binning by  $\alpha$  is not as simple, since higher resolution for extreme values is desired, to cover loss cone regions. To satisfy the requirement and yet provide equal-spaced intervals for mid-range, the end bins are made half the size of the other bins.

GET3DBIN uses the binning scheme to read in LEPA data for several half-spins, adding the fluxes into associated bins. Upon completion of a cycle of these half-spins, the code will determine the statistical information for each bin and output the information to a file. See Section 9.6.2 for details.

### 9.3.2 Basic Steps of the Software Processing

Except for the case of LEPAFLUX, the initial step is the extraction of ECI-based measured geomagnetic field components from the scientific magnetometer database. The processing ends when the three-dimensional distribution of the plasma density are computed for both the electrons and the ions. Note that the discussion on the pertinent major programs in each step is supplemented by more detailed sections later on in this report. The reader is encouraged to refer to the general operational flowchart in Figure 45 where the step by step procedure is depicted.

Starting with the data files related to the measurements made by LEPA and the scientific magnetometer, all files are processed in piecewise fashion. For each processing step, there are three major stages. The initial stage is to retrieve the necessary input files from various sources for each software package. The next stage is to create the output data files by running the code. The final stage is to validate the results by plotting the data. Each major code has a subsequent section devoted to it; within those sections are detailed information on how one can retrieve the input files, execute the main code, and post-process the output files.

Before proceeding with the discussion of software-related processing, an explanation is needed for the file name convention used in this manual. In the original convention, some of the file names are suffixed with '####0' where '####' is the orbit number of interest and '0' refers to the location of the instrument on the CRRES body frame. Files whose data are not dependent on instrument placement have been named as "ABCD####" where the first four letters tell what type of file it is. The latter convention has been used in the original PASCAL codes; the convention has been adopted in current codes to maintain consistency. The advantage of this renaming convention is that, when the user is forced to make a local copy with a slightly different name, this approach actually avoids accidental overwriting of the original files. In the codes, the actual filenames are hardwired as "ABCD####", where the CRRES body frame placement index can be inserted, if needed, into the "D" slot.

A programming discussion of these codes must be given first. All software has been written in FORTRAN language and compiled with Microsoft 5.1 FORTRAN compiler. By not incorporating any Microsoft WINDOW interface features, all codes are made to run on a basic DOS system under the 640 Kbyte RAM limits. Each code is designed to be portable to other systems as much as possible. There are three changes necessary to fully implement the software on any mainframe: the use of command-line argument utilities, bit manipulation routine calls, and one nonstandard library call. See "Appendix A: Porting To Other Systems" for additional details. For the enduser, it is sufficient to mention that most codes make use of either the *command line arguments* or a special user-modified input file called a *namelist* file, or both.

Command line arguments allow the user to enter additional arguments on the same line as the program name after the system prompt. Implementation of the command line arguments feature is system-specific, and is explained in more detail in Appendix A of *Griffin* [1995]. The command line arguments are advantageous when the user just wants to do a single-line launch

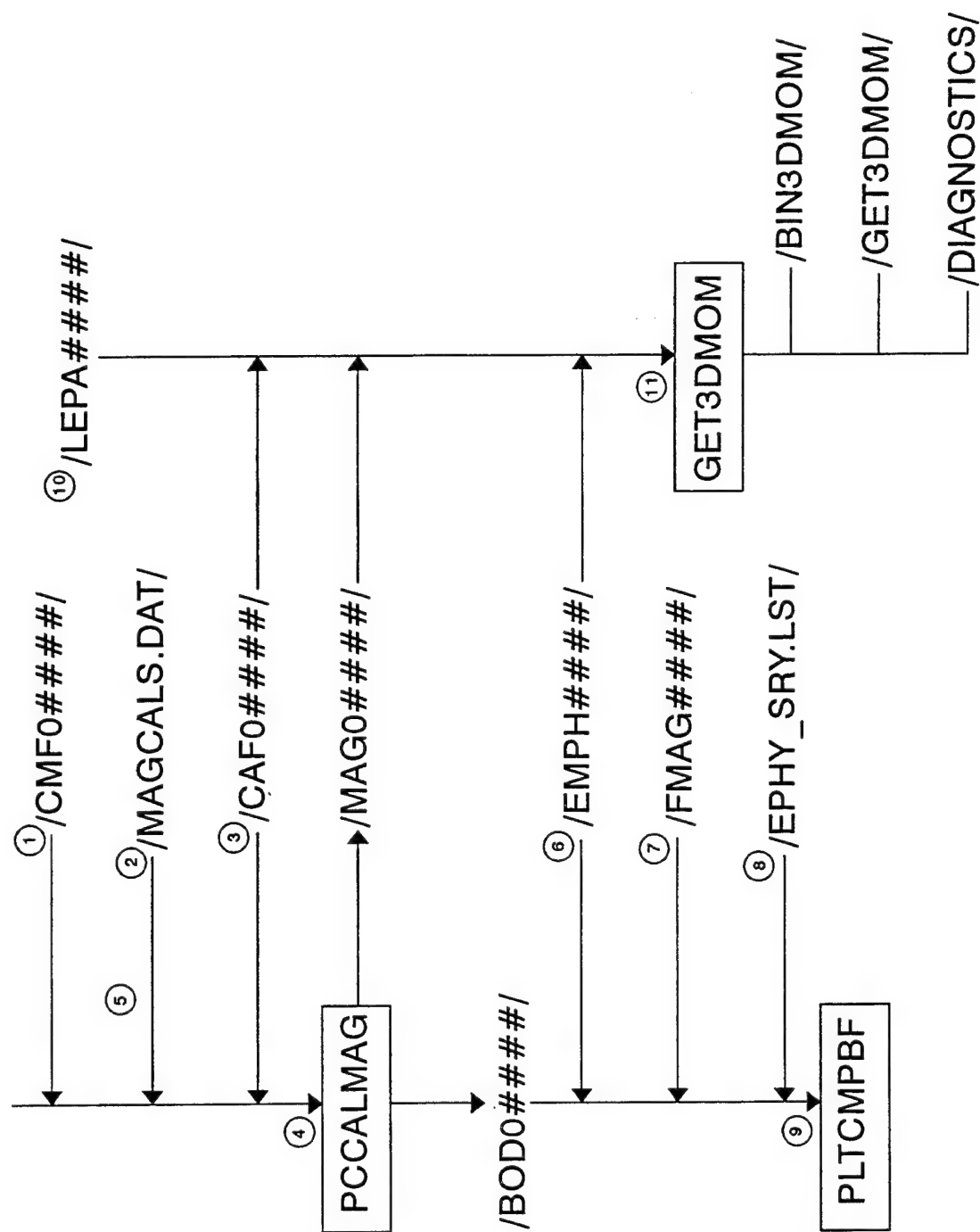


Figure 45. Processing of LEPA data by steps.

of the application code. The feature is also suitable for use in a DOS batch file which could be used to run several orbits.

NAMELIST is an input/output utility that enables any program to read in a flexible number of values or to write out a diverse set of variables specific to a run. Although the NAMELIST feature is not in the FORTRAN-77 standard, it is available on most, if not all, compilers. The widespread implementation of NAMELIST by the majority of operating systems has encouraged its official recognition in the FORTRAN-90 standards. NAMELIST is typically useful when there is a large number of input parameters, most of which can be set to default values unique to the user. In such a case, the user need supply only those inputs which differ from the programmed defaults.

To run these codes, the typical procedure is to simply type "*program\_name* #### *program\_namelist\_file*" to process the appropriate data files for the orbit numbered "####" using the input namelist file *program\_namelist\_file*. For convenience of the user and programmer, a namelist file has been provided to pass default parameters that could be changed from machine to machine, task to task. The default namelist file can be generated by simply typing "*program\_name* ####". The program running for the first time will not find the default namelist in the current directory and will create one for the user before terminating. In regard to creating a default namelist, any legal orbit number actually can be used, since the program first looks for the file before processing any data.

Before running any software package, several input data files must be collected from various sources and several of them must be processed before use. Most of files are from the CRRES historical database, which contains flight-time data from various onboard instrument packages, such as the magnetometer, and post-mission computed quantities, such as the satellite ephemeris. Of those files, some are available at Phillips Laboratory on-line via the mainframe accounts or on media not accessible by network systems. Retrieval of inaccessible data requires on-site visits once the user is given access authorization. Radex will provide the remainder of the necessary files. Instructions on how to acquire them will be specified in Appendix B of *Griffin* [1995].

All of the plotting packages mentioned in this report use GraphiC, a graphics utility package put out by Scientific Endeavors Corporation. Given the interfacing files necessary to work with Microsoft FORTRAN, the graphics library utility allows the user to first preview the plot on the screen and, if desired, create a hardcopy of the same plots on any printer.

#### 9.3.2.1 Magnetometer Database Processing

Magnetometer data files are necessary in order to compute the pitch angles for the directional differential fluxes. In the case of LEPAFLUX, there are already PL post-processed data files available for each orbit. See Section 3 for more details. GET3DBIN uses a magnetometer data file where the three components of the geomagnetic field are in an ECI reference frame. This section gives a brief summary of the process; actual instructions are provided in Section 9.5.

The first step to generate the suitable magnetometer datafile for GET3DBIN is running PCCALMAG. For input files, PCCALMAG uses the magnetometer THDB (Time History Data Base) and the calibration files. In addition, the CRRES attitude determination coefficient file is also required for processing. Appendix B of *Griffin* [1995] will fully describe where and how to obtain those files. The only necessary discussion here is what the files represent. The magnetometer THDB is the telemetry database which contains signal strengths as measured by the scientific magnetometer. The calibration file is used for converting those sensor signals into an equivalent three-component geomagnetic field strength in a satellite body-centered coordinate system. The CRRES attitude determination coefficient file is the file necessary to transform any vector defined within the satellite body-centered system into the ECI-based coordinate system.

Running PCCALMAG actually requires two passes. The first pass is to generate the geomagnetic field components as measured in a satellite body-centered frame of reference for validation purposes. The second pass is to actually convert the magnetometer signals from the database into geomagnetic field components as would be seen in an ECI-based frame of reference at the satellite position.

The purpose of the first pass is to validate that the processing of the magnetometer data base does not introduce any spurious or sudden discontinuity points in the output file. Probably the easiest and the most sensitive measure of anomalous behavior within the processed magnetic field is the abrupt change in the angle between the geomagnetic field vector and the spin axis of the CRRES satellite. This angle is referred to as the *elevation* angle,  $\theta$ . A satellite body-centered quantity, the elevation angle is defined as

$$\cos(\theta_e) = \hat{z}_{sat} \cdot \hat{v}_{sat} \quad (9-2)$$

where the unit vector  $z$  aligns with the spin axis of the satellite, and unit vector  $v$ , with any vector measured in the satellite body-centered coordinate system. The elevation angle for the geomagnetic field vector is the easiest and quickest way to perform diagnostic studies on the newly-processed magnetometer file.

Thus, the validation process is generally quite simple, for it requires only that a graphical inspection of the elevation angle for the geomagnetic field be made in comparison to two other sources of geomagnetic field values. To accomplish this task of superimposing elevation angles from three different geomagnetic field-based data files in a plot, a plotting package called PLTCMPBF is used.

Described in Section 9.5.2, PLTCMPBF (PLoT of CoMParison of B Fields) reads the newly-computed values and compares the secular trend and fine structure variations within the new data with those computed from two input files. One is the static geomagnetic field model (IGRF-85) stored within the CRRES ephemeris file. The other is 30-second interval field components previously-processed from a similar magnetometer historical data base. In addition to the previously mentioned three files, PLTCMPBF also needs the CRRES attitude determination coefficient file to map the quiet geomagnetic model components from an ECI frame of reference

to satellite body-centered coordinates.

Having established the input requirements, validation procedure with PLTCMPBF actually consists of checking three features of the plot. First, the long-term trend of the measured geomagnetic field should follow the secular trend of the static model field for the quiet portion of the orbit. Second, the previously-processed magnetometer data file done by PL staff would be closely followed by the short-term behavior of the newly-processed field. Finally, there should be a lack of abrupt discontinuities in the timeline plot of the processed data.

In the event that the magnetometer data passes the visual inspection, the second pass is then performed and the output magnetometer file is created, having the three components of the measured geomagnetic field defined in the ECI-based coordinate system. The newly-created file containing the ECI magnetic field vectors is available for the next step described in Section 9.3.2.2.

If the validation has revealed a possible problem with the processing of the magnetometer data file, modifications can be made to the several data editing algorithms within the code. See Section 9.5 for more details.

#### 9.3.2.2 Binning of Differential Directional Flux

GET3DBIN is the next major code to run and requires several input files. More specific details are given in Section 5 on how to use/provide input values and select options. Here, it is sufficient to describe the steps necessary to generate the next level of output values. The primary input file is the LEPA data file and the newly-created magnetometer data file. The necessary additional input files are the attitude determination coefficient file and the ephemeris historical database already used in the previous phase.

The main functional role of this code is to compute the mean  $j(\Omega, E)$  as a function of the  $(\Phi, \alpha)$  bin indices. The operational scheme is to first compute the net counts for each of the sectors and zones within the FOV for both the electron and ion constituents. The counts are converted into the instantaneous  $j(\Omega, E)$ . Once the value has been determined, the look angle for the sector and zone portion of the FOV is translated to the ECI-based coordinate system. By using the magnetometer data, the pitch angle is also computed. Given the magnetic field components, conversion from ECI to VDH coordinates is defined, and the azimuth angle follows from definitions based on the coordinate transformation as given in Section 9.3.1. Each measurement is thus assigned an azimuth-pitch angle bin to go along with its association with a specific energy channel. Means and standard deviations of the fluxes over a specified number of half-spins are determined for each channel and directional bin. The results are saved to an output file whose format structure is described in Section 9.6.2.2.1.



## 9.4 INTRODUCTION TO LEPAFLUX

This section describes the program LEPAFLUX initially in terms of overall functional role with regard to LEPA datafiles. The discussion centers on basic operational features of the software package. The first subsection will explain how and what input/output files are needed.

LEPAFLUX is a PC-based software utility that reads in a LEPA datafile to find the pitch angle ( $\alpha$ ) and corresponding differential directional fluxes,  $j(\Omega, E)$ , of the ion and electron distributions. Basically, LEPAFLUX extracts raw and averaged background counts from measurements made by LEPA within a specific zone and sector for each energy channel, and converts the net counts into  $j(\Omega, E)$ . The fluxes are stored by energy channel number and voltage level for each sector and zone. The pitch angles are computed and stored either as its cosine or angular value measured in radians or degrees. Depending on the user's choice, the printout of the stored values can be made for every  $N_{1/2}$  half-spin. There is no coordinate transformation performed; all values are given in the spacecraft coordinate systems.

The chief feature of this code is the inclusion of a subroutine, "USER\_MODULE". As is currently designed, "USER\_MODULE" just prints out the stored values of  $\alpha$  and  $j(\Omega, E)$  for every  $N_{1/2}$  half-spin. Here is where a user could implement additional post-processing schemes for the collected fluxes and corresponding pitch angles. The advantage is to provide a "hook" without any necessary modifications to the supporting routines.

LEPAFLUX reads both the command line arguments and a NAMELIST file for orbit-dependent and input file-specific values. The user is required to enter the orbit number on command line, followed (optionally) by the name of the namelist file, which overrides the default name LEPAFLUX.INP. The namelist file contains the pathnames necessary to find the required input files to do a run. Also within the namelist file is a switch for controlling the range of data analysis.

To process a LEPA file, LEPAFLUX needs two other orbit-dependent datafiles. They are used to compute the time-dependent pitch angle, and to obtain ephemeris-dependent quantities. These files are available at Phillips Laboratory. The first file is the geomagnetic components measured by the onboard CRRES magnetometer in the satellite body-centered coordinate system. The magnetometer data file had been processed by the original PL code, CMF2FMAG, and is named "FMAG####". The second file is read in by one of the support PASCAL-based routines to obtain crucial values, such as satellite position and velocity, sun look angle, and geomagnetic model values. The latter file is not actually used, but is provided in case the user wishes to use the information for additional post-processing of the fluxes.

### 9.4.1 Overall General Descriptions for Input

The necessary user-dependent inputs are given both as command line arguments and from within a NAMELIST file. On the command line, the user enters the orbit number and the name of a



NAMelist file if different from "LEPAFLUX.INP". This latter feature provides flexibility of using different NAMelist files tailor-fit for special cases, such as different LEPA operational modes. The NAMelist file provides file pathnames, assigns data control parameters, and sets an optional switch. The NAMelist options and command line arguments are described in *Griffin* [1995].

#### 9.4.1.1 Input Files

Before running LEPAFLUX, three input files are needed. The primary input file is LEPA####. FMAG#### provides the magnetometer data. E000#### supplies the CRRES ephemeris and geophysical data related to the satellite positions.

#### 9.4.2 Overall General Descriptions for Output

The output of LEPAFLUX consists of sequential screen dumps and one primary output file, named "LEPAFLUX.OUT" by default. The primary output file contains, for both the ion and electron species, their differential directional fluxes and corresponding pitch angles for a given set of  $N_{1/2}$  half-spins sampled from the LEPA datafile. The output format is described and the interpretation of the values are explained in *Griffin* [1995].

##### 9.4.2.1 Structure and Format of the Primary Output Data File

LEPAFLUX creates one primary output data file whose default name is "LEPAFLUX.OUT". It is an unformatted datafile with one header record followed by sequential data records containing the  $\alpha$  and  $j(\Omega, E)$  values. The subsequent data records contain the fluxes and pitch angles for all viable channel numbers as a function of voltage level, operational mode, species type, and sector/zone indices.

Since the current programs are capable of reading in only the mode 0 and mode 10 data from the LEPA file, there are four possible types of data that could be written to the primary output file. The types are electron mode 0 loss-cone sector, electron mode 0 perpendicular sector, electron mode 10, and ion mode 0/10. The first two types only have data from one sector, but 14 zones; the latter two, from eight sectors and 6 or 7 zones. This means that each type requires a slightly different way of presenting the range of fluxes and pitch angles possible.

To minimize the extensive coding in order to write and read the data in the output file, each data type is required to use three distinctive records. The first WRITE creates a record of four variables associated with the data type. The next WRITE will give the pitch angles; the last, the fluxes.

For the first record, there are four variables uniquely associated with the data type. The first variable is a five-byte character label signifying the data type. The second and third variables are integers indicating the number of sectors and zones, respectively. The last is an integer,

giving the UT time in milliseconds, either as a scalar or an array of 8 elements. The 5-byte label for mode 0 electron cases are 'LOSSC' and '90DEG'; mode 10 electrons and ions, 'ECRSE' and 'IONS '. The first record is designed to handle all four of these types.

## 9.5 PROCESSING OF THE MAGNETOMETER DATABASE

GET3DBIN uses the measured geomagnetic field components in an ECI-based coordinate system to compute and bin  $j(\Omega, E)$  values. The code to provide the requisite magnetometer data file is PCCALMAG. A DOS-based utility, PCCALMAG is designed to process the historical magnetometer data imported from the PL mainframe and creates a file with either satellite body-centered or ECI-based geomagnetic field vector components as measured by the satellite. It employs extensive data editing based on mission events and hardware glitches. By default, it generates the file in a form suitable for data validation with other sources of the geomagnetic field.

To perform a validation check, the geomagnetic field elevation angle is primarily used. Experience has been that elevation angle for the geomagnetic field vector is the easiest and quickest way to perform diagnostic studies on the newly-processed magnetometer file. Using elevation angles from three different geomagnetic field-based data files, validation is done with a plotting package called PLTCMPBF.

PLTCMPBF, short for PLoTting the CoMParison of B Fields, shows three overlapping curves representing the elevation angles of the geomagnetic fields derived from the three different files. Essentially, the program first reads a CRRES ephemeris file to extract the ECI-based quiet IGRF-85 model geomagnetic field components, and uses the attitude determination coefficient file to convert the ECI-based coordinates to body-centered values before calculating the elevation angle. Next, the elevation angles are read directly from the FMAG file. Finally, the body-centered version of the magnetometer file generated by PCCALMAG is processed to obtain the elevation angles. For essential details of setting up a run for each of these codes, see *Griffin* [1995].

### 9.5.1 Output File from PCCALMAG

The output file is named 'BOD0####.DAT' or 'MAG0####.DAT', depending on whether the user desires a body-fixed or an ECI-based coordinate system. The structure of both ASCII data files consists of a single header record containing integers, separated by spaces, denoting the orbit number, modified julian date, year (90 or 91) and day of year (1-365) for the start time of the orbit, and the orbit number from the calibration file that actually provides the signal conversion coefficients. The subsequent data records have four real\*8 values, a time value and the corresponding B-field components for each output file.

## 9.6 INTRODUCTION TO GET3DBIN

GET3DBIN is a PC-based software utility that reads in a LEPA datafile to calculate user-defined interim quantities and mean differential directional flux values of the ion and electron distributions. More specifically, GET3DBIN first scans a specific number of half-spin data records to extract net counts and converts them into differential directional flux distributions as functions of energy and look angles relative to CRRES. The code then does a coordinate transformation from the spacecraft frame of reference to the magnetic field meridian frame, in order to sort the measurements by pitch angles ( $\alpha$ ) and azimuth ( $\Phi$ ). Upon completion of reading in a user-defined number of half-spin records, GET3DBIN performs basic statistical analysis on all of the non-zero populated bins, and saves aside the mean and unbiased standard deviation values per bin as a separate file. GET3DBIN provides optional features to do intermediate spot-checking and output for plotting packages. The techniques used in determining the plasma moments will be explained in another section.

To process a LEPA file, GET3DBIN needs three other orbit-dependent datafiles. They are used to compute the time-dependent pitch angles, to transform from satellite-centered coordinates to ECI frame of reference, and to obtain ephemeris-dependent quantities. These files are either available on the mainframes at Phillips Laboratory, or by request from Radex. The first file is the ECI-based geomagnetic components derived from onboard CRRES magnetometer data preprocessed by another Radex code, PCCALMAG. The second file enables the user to compute attitude determination of the instrument FOV located on a specific point of CRRES. That ability is made possible by a set of software utilities written at Radex [McNeil, 1991]. The third file is read in by one of the support PASCAL-based routines to obtain crucial values, such as satellite position and velocity, sun look angle, and geomagnetic model values.

### 9.6.1 Overall General Descriptions for Input

The necessary user-dependent inputs are both given as command line arguments and from within a NAMELIST file. On the command line, the user enters the orbit number and the name of the NAMELIST file if different from "GET3DBIN.INP". This latter feature provides flexibility of using different NAMELIST files tailor-fit for special cases, such as different LEPA operational modes. The NAMELIST file provides file pathnames, defines binning limits, assigns data control parameters, and sets optional switches. The NAMELIST options and command line arguments will be described later.

#### 9.6.1.1 Namelist File Descriptions

The NAMELIST file contains user-defined choices in file management, binning limits, and option switches. The file management aspect deals primarily with where the input files are located, what names are assigned to the output files and where they are to be placed. Limits on data collection for statistical purposes are done for either ions or electrons, or both. These limits control the cutoff for the channel index, the number of bins for pitch angle ( $\alpha$ ) and

azimuth ( $\Phi$ ) coordinates, or disabling the use of data from coarse zone 0. Spot-checking on a portion of LEPA data is accomplished by using various options to print out intermediate values. One example of data integrity inspection is generating sector-zone maps of differential directional fluxes per half-spin separately for ions and electrons within a given slice of UT in orbit. Another is a check for hits within VDH-based binspace by zonal sweeps and projections of spin axis and sun/antisunward look angles.

The code is set up to sort the electrons and ions separately; there is a feature that allows for different numbers of pitch angles and azimuth bins to be used in statistical sorting. The current limit is 12 each for each species. Likewise, this feature extends to channel numbers (important because of the poor operational quality of LEPA in collimating electrons for channels whose indices are higher than 19). Accordingly, one would run with 19 channels for electrons and use that value or a higher number for ions at the user's discretion.

The principal output file is "FILE\_BIN\_OUTPUT". The file contains the information on what is statistically stored in populated bins for the requested number of half-spins with a time tag. As a plotting software package, PLT3DBIN, can read and display the data. Its descriptions are listed in the appendices of *Griffin* [1995].

#### 9.6.1.2 Input Files

Before running GET3DBIN, several input files must be collected from various sources and several of them must be processed before use. The majority of files are from the CRRES historical database, containing flight-time data from various onboard instrument packages, such as the magnetometer, and post-mission computed quantities, such as the satellite ephemeris. Of those files, some are available at the Phillips Laboratory on-line via the mainframe accounts, or on media not accessible by network systems. Retrieval of inaccessible data requires on-site visits once the user is given access authorization by the principal investigators in charge. The remaining files are provided by Radex.

#### 9.6.2 Overall General Descriptions for Output

The output of GET3DBIN consists of sequential screen dumps and one primary output file, named "GET3DBIN.OUT" by default. As an option available in the input namelist file, there is also an interim diagnostic file, named by default as "PLTHSPIN.INP", which would be read in by a plotting package, PLTHSPIN. The screen dumps can be redirected to a file, if desired by the user. The primary output file contains the mean differential directional fluxes for both the ion and electron species, along with statistical information and populated bin indices for a given set of  $N_{1/2}$  half-spins sampled from the LEPA datafile. The diagnostic file has differential directional flux values found for each sector and zone within each half-spin differentiated by charge species and voltage modes.

GET3DBIN sorts  $N_{1/2}$  half-spin worth of data into the appropriate bins and does a statistical analysis of the populated bins first for the electrons and then for the ions. Each bin is defined uniquely by a discrete range of pitch angles and azimuth angles, voltage mode, channel number, and charged particle type. Given a bin, the mean value for a populated bin having added in  $N_B$  differential directional flux values is

$$\bar{d} = \frac{1}{N_B} \sum_{i=1}^{N_B} d_i, \quad (9-3)$$

where the  $j$  represent the differential directional flux. The standard deviation,  $\sigma_j$ , is computed as

$$\sigma_d = \sqrt{\frac{\left( \sum_{i=1}^{N_B} d_i^2 \right) - N_B \bar{d}^2}{N_B - 1}}, \quad (9-4)$$

based on using the rewritten formulation of the conventional definition for *unbiased*  $\sigma_j$ ,

$$(N_B - 1) \sigma^2 = \sum_{i=1}^{N_B} (d_i - \bar{d})^2, \quad (9-5)$$

with the sum expanded out. The statistical information for each bin is written out to the primary output file, while the summary of distribution of the mean values are printed out to the screen.

The bins are arranged by azimuthal and pitch angles with regard to charge species, voltage mode, and channel number. For both the electron and ion, the total number of bins possible is

$$N_{BIN} = 2 N_\alpha N_\phi N_{channel} \quad (9-6)$$

where 2 is the number of voltage modes possible and the subscripts refer to the pitch angle, azimuth, and channel indices, respectively. In actual binning, fewer bins may actually be populated due to limited coverage imposed by the FOV fan sweep and the orientation of the satellite spin axis with respect to the geomagnetic field lines. After processing all of the data desired, the program writes out the results of the binnings to both the screen and the output file. To the screen, the code prints the number of populated bins and number of maximum bins possible; to the file, the mean and unbiased standard deviation of the differential directional flux values of the populated bins. If there are low net count rates, an insufficient number of sampled half-spins, or a significant amount of data gaps due to adverse mission events, the populated bins could have zero or negative mean values. For this reason, the program prints out to the screen the number of negative, zero, and positive mean values in populated bins as a measure of how the data performed, statistically speaking.

Because there are so many bins that can be filled, a packing scheme has been implemented to designate a specific bin. This is necessary to reduce the size of the output file. A typical run

with  $N_{1/2} = 32$  and default number of bins would have created a 8 MB binary data file just by printing out the mean and unbiased standard deviation values in single precision for all of the possible bins, without including the number of flux density points accumulated within each one. By implementing a bitmapping scheme that packs the bin indices and number of points per bin within an integer preceding the statistical values, only the populated bins would be tagged and printed out.

#### 9.6.2.1 Output Datafiles

By default, GET3DBIN creates one primary output data file. GET3DBIN will also create an additional file if an optional diagnostic feature is selected. The former file employs a bit-packing scheme while the latter does not. The latter is presumably smaller, because only a single channel is sampled and usually a few half-spin cases are designated by the user. Appendix B of *Griffin* [1995] gives the specifics for packing and unpacking the information from the output files.

Once the goal was to avoid having a large file created when the program dumps out all of the bins. The procedure for reducing the size of the database has to be developed. There may be a sparse number of populated bins, particularly for mode 0 electrons. In contrast, there may be a large number of filled bins if mode 10 electrons and ions are collected over many half-spins. Therefore, the method to reduce the file size will require that any number of filled bins be written out without regard to placement. The disadvantage to dumping out only the filled bins requires means to identify the individual bins. Just using indices by themselves as individual values would have added more datawords for each populated bin. The solution is to pack the indices into specific field of bits within a data word. This scheme effectively compresses all of the identifier data words into one. Even with the indices stored within the one target word, there are still unused bits available. Since there is a need to indicate the number of datapoints used in the statistical analysis for each bin, that critical value is also packed. Appendix B of *Griffin* [1995] gives the specifics for packing and unpacking the information from the output files.

#### *Structure and format of primary output file*

The default name of the primary output file is "GET3DBIN.OUT". It is an unformatted datafile with one header record with sequential data records containing statistical results from summing up  $N_{1/2}$  half-spin worth of LEPA data.

#### *Structure and format of half-spin datafile*

If the option "WANT\_HSPIN\_DUMP" is selected, the code will generate an unformatted binary data file that would contain the differential directional flux value found within each sector and zone for a given channel number every half-spin. When the option is enabled, the user can select a portion of the orbit by specifying the beginning and end times in UT as milliseconds. The resulting file will generate separate reports for each half-spin for electrons and for ions.

## REFERENCES

- Bhavnani, K. H. and R. P. Vancour, "Coordinate Systems for Space and Geophysical Applications", PL-TR-91-2296, 1991, ADA247550.
- Blake, J. B., *Private Communication*, 1991.
- CRRES Microelectronics Package Serial Telemetry Manual, Naval Research Laboratory, Space Systems Development Department, Washington, D.C., December 1, 1989.
- CRRES Microelectronics Package User's Guide, Naval Research Laboratory, Space Systems Development Department, Washington, D.C., December 30, 1989.
- FORTTRAN Version 1 for NOS/VE Language Definition, Control Data Corporation, St. Paul, MN, 1988.
- GraphiC<sup>TM</sup> 6.0 Publication Quality Scientific Graphics, Scientific Endeavors Corporation, Kingston, TN, May, 1991.
- Gussenhoven, M. S., E. G. Mullen, R. C. Filz, F. A. Hanser, K. A. Lynch, "Space Radiation Dosimeter SSJ\* for the Block 5D/Flight 7 DMSP Satellite: Calibration and Data Presentation", AFGL-TR-86-0065, 20 March 1986, ADA172178.
- Gussenhoven, M. S., E. G. Mullen, and E. Holeman, "Radiation Belt Dynamics During Solar Minimum", *IEEE Trans. Nuc. Sci.*, 1989.
- Gussenhoven, M. S., E. G. Mullen, and R. C. Sagalyn, *CRRES/SPACERAD Experiment Descriptions*, AFGL-TR-85-0017, 1985, ADA160504.
- Gussenhoven, M. S., E. G. Mullen, H. Singer, J. Fennel and A. Vampola, *Private Communication*, Phillips Laboratory, 16 April 1990.
- Gussenhoven, M. S., E. G. Mullen, M. D. Violet, C. Hein, J. Bass, and D. Madden, "CRRES High Energy Proton Flux Maps", *IEEE Trans. Nuc. Sci.* 40, 1950, 1993
- Griffin, A., D. Delorey, and R. McInerney, *Private Communication*, October, 1989.
- Griffin, J. M., "Programmer and Enduser's Guide to Processing LEPA Data Files", PL Technical Report, to be published, 1995.



## REFERENCES (Cont'd)

- Hardy, D. A., D. M. Walton, A. D. Johnstone, M. F. Smith, M. P. Gough, A. Huber, J. Pantazis, and R. Burkhardt, "Low Energy Plasma Analyzer", IEEE Trans. Nucl. Sci., Vol. 40, No. 2, pp. 246-251, 1993a.
- Hardy, D. A., D. M. Walton, A. D. Johnstone, M. F. Smith, M. P. Gough, A. Huber, J. Pantazis, and R. Burkhardt, *Private Communication*, 1993b.
- Hein, C. "The Protel Contamination Code", PL-TR-93-2178, 1993, ADA273806.
- Hein, C., *Private Communication*, 1990.
- Hein, C. and J. Bass, "Modeling the DMSP and CRRES Dosimeters using the Path Length Distribution Method", PL-TR-93-2120, 1993, ADA269898.
- Hilmer, R. V., *A Magnetospheric Magnetic Field Model with Flexible Internal Current Systems*, Ph D. Thesis, Rice University, Houston Texas, 1989.
- Janni, J., "Proton Range Energy Tables, 1 KeV - 10 GeV" in: Atomic Data and Nuclear Data Tables, Volume 27, 147-529 (1982), Academic Press, New York
- Kerns, K. J., LEPA Software Documentation, 1993.
- King, J. H., "Solar Proton Fluences for 1977-1983 Space Missions", J.Spacecraft, 11, No. 6, 401, 1974.
- Krimigis, S. M., T. P. Armstrong, J. W. D. Kohl, "Measurements of the Quiet-Time Low Energy Proton, Alpha and M-Nuclei Component in Cosmic Rays", 13th International Cosmic Ray Conference, 2, 1656, 1973.
- Lingenfelter, R. E., "The Cosmic-Ray Neutron Leakage Flux", *J. Geophys. Res.*, Vol. 68, P. 5633, 1963.
- Lynch, K., E. Boughan, D. Fisch, D. Hardy, K. Riehl, "PROTEL: Design, Fabrication, Calibration, Testing and Satellite Integration of a Proton Telescope", AFGL-TR-89-0045, Environmental Papers, #337, 1989, ADA214564.
- McIlwain, C. E., "The Radiation Belts", *Natural and Artificial Science*, 142, p. 355, 1963.



## REFERENCES (Cont'd)

- McNeil, W. J., "Aspects of the Calibration and Processing of the CRRES Fluxgate Magnetometer Data", PL-TR-93-2124, 1993, ADA270127.
- Mead, J. D., "Deformation of the Geomagnetic Field by the Solar Wind", *J. Geophys. Res.*, Vol. 68, P. 1181, 1964.
- Microsoft FORTRAN Reference, Version 5.1, Microsoft Corporation, Redmond, WA, 1991.
- Morel, P. R., F. Hanser, B. Sellers, J. L. Hunerwadel, R. Cohen, B. D. Kane, B. K. Dichter, "Fabricate, Calibrate and Test a Dosimeter for Integration into the CRRES Satellite", GL-TR-89-0152, Air Force Geophysics Laboratory, April 1989, ADA213812.
- Mullen, E. G. and M. S. Gussenhoven, *Results of Space Experiments: CRRES*, 1991.
- Northrop, T. G., *The Adiabatic Motion of Charged Particles*, John Wiley and Sons, New York (1963).
- Pfitzer, K., *Improved Models of the Inner and Outer Radiation Belts*, PL-TR-92-2193, 1992, ADA258708.
- Real Time Data Acquisition System, Assurance Technology Corporation, Carlisle, MA 1989.
- Redus, R., R. Filz, W. Swider, M. Violet, *Private Communication*, 1990.
- Roederer, J. G. *Geomagnetic Field Distortions and Their Effects on Radiation Belt Particles*, Rev. Geophys. and Space Phys., Vol. 10 No. 2, Pp. 599-630, 1972.
- Roederer, J. G., *Dynamics of Geomagnetically Trapped Radiation*, Springer Verlag, Berlin/Heidelberg/New York, 1970.
- Schulz, M. and L. J. Lanzerotti, *Particle Diffusion in the Radiation Belts*, Springer Verlag, Berlin/Heidelberg/New York, 1974.
- Simpson, J. A., M. J. Munoz, M. Perkins, and J. P. Wefel, "The Experiment for High Energy, Heavy Nuclei Composition (ONR-604)", in CRRES/SPACERAD Experimental Descriptions, eds. M. S. Gussenhoven, E. G. Mullen, and R. C. Sagalyn, Air Force Geophysics Laboratory, AFGL-TR-85-0017 (Hanscom AFB, MA, ADA160504), Pp. 163-173, 1985.
- Smith, H. J., and E. V. P. Smith, "Solar Flares", Mc Millan Co., 1963.

## REFERENCES (Cont'd)

- Tsyganenko, N. A. and A. V. Usmanov, "Determination of the Magnetospheric Current System Parameters and Development of Experimental Geomagnetic Field Models Based on Data From IMP and HEOS Satellites", *Planet. Space Sci.*, Vol. 30, Pp. 985-998, 1982.
- Violet, M., *Private Communication (Understanding Protel)*, 1992.
- Wefel, J. P. and T. G. Guzik, "The Interplanetary Heavy Ion Environment for Both Galactic Cosmic Rays and Solar Energetic Particles during the CRRES Mission", PL-TR-91-2252, 1991, ADA248942.
- Wolfram, S., Mathematica: A System for Doing Mathematics by Computer, (documentation), 2nd ed., Addison Wesley, Reading, MA; Program - Wolfram Research Corp., 1991.